The Pennsylvania State University

The Graduate School

Department of Physics

EXPERIMENTS ON A ONE-DIMENSIONAL BOSE GAS: THOMAS FERMI TO TONKS-GIRARDEAU

A Thesis in

Physics

By

Trevor Wenger

Submitted in Partial Fulfillment
of the Requirements
for the Degree of

Doctor of Philosophy

May 2007

The thesis of Trevor Wenger was reviewed and approved* by the following:

David S. Weiss
Professor of Physics
Thesis Adviser
Chair of Committee

Kurt Gibble
Associate Professor of Physics

Milton W. Cole
Professor of Physics
Distinguished Professor of Materials Science and Engineering
Distinguished Professor of Physics

Qiang Du
Verne M. Williaman Professor of Mathematics

Jayanth R. Banavar
Professor of Physics
Head of the Department of Physics

*Signatures are on file in the Graduate School.

Abstract:

A set of experiments was performed on a one-dimensional Bose gas system. A 3D Bose-Einstein condensate of ^{87}Rb atoms was formed in an all-optical trap. The BEC was then loaded into a 2D optical lattice that consists of an array of parallel 1D tubes. Measurements of the energy, cloud size, and local pair correlation function probe the properties of the gas from the weak coupling to strong coupling (Tonks-Girardeau) limit. The characteristic property of fermionization of the wave functions was observed in the TG limit.

Another experiment was done to probe the nature on non-equilibrium 1D Bose gases. This integrable system, when placed in a non-equilibrium momentum distribution, was found not to thermalize on the time scale of our experiment (hundreds of trap oscillations or thousands of collisions). This is in stark contrast to the 3D case, which thermalizes on the order of 3 trap oscillations.

Table of Contents:

List of Figures:

Acknowledgments:

I would like to acknowledge my graduate advisor David Weiss. His dedication and passion for science is extraordinary. Also, his great ability to teach and his patience with his students have made it a pleasure to work for him over the years. I would also like to acknowledge my collaborator in these experiments, Toshiya Kinoshita. His dedication to his work is inspiring. Also, I thank my family for all of their support and encouragement.

Chapter 1 : History and Introduction

1.1 Brief history of a Bose-Einstein Condensate

This thesis involves a set of experiments on a Bose Einstein Condensate of ^{87}Rb atoms in one dimension. In 1924 S. Bose correctly evaluated the statistical mechanics of a distribution of photons enabling him to calculate the correct Planck spectrum for black body radiation. Within a year A. Einstein generalized this result to all indistinguishable bosons, regardless of mass, and came up with the Bose-Einstein distribution function:

$$N(E) = \frac{1}{e^{\beta(E-\mu)} - 1} \tag{1.1.1}$$

Here $\beta \equiv \frac{1}{k_B T}$ and μ is the chemical potential. The unique property of this distribution is that at cold enough temperatures the system minimizes its free energy by having a macroscopic occupation of the ground state. This phase transition occurs when the individual particle wave functions start to become significantly overlapped with one another and can be expressed numerically as:

$$n\lambda_{dB}^3 \geq 2.612 \tag{1.1.2}$$

Here λ_{dB} is the de Broglie wavelength and n is the spatial density [7]. This phenomenon manifests itself in superfluidity in liquid ^{4}He and superconductivity.

The developments in the mid 1980's involving laser cooled and trapped atoms led to the ambitious goal of producing a BEC in a dilute gas of alkali atoms. It was first observed in 1995 in Rb [1], Na [3], and Li [2] and is now commonly produced in laboratories all over the world.

A BEC of a dilute atomic gas in a trap cannot be well described without taking into account atomic interactions. To first order these interactions are described by a mean-field repulsive force that arises due to atom-atom scattering. It is added to the Hamiltonian as a term proportional to the density $|\Psi|^2$. The Hamiltonian becomes:

$$\left[-\frac{\hbar^2}{2m}\nabla_{\vec{r}}^2 + V_{trap}(\vec{r}) + NV_{\text{int}}|\Psi(\vec{r})|^2 \right]\Psi(\vec{r}) = E_N\Psi(\vec{r}) \qquad (1.1.3)$$

Here m is the mass, V_{trap} is the confining trap potential, N is the total number of atoms, and $V_{\text{int}} \equiv \frac{4\pi\hbar^2 a}{m}$ is the mean field interaction strength, where a is the s wave atomic scattering length. This is the well-known Gross-Pitaevski equation. The non-linear interaction term leads to many phenomena in BEC physics. One of the main objectives of these experiments is to study quantum degenerate gases in regimes outside of this mean-field limit.

1.2 One dimensional Bose gas

One such beyond mean field regime can be reached by confining the Bose gas to one dimension and inducing strong coupling. This limit is called the Tonks-Girardeau regime. In 1936, Lewi Tonks calculated the equation of state for a classical 1D gas of hard spheres [4]. In 1960, Marvin Girardeau solved the problem of a 1D Bose gas with infinite hard core repulsion [5]. This was followed closely in 1963 by Elliot Lieb and Werner Liniger, who found the exact solutions for a 1D Bose gas with arbitrary strength point-like delta function interactions [6]. The central result of this work is that in 1D, with sufficiently strong interactions, the 1D Bose gas will "fermionize", meaning that individual particle wave functions cease to overlap with one another. Without any wave function overlap, the mean field energy of the gas goes to zero and hence, mean field physics ceases to apply.

Lieb and Liniger showed that the 1D Bose gas is parameterized by the variable,

$$\gamma = \frac{\mu g_{1D}}{\hbar^2 n_{1D}}, \tag{1.2.1}$$

Where μ is the reduced mass of the two identical bosons, g_{1D} is the height of the delta function potential, and n_{1D} is the 1D linear atomic density. The Tonks-Girardeau (TG) limit is reached when $\gamma >> 1$; which can be achieved with strong interactions or low density. Conversely, the mean field (BEC) limit is reached when $\gamma << 1$.

To achieve 1D character for a gas, it must be tightly confined in two transverse dimensions. The extent of 1D character can be quantified by comparing the average

energy per particle to the quantum energy spacing of the transverse potential. As long as the former is much smaller than the latter, no interactions can excite transverse modes. Since the transverse wave functions never change, all of the dynamics in the system are one-dimensional. We achieve 1D trapping in these experiments by crossing two standing wave laser beams, which creates a 2D optical lattice, an array of 1D tubes within which the atoms are trapped in 1D. The mechanism for this 1D trap is the dipole force that light exerts on atoms as described below.

1.3 Brief summary of light forces for a two-level atom

To prepare a BEC of ^{87}Rb atoms, extensive laser cooling and trapping must first be done. The basic effect of a light field on an atom can most easily be seen by considering the interaction of the light field with a two level atom in a semi-classical way. A detailed description of this interaction can be found in Ref. [7] from which the following results are gotten. The light field couples to the atom via the dipole interaction (where the induced dipole of the atom interacts with the electric field of the light). The strength of this coupling is characterized by the Rabi frequency

$$\Omega \equiv \frac{-eE_0}{\hbar}\langle e|\vec{r}|g\rangle \tag{1.3.1}$$

Here e is the electronic charge, E_0 is the amplitude of the electric field in the light wave, e and g are the excited and ground state atomic wave functions respectively and $\vec{r}$ is the electronic coordinate.

Ehrenfest's theorem states that the expectation value of a quantum mechanical operator must correspond to the behavior of its classical counterpart. This leads to the quantum mechanical equivalent of the classical expression that the force is the negative gradient of the potential.

$$F = -\left\langle \frac{\partial H}{\partial r} \right\rangle \tag{1.3.2}$$

Where $H = -e\vec{E}(\vec{r},t)\cdot\vec{r}$ is the Hamiltonian of the system with $\vec{E}(\vec{r},t)$ being the electric field of the laser light. In general,

$$\vec{E}(\vec{r},t) = \vec{\varepsilon}E_0(\vec{r})\cos(wt + \varphi(\vec{r})) \tag{1.3.3}$$

Neglecting the spatial variation of the electric field over the size of the atomic wave packet (electric dipole approximation), assuming the direction of the induced dipole is along $\vec{E}$, and neglecting any terms that oscillate with the laser frequency, ω_l, the result for the force at $\vec{r} = 0$ becomes,

$$\vec{F} = \frac{-\hbar\Omega}{2}\left(A\frac{\vec{\nabla}\Omega}{\Omega} + B\vec{\nabla}\varphi \right) \tag{1.3.4}$$

where A and B are constants that depend on Ω, $\delta = \omega_l - \omega_{atom}$ is the detuning from the atomic transition, and Γ is the lifetime of the excited state.

Specifically,

$$A = \frac{\Omega\delta}{\delta^2 + (\Gamma/2)^2 + \Omega^2/2}, \qquad \text{and} \qquad B = \frac{-\Omega\Gamma/2}{\delta^2 + (\Gamma/2)^2 + \Omega^2/2} \tag{1.3.5}$$

The two terms represent the two forces that light can exert on the atom. The second term is a dissipative force, often called the scattering force, proportional to the gradient of the phase. This results from the scattering of photons by the atoms from a traveling wave. A traveling wave has the form:

$$\vec{E}\ (\vec{r},t) = \vec{\varepsilon}E_0 \cos(wt - \vec{k}\cdot\vec{r}) \tag{1.3.6}$$

And so the first term (proportional to the gradient of the amplitude) vanishes. The scattering process includes the stimulated absorption of a photon by the atom from the light field and the subsequent spontaneous emission of a photon. Stimulated absorption gives the atom a momentum kick of $\hbar k$ in the direction of the laser beam. Spontaneous emission gives an average momentum kick of zero due to the random nature of the spontaneously emitted photon's direction. The irreversibility of spontaneous emission makes the scattering force non-conservative. The whole scattering process gives an average momentum kick of $\hbar k$ in the direction of the laser beam. From the above equations, the scattering force can be written as

$$F_{sc} = \hbar k \Gamma \rho_{ee} \tag{1.3.7}$$

Here k is the wave vector of the light, and ρ_{ee} is the excited state population. Equation (1.3.7) shows that one $\hbar k$ of momentum is transferred to the atom at the spontaneous emission rate, $\Gamma\rho_{ee}$. In terms of the Rabi frequency, it can be written as

$$F_{sc} = \frac{\hbar k s_0 \Gamma / 2}{1 + s_0 + (2\delta / \Gamma)^2}, \tag{1.3.8}$$

where $s_0 \equiv \frac{2|\Omega|^2}{\Gamma^2}$ is the saturation parameter and δ is the detuning of the laser frequency to the atomic transition. This force is important in slowing atoms from the atomic source, and capturing them in an optical molasses.

The first term in equation (1.3.4) corresponds to the dipole force, a conservative force equal to the gradient of the ac Stark shift. The ac Stark shift is proportional to the intensity of the light and inversely proportional to the detuning, δ. In the limit of large detuning, $|\delta| >> \Omega$, the ac Stark shift of the ground state is given by

$$\Delta E_g = \frac{\hbar \Omega^2}{4\delta} \tag{1.3.9}$$

And so the dipole force is given by

$$\vec{F}_{dip} = -\vec{\nabla}(\Delta E_g) = -\frac{\hbar \Omega}{2\delta}\vec{\nabla}\Omega . \tag{1.3.10}$$

In the case of a standing wave field

$$\vec{E}(\vec{r},t) = \vec{\varepsilon}E_0 \cos kz \cos wt \tag{1.3.11}$$

And so the gradient of the phase vanishes and there is only a dipole force. This can easily be seen as the scattering force from the two counterpropagating beams that make up the standing wave cancel each other out. In this case the dipole force is

$$F_{dip} = \frac{2\hbar k \delta s_0 \sin 2kz}{1 + 4s_0 \cos^2 kz + (2\delta/\Gamma)^2} \tag{1.3.12}$$

The sign of F_{dip} depends on the sign of δ, ultimately because the relative phase of the induced dipole of the atom and the oscillating electric field of the light depends on the sign of δ. If $\delta < 0$, they are in phase, so the ac Stark shift is negative and the atom is attracted to regions of high intensity. If $\delta > 0$, they are out of phase, so the ac Stark shift is positive and the atom is attracted to regions of low intensity. This is the force that prevails in our crossed dipole trap and our optical lattices.

Chapter 2: Bose Einstein Condensate Production

In these experiments, we produce a Bose Einstein Condensate of ^{87}Rb atoms using an all-optical method, meaning that only an optical dipole force trap is used for evaporative cooling. Several other groups have made BEC's in optical traps of various types. These include an ^{87}Rb BEC using crossed CO_2 beams (10.6 μm wavelength) [8], a Cs BEC in a crossed CO_2 plus a focused yttrium aluminum garnet (YAG) laser beam (1.064 μm) [9], an Yb BEC in a doubled YAG laser (532nm) crossed dipole trap [10], an ^{87}Rb BEC in a single focused CO_2 beam [11], and a Cs BEC in a two-dimensional YAG laser based optical surface trap [12]. Laser cooling is done on the D_2 line, i.e. the $5S_{1/2}$ to $5P_{3/2}$ transition at 780 nm. The energy level diagram for ^{87}Rb is shown below for reference (Fig. 2.1) [13].

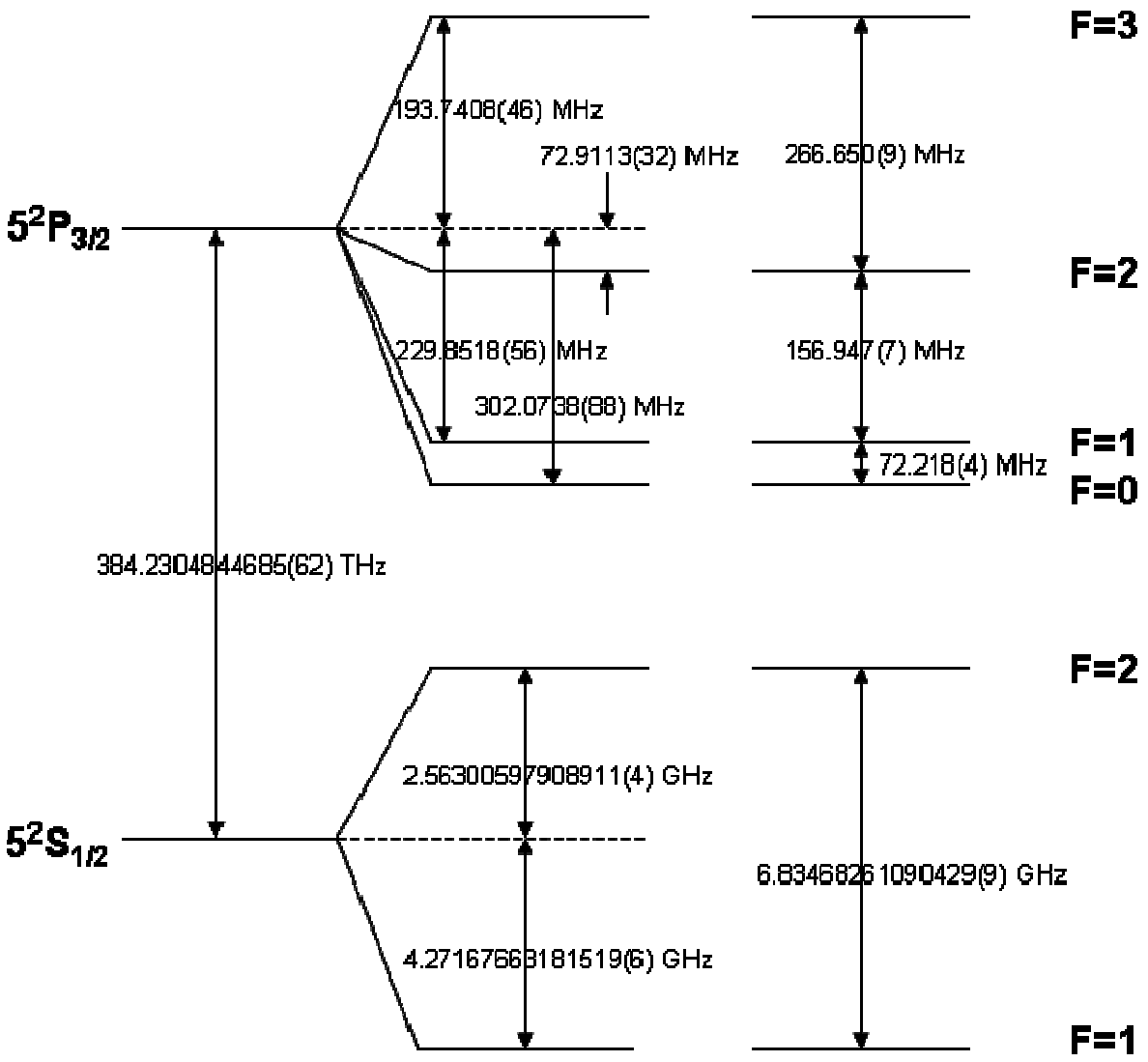

Figure 2.1: The ^{87}Rb D_2 line. The energy hyperfine energy splittings for the $5S_{1/2}$ state are in GHz, for the $5P_{3/2}$ are in MHz, and the fine structure splitting is in THz.

2.1 Slowing atoms from the oven

The first step in the cooling process is to slow the atoms from the oven. The atoms escape from the oven via a small hole. The slowing laser beam is directed head on at the

stream of atoms. As atoms scatter photons from this beam they are decelerated by the scattering force. This slowing beam originates from one of two Ti-Sapphire lasers (Ti-Sapph I). Ti-Sapph I is locked via saturation absorption spectroscopy [14] to the F=2 $\leftrightarrow$ F'=2, F=2 $\leftrightarrow$ F'=3 crossover resonance. This resonance is halfway between the F'=2 and the F'=3 excited state (see Figure 2.1). After double passing through an acoustic-optic modulator (a.o.m.) that can adjust the overall detuning of Ti-Sapphire I, the frequency is detuned to the F=2 $\leftrightarrow$ F'=3 transition with an adjustable range from -40MHz to +60MHz. The beam then double passes through a second a.o.m. with an rf input of 125 MHz, making the detuning -210MHz (f_{main}). The atoms are Doppler shifted into resonance due to their motion with respect to the beam. As the velocity of the atoms decreases, the Doppler shift decreases, and so the detuning must be decreased to keep the atoms in resonance with the light. This is done by adjusting the rf frequency into the first of two electric-optic modulators (e.o.m.) by giving a triangle voltage wave pattern to the voltage controlled oscillator that produces the rf signal. The e.o.m. puts sidebands on the light at plus and minus the rf frequency input; here the plus sideband is what will remain resonant with the atoms. As this frequency is scanned by the triangle wave pattern at about 300Hz, the sideband frequency is scanned from $f_{main} + 0$ to $f_{main} + 200MHz$. In addition, the slowing beam then passes through a 2nd electric-optic modulator with an input rf of 6.835 GHz. This puts sidebands on f_{main} and the 1st sidebands at 6.835 GHz, which depump atoms out of the F=1 ground state so as to keep them optically active to the main slowing beam. This "chirp" slowing method keeps the atoms in resonance with the beam from the oven until they reach the center of the chamber, where they will be captured by the magneto-optic-trap (MOT).

2.2 The magneto-optic-trap

The MOT consists of three pairs of red detuned counter-propagating laser beams (called the optical molasses) from Ti-Sapph I (one pair for each direction), and a magnetic field gradient, produced from a pair of anti-Helmholtz coils, zeroed at the center of the MOT. The polarization of the counter-propagating beams is σ^+, σ^-. Due to the Zeeman shift of the atomic sublevels, as the atoms move away from the center, they become more in resonant with the laser light propagating in the opposite direction and thus feel a restoring force back towards the center of the MOT. A diagram of a one dimensional MOT for an atom with a transition from $F = 0$ to $F' = 1$ is shown below (Fig. 2.2) [7]. This illustrates the basic idea of a MOT, although the actual operation of a 3D MOT is much more complex, with many details not completely understood.

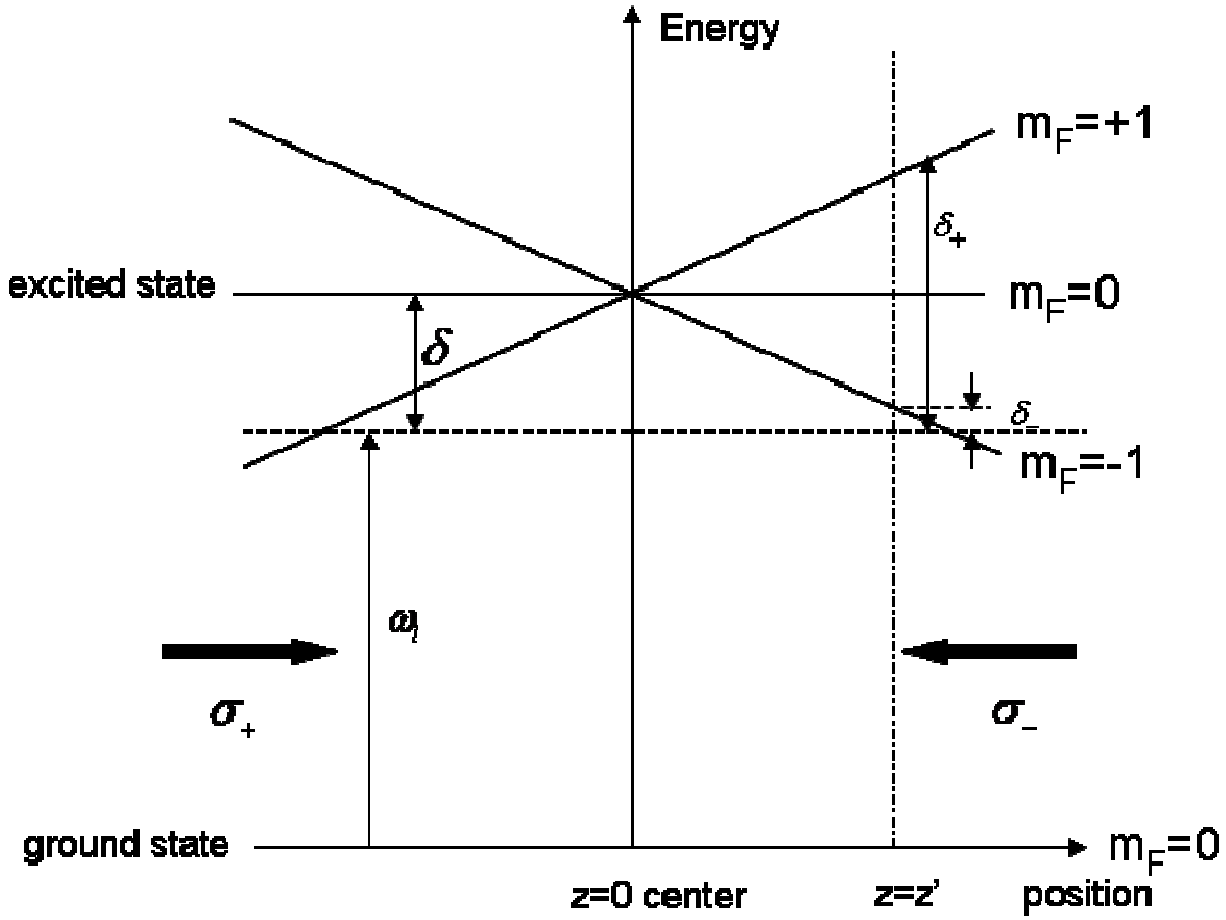

Figure 2.2: Diagram for a 1D MOT. The dashed horizontal line is the laser frequency. The magnetic field pulls atoms to the right of center into resonance with the σ_- beam and atoms to the left of center into resonance with the σ^+ beam.

As shown in the figure, as an atom moves away from the trap center to the right, the Zeeman shift pulls the $m_F = -1$ substate in resonance while pushing the $m_F = +1$ substate out of resonance. The atom is thus more likely to scatter a σ^- photon and get a kick back towards the center. The situation is exactly reversed on the left side. Our molasses beams have an intensity of ~55mW/cm^2 per set of counter-propagating beams and a detuning of -20MHz from the $F = 2, F' = 3$ transition during the slowing phase. The size of the magnetic field gradient is 10 G/cm, achieved by running a current of ~12

amps through each of the MOT coils. There is also a repumping beam to pump atoms out of the $F = 1$ ground state. This beam is from a diode laser locked by saturation absorption spectroscopy to the $F = 1$ to $F' = 1,2$ crossover resonance (see Figure 2.1). After passing through an a.o.m., the repumping beam is nearly resonant with the F=1 to F'=2 transition with an intensity of about 0.36mW/cm^2.

2.3 3D lattice cooling

2.3.1 Compressing the MOT

The next step is to compress the MOT. By increasing the magnetic field gradient, the effective size of the MOT is reduced, thus increasing the atomic density. After 0.8s of loading, the MOT is compressed by increasing the coil current to ~36 amps, making the field gradient 31 G/cm. At the same time the intensity of the molasses light is reduced to 8mW/cm^2 per beam and the detuning is increased to -90MHz. Also the repumping beam intensity is reduced to 0.001mW/cm^2. We reach a peak atomic density of 1.5X10^{12} atoms per cm^3.

2.3.2 Turning on the 3D optical lattice

At this point the magnetic field and optical molasses are turned off and a 3D far-off resonant optical lattice is turned on. The optical lattice consists of three pairs of retro-reflected counter-propagating laser beams produced from a second Ti-Sapphire laser (Ti-

Sapph II). The lattice is blue detuned by 160 GHz and is 300 μK deep. It consists of three orthogonal linearly polarized standing waves with frequencies that differ from 25 to 155MHz so that it is effectively linearly polarized everywhere [15]. This ensures that any pair of beams only interferes with itself and not with another pair. Each lattice beam has a waist of 540 μm and a maximum power of 700mW. Each lattice beam is focused onto the retro-reflecting mirror so that the beam waists of the incoming and retro-reflected beam are equal at the atoms' location. The lattice is turned on suddenly to 60% of its full depth to capture most of the atoms at lattice sites. This is about twice the atoms' thermal kinetic energy. Then it is adiabatically ramped up, with respect to lattice oscillations, to its full depth in 135 μs to bind nearly all of the atoms to lattice sites.

2.3.3 Polarization gradient cooling in the lattice

At this point, the optical molasses is turned back on with a lower power (~5mW/cm^2 per beam), the same detuning, and the repumping is turned off. Polarization gradient cooling takes place and cools the atoms to the lowest few vibrational levels of the lattice. A brief description of the polarization gradient cooling process is as follows; a detailed description can be found in reference [7].

The polarization gradient cooling (PGC) is done by the optical molasses light, whose counter-propagating beams have σ^+, σ^- polarizations. This PGC scheme is a bit more complicated than the orthogonal linear polarization scheme. A detailed description of the latter can be found in reference [7], where a less detailed overview of the former can also be found. Both are summarized below. Basically, PGC relies on a spatially dependant

polarization of the red detuned light field. The ac Stark shift of the different ground magnetic substates depend on the polarization of the light through the transition matrix elements. In the orthogonal linear PGC scheme, the polarization changes from σ^+ to σ^- in a quarter cycle of the wave. It turns out that the optically pumped state always has a larger shift than the depleted state. As the atoms travel through a quarter cycle they are going up a potential hill, thus losing energy, until they reach the opposite polarization. Here they are optically pumped to the opposite magnetic sublevel, which in the new polarization now has the larger shift, and thus the process repeats itself. This is the so called "Sisyphus cooling".

For the σ^+,σ^- PGC scheme, the wave that results is everywhere linearly polarized but rotates through an angle of 2π in one wavelength. Since the polarization is always linear, the ac Stark shifts are constant spatially, and so "Sisyphus cooling" cannot occur. Moving atoms experience a rotating polarization and hence a rotating quantization axis (in order to stay in the same basis). This rotation causes a redistribution among the ground magnetic substates (of F=2 in our case) that lags behind the equilibrium distribution appropriate to the local polarization direction. Dalibard & Cohen Tannoudji showed that this redistribution favors positive m_F levels when moving toward the σ^+ light and negative m_F levels when moving toward the σ^- light [16]. In the case of the F=2 ground state, the $m_F = 2$ state has a 15 times stronger matrix element than the $m_F = -2$ state and hence scatters σ^+ photons 15 times more likely than σ^- photons [7]. The situation is reversed for atoms moving toward the σ^- light, preferentially scattering more σ^- photons. This mechanism is different than Doppler shift cooling, in that it involves preferentially scattering from a beam due to population imbalance and stronger

matrix elements, not just a frequency shift due to the atomic velocity. It has a much smaller velocity capture range, but a much stronger restoring force than Doppler cooling.

2.3.4 Optical pumping and lattice turn off

At this point we optically pump the atoms to the F=1, m_F =1 hyperfine sublevel with an efficiency of about 95%. We determine the population by, after optical pumping, releasing the atoms in a magnetic levitation field. The m_F=1 sublevel is levitated while the other sub levels (m_F=0 and -1) will drift downwards due to gravity and imperfect magnetic field gradient levitation. By taking an image after expansion we can see three separate populations and thus measure their relative populations. The optical pumping beam is circularly polarized, σ^+, and originates from the repumping diode laser. It is oriented in the vertical direction, perpendicular to the optical table, and cycles atoms on the F=1 to F'=1 transition. The σ^+ light allows only $\Delta m_F = +1$ transitions during absorption while the spontaneous emission can have $\Delta m_F = -1,0,+1$. This on average moves the magnetic substate towards $m_F = +1$. The optical pumping light is on for 2.5ms. During this time there is also depumping light on that transfers atoms out of the F=2 ground state. This beam originates from Ti Sapph I. Both beams have a very low intensity.

After optical pumping, the lattice is adiabatically turned off with respect to lattice oscillations. This results in a decrease in kinetic energy to 1.5 μK, a density of $5X10^{11}$ atoms per cm^3 and a phase space density of 1/550 where the phase space density is defined as $\rho = n\lambda_{dB}^3$.

2.4 Crossed Dipole YAG trap

2.4.1 YAG trap equations

The atoms are then loaded into the compressible cross dipole YAG trap. This trap consists of two perpendicular laser beams parallel to the optical table produced from a yttrium aluminum garnet (YAG) laser with a wavelength of 1064 nm. The YAG beam passes through an acoustic optic tunable filter (a.o.t.f.) which creates the two beams and gives a frequency difference of 24MHz to avoid interference. The intensity varies transversely to both beams as $I(r) = I_0 e^{\frac{-2r^2}{w_0^2}}$, where r is the radial coordinate and w_0 is the laser beam waist. Using equation (1.3.9) and the definition, $s_0 = \frac{2|\Omega|^2}{\Gamma^2} = I / I_s$, the potential is

$$U_{trap}(r) = \frac{\hbar \Gamma^2 I(r)}{8 \delta I_s} \tag{2.4.1}$$

Where $I_s \equiv \frac{\pi h c}{3 \lambda^3 \tau}$ is the on resonant saturation intensity with λ being the atomic transition wavelength and τ being the excited state lifetime. The peak depth at the center of the trap is,

$$U_{trap}^{0} = \frac{\hbar \Gamma^2 I_0}{8 \delta I_s} \quad , \tag{2.4.2}$$

where $I_0 = 2\frac{2}{\pi}\frac{P}{w_0^2}$, and P is the total power in each laser beam.

2.4.2 Compressing the YAG trap

To start the evaporative cooling process, we first must obtain a high enough atomic density so that evaporation increases the phase space density more rapidly than heating and loss decrease it. Such density increases in optical traps have been attained in essentially two ways. In Ref's [8, 10], the numerical aperture of the focused crossed dipole beams is large, so the beams diverge sharply near the waists. The result is that many more atoms are loaded into the arms of the trap than into the crossed region. These atoms in the arms experience a large restoring force into the crossed region so that when they arrive, unforced evaporative cooling proceeds quickly, leaving a high-density remnant of atoms [17]. Both in Ref. [9] and in this experiment, atoms are loaded directly into a large volume crossed dipole trap and then the trap shape or size is dynamically changed. In Ref [9], they add an additional "dimple" laser beam to increase the collision rate of atoms to enhance evaporation. In this experiment, we use a zoom lens to adiabatically decrease the size of the trap to increase the atomic density.

Our movable zoom lens system is shown below (Fig. 2.3). The size of this trap can be controlled by the position of the movable lens [18].

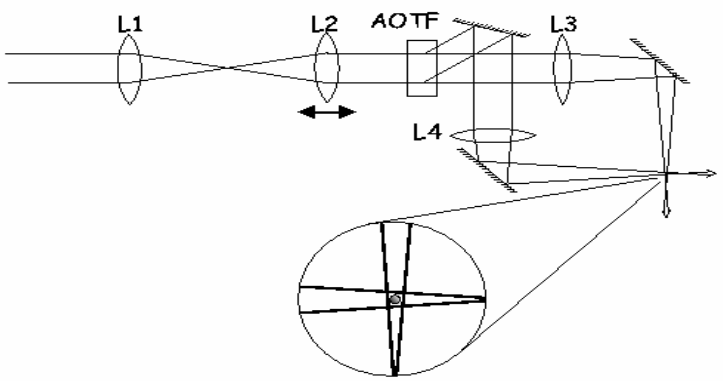

Figure 2.3: Diagram of the optical system for the compressible crossed dipole trap. Computer-controlled translation of lens L2 changes the waist of the beams at their crossing point. The beams are divided and frequency shifted with an acousto-optic tunable filter (AOTF).

The YAG beams each have a power of 3 W and a waist of 300 μm during the loading of the atoms. The depth of this trap is 3 μK , thus trapping most of the atoms. To balance the gravitational potential shift across the beam profile of 31 μK , a vertical magnetic field gradient is applied using the MOT anti-Helmholtz coils, which also produces a bias field of 23 Gauss for the optical pumping described above.

We compress the YAG trap from the original 300 μm to 50 μm in 0.6s (adiabatic with respect to the trap oscillation frequency) in a two step process. The result is a factor of 200 reduction in the trap volume, which increases the thermalization rate sufficiently for evaporation to begin. It is important to note that during this adiabatic compression,

the entropy remains constant, which means the ratio of the temperature T to the trap depth U remains constant. This can be seen as follows. With fixed power the trap depth, $U \propto w^{-2}$, where w is the beam waist. The trap oscillation frequency is $\omega \propto \sqrt{U} w^{-1}$. For the adiabatic change, the atoms stay in the same vibrational levels of the trap, so $T \propto \omega \propto \sqrt{U} w^{-1} \propto w^{-2}$, i.e. the same as U. The thermalization rate increases very efficiently by the compressed trap method. The phase space density, $\rho \propto nT^{-3/2}$, where n is the spatial density, also remains constant during adiabatic changes in the trap size. Therefore n increases when w is decreased by, $n \propto T^{3/2} \propto w^{-3} \propto V^{-1}$, where V is the volume. The thermalization rate, $\Gamma \propto nT^{1/2} \propto V^{-4/3}$, increases by a factor of over 1000 due to the 200 factor reduction in the trap volume.

2.4.3 Forced evaporation

200ms after the start of compression, we begin the evaporation process, which simply consists of lowering the YAG trap depth and allowing the hottest atoms to escape. The rate with which the depth is lowered is governed by the slower of two times; the oscillation frequency in the trap and the thermalization time. The trap depth is lowered according to the equation,

$$P = \frac{P_0}{\left(1 + t/t_0\right)^2}, \tag{2.4.3}$$

which is derived from the adiabatic condition of $\frac{1}{\omega}\frac{d\omega}{dt} << \omega$, where ω is the YAG trap frequency. In total, we reduce the trap depth by a factor of 243 from the initial power of 3W per beam in 5 independently optimized steps, each decreasing the power by a factor of 3. The optimal time constant for each "step" of evaporation is empirically determined and becomes slower as evaporation proceeds, going from a time constant of 300ms for the 1st evaporation to 1400ms for the last evaporation. The initial horizontal trap frequency during loading is 17 Hz. During compression and evaporation, the calculated spontaneous emission rate reaches a maximum of 0.4 Hz. The final trap frequency is 40Hz with a negligible spontaneous emission rate of 0.0065 Hz.

There are actually three potentials present during this process, the dipole trapping potential, the potential due to the bias field, which is antitrapping, and the gravitational potential. The gravitational potential is cancelled by the magnetic gradient field as described above. The combined effect of the dipole trap and the magnetic antitrap is to produce a lip around the edge of the trap, which has the salutary effect of preventing atoms that have left the trap from returning.

Due to the crossed beam configuration of the dipole trap, the trap is twice as deep in the vertical direction as the horizontal direction. This makes the effective dimension of the evaporation about halfway between two (atoms escaping from a ring) and three (atoms escaping from a closed surface) [19]. For efficient evaporation atoms must be able to escape from all points of the trap symmetrically. To ensure this, the atoms must be located at the zero slope point of the magnetic antitrap. We adjust the transverse bias fields produced by two sets of Helmholtz coils so that the atoms do not drift in the transverse direction after the YAG trap is shut off. This is done by turning off the YAG

trap and letting the atoms expand in the levitation field. By imaging the atoms from above and the side, we can tell if they drift in some horizontal direction and correct it by adjusting the coil currents.

Figure 2.4 shows the evaporation process. The phase space density increases nearly exponentially and BEC is reached when the YAG power is reduced by a factor of 30.

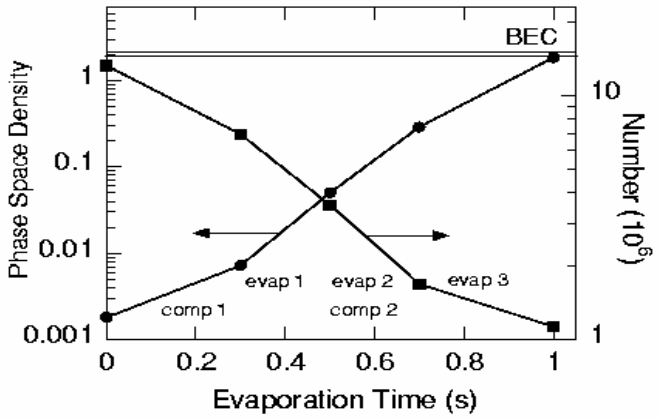

Figure 2.4: Phase-space density during compression and evaporation. There are two compressions, first to 120 μm waist, then to 50 μm. Evaporation takes place in five stages, and BEC is reached immediately after the third stage.

For our specific trapping configuration the phase space density is calculated using the following formula,

$$\rho = \frac{N}{\pi^{3/2}\sigma_r^2\sigma_z}\left(\frac{2\pi\hbar^2}{mk_BT}\right)^{3/2}, \qquad (2.4.4)$$

where σ_r and σ_z are the effective size of the trap transversely and vertically respectively and N is the atom number.

$\sigma_{rz} = \sqrt{\frac{2k_B T}{m\omega_{rz}^2}}$, where ω_{rz} is the transverse or vertical trapping frequency.

$\omega_r^2 = \frac{4U_0}{mw_0^2}$, where w_0 is the YAG beam waist and U_0 is the depth; $\omega_z = \sqrt{2}\omega_r$.

Figure 2.5 shows standard absorption images of atoms suddenly released from the YAG trap and allowed to expand for 20 ms at different times during the evaporation process.

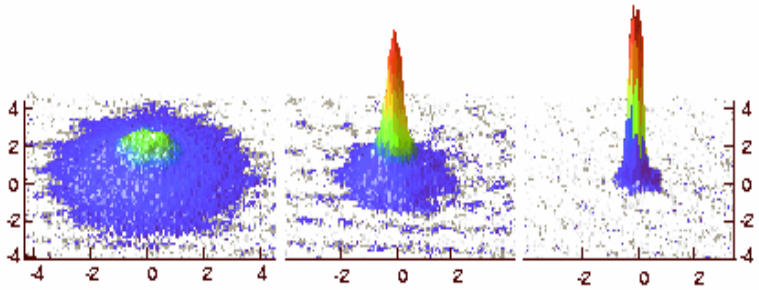

Figure 2.5: Absorption images of the atom distribution at various evaporation stages. (a) After 1s, just before the BEC transition. (b) After 1.6s, with half the atoms in the BEC. (c) After 2.6s, a nearly pure BEC. The atom number is color coded and shown on the vertical axis. The horizontal units are Rb photon recoil momentum (the size of the cloud before expansion is much smaller than after expansion).

Figure 2.5 (c) shows, after 2s of evaporation, a >90% pure BEC with $2.5X10^5$ atoms. The signature BEC spike can be seen, emerging due to macroscopic occupation of the ground state of the trap. At this point the mean field dominated energy of the atoms is about 7.5 nK . Since this data was taken, further optimization has yielded, in the same evaporation time, a >98% pure BEC of $3.5X10^5$ atoms. The entire process from start to finish takes about 3.3s, which is very convenient for averaging the signal over several runs. Having achieved a degenerate gas of bosons, we are ready to load the atoms into 1D.

Note1: The absorption images are taken by illuminating the atoms with a low intensity probe beam. The atoms cast a shadow onto the beam which is proportional to the optical thickness of the atoms. From our side view, the signal is integrated over one horizontal direction, so that what we see is proportional to the density of atoms as a function of the other horizontal direction and the vertical direction. Because our trap is cylindrically symmetric, we can safely assume the integrated horizontal direction has the same density profile as the one we can see. The images in Figure 2.5 are then tilted so that the color scale can be seen as a dimension. See Reference [18] for more details.

Note2: The main improvement in the BEC production occurred as a result of an improvement of the vacuum from $\sim 6x10^{-10}$ to $\sim 3x10^{-10}$. This was achieved by the

installation of a new titanium sublimation pump that replaced the older, broken one. The time constants for evaporation were then readjusted, however, the ones quoted above are the latest, optimized ones.

Chapter 3 : 1-dimensional Bose Gas

Once a nearly pure BEC is achieved, we want to study the gas in one dimension. We accomplish this with a 2D optical lattice. By ramping up the lattice beams adiabatically with respect to the lattice oscillation frequency, we can go from a 3D BEC with low entropy to a 1D Bose gas with comparably low entropy.

3.1 Brief overview of experimental 1D trapping system

Figure 3.1 shows a schematic of the light traps that create 1D gases. Our 2D optical lattice consists of two retro-reflected laser beams (blue beams in Fig. 3.1) produced from the lattice Ti-Sapphire laser (Ti-Sapp II). The two standing waves are mutually perpendicular and horizontal (i.e. parallel to the optical table). The beams are blue detuned by 3.15THz and have a frequency difference of 130MHz with respect to each other to avoid interference between standing waves. This configuration creates an array of 1D tubes oriented vertically. The crossed dipole trap (red beams in Fig. 3.1) remains on, providing harmonic confinement in the 1D vertical direction.

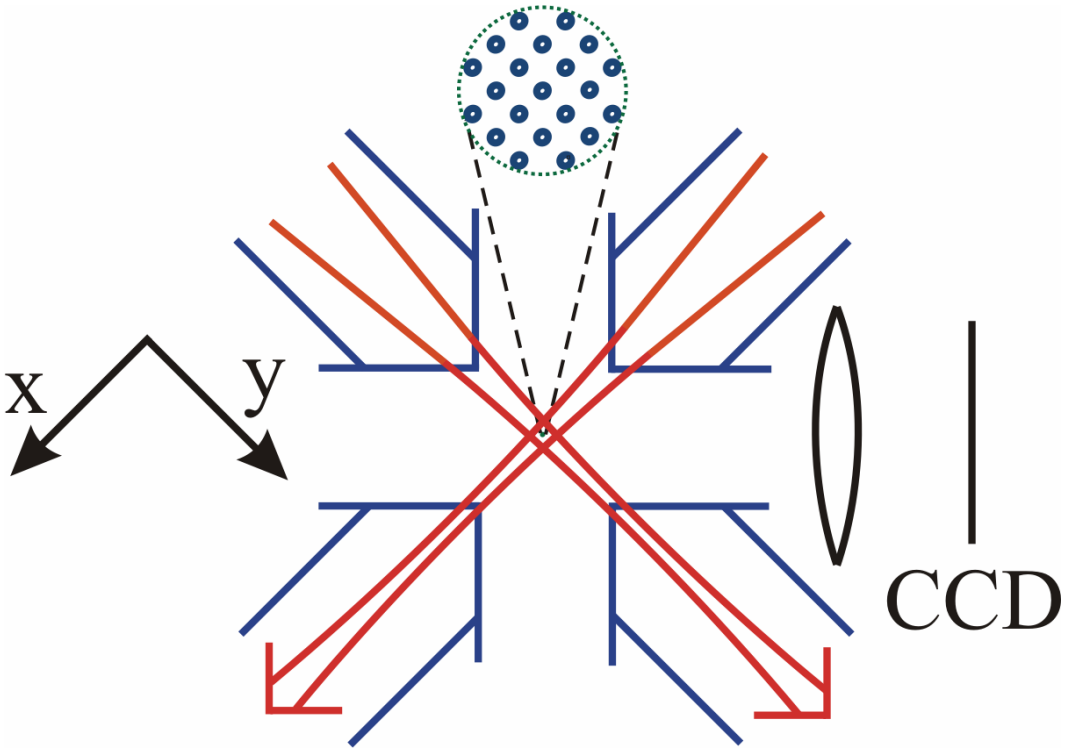

Figure 3.1: Schematic of 1D trapping system showing the crossed dipole YAG trap (red), and the 2D optical lattice (blue). The array of one dimensional tubes (blow up) comes out of the page.

As is shown in Fig. 3.1, we image the atoms from the side of the 1D tubes. The blue detuned lattice has two main advantages. First, since the atoms are located at intensity minima, the spontaneous emission is greatly reduced. Second, we can change the intensity of the lattice without significantly affecting the confinement in the 1D axial direction, which is nearly completely provided by the YAG trap. That is, the antitrap from the blue detuned Gaussian profile of the lattice beams is small compared to the YAG confining potential, constituting at most a 2.8% correction.

3.2 One dimensional Bose gas theory

These experiments create 1D gases because there are no dynamics in the transverse (radial) direction. The energy per particle of the atoms is much less than the harmonic oscillator energy spacing, which ensures that no atoms are excited from the transverse ground state. In our case the typical energy per particle after loading into the 2D lattice is 10's to 100's of nK depending on the density, while the harmonic oscillator energy spacing for full lattice power is 3.4 μK .

3.2.1 One dimensional Hamiltonian and gas parameter

In 1D, a dense, weakly interacting Bose gas behaves like a BEC, in as much as there is a macroscopic occupation of the ground state of the system. However, when the gas becomes dilute and strongly interacting, the atoms begin to repel one another, acting as if they were noninteracting fermions [5, 20]. This is known as a Tonks-Girardeau (TG) gas [4, 6] and provides an example of the importance of correlations among wave functions in a many body system.

The Hamiltonian for a 1D system with arbitrary strength delta function interactions between particles is

$$H_{1D} = \sum_{particles} \left(\frac{-\hbar^2}{2\mu} \frac{\partial^2}{\partial z^2} + g_{1D}\delta(z) \right), \tag{3.2.1}$$

where μ is the reduced mass and g_{1D} is the coupling strength. Lieb and Liniger first addressed this Hamiltonian in 1963 [6]. They developed exact solutions for all coupling regimes, characterized by the dimensionless parameter,

$$\gamma = \frac{\varepsilon_{\text{int}}}{\varepsilon_{kin}}, \tag{3.2.2}$$

where ε_{int} and ε_{kin} are the average interaction and kinetic energies calculated with mean field theory. This ratio becomes, $\frac{\varepsilon_{\text{int}}}{\varepsilon_{kin}} = \left(\frac{r^2}{l_c^2}\right)$, where $r = 1/n_{1D}$ is the interparticle spacing and l_c is the correlation length. The correlation length is the de Broglie wavelength associated with the mean field energy, $\varepsilon_{\text{int}} = 1/2g_{1D}n_{1D}$. So that

$$l_c = \frac{\hbar}{\sqrt{\mu g_{1D} n_{1D}}}. \tag{3.2.3}$$

The coupling parameter can be reexpressed as

$$\gamma = \frac{\mu g_{1D}}{\hbar^2 n_{1D}}. \tag{3.2.4}$$

3.2.2 Strong coupling regime

In the limit of high gamma, $\gamma >> 1$, the system is in the strongly coupled TG regime. The repulsive interactions are so large that the system minimizes energy by localizing

particles with respect to each other. The result is that the wavefunction overlap is minimal (asymptotically going to zero), and the dominant energy is the kinetic energy associated with localizing particles on a line. This can be seen schematically in Fig. 3.2.

Figure 3.2: One dimensional Bose gas in the TG regime. Although single particle wave functions are delocalized, the cartoon illustrates that the probability of any two wave functions being observed in the same place goes to zero.

It is important to note that the particles aren't localized in the sense that individual particle wave functions are distinct. They still are spread across the entire gas. However, the probability of finding any two particles at the same position (i.e. the second order correlation function $g_2(0)$) goes to zero, just as for a gas of non-interacting fermions. Also note that the strongly interacting regime in 1D occurs at low density, while in 3D it occurs at high density. The vanishing probability of finding two particles in the same place in the TG regime means that there are no number fluctuations in space, which implies the loss of long range phase coherence. The TG gas is in this way similar to the Mott insulator phase of a gas in a periodic potential, except for the lack of diagonal long range spatial order [21, 22].

3.2.3 Weak coupling regime

In the limit of low gamma, $\gamma << 1$, the system is in the weakly coupled mean field (Thomas-Fermi) regime. In this case the energy cost of having wave functions overlap is small compared to the kinetic energy of localizing particles, and so the dominant energy is mean field energy. Wave function overlap is considerable in this regime and the system behaves much like a BEC (i.e. exhibits long range phase coherence); see Fig. 3.3.

Figure 3.3: One dimensional Bose gas in the mean field regime. As in a 3D BEC, there are weak correlations among the single particle wave functions, and the local pair correlation is one.

3.3 One dimensional Bose gas theory in experimentally relevant systems

The next step is to adapt this 1D theory to actual experimental systems. This was done by Olshanii et al [23] when they adapted the Lieb Liniger theory to a 1D gas in a cigar shaped trap with harmonic transverse trapping. The result is that

$$\gamma = \frac{2a_{3D}}{a_\perp^2 n_{1D}}\left(1 - \frac{Ca_{3D}}{\sqrt{2}a_\perp}\right)^{-1} = \frac{2}{n_{1D}|a_{1D}|}, \tag{3.3.1}$$

with $a_{1D} = \left(\frac{-a_\perp^2}{a_{3D}}\right)\left(1 - C\frac{a_{3D}}{\sqrt{2}a_\perp}\right)$ being the 1D scattering length.

Here, $a_{3D} = 5.3nm$ is the 3D atomic scattering length, $a_\perp = \sqrt{\frac{\hbar}{m\omega_r}}$ is the transverse oscillator length, and $C \approx 1.46$ is a constant. Since typically, $a_\perp = 40nm$,

$$\gamma \approx \frac{2a_{3D}}{a_\perp^2 n_{1D}}. \tag{3.3.2}$$

In our system we can increase gamma by decreasing the 1D density, decreasing the transverse oscillator length (i.e. increasing the confinement by increasing the lattice power), or increasing the 3D scattering length. The latter could be done using a Feshbach resonance, which we did not do. We control gamma by changing the 1D density and 2D lattice power. We scan gamma across nearly an order of magnitude (from near zero up to ~11) and observe the effect of strong coupling on such quantities as the energy per particle and the 2nd order correlation function. The 1D density is varied by changing the power of the crossed dipole YAG trap either before (to change the number of atoms per tube N_{tube}) or after (to change the axial confinement in 1D) the lattice ramp up.

Considering the addition of harmonic axial confinement, Olshanii et al calculate the 1D density using mean field, Tonks-Girardeau, and the exact 1D Bose gas theory [24],

the latter being valid across all coupling regimes. This gives definitions for the gas parameter as follows:

$$\gamma_{TF} = \frac{2}{n_{TF}^{0}\left|a_{1D}\right|} = \frac{2}{\eta} \quad ; \quad \gamma_{TG} = \frac{2}{n_{TG}^{0}\left|a_{1D}\right|} \quad ; \quad \gamma_{exact} = \frac{2}{n_{exact}^{0}\left|a_{1D}\right|} \tag{3.3.3}$$

where the densities used are the peak 1D densities. The first and last expressions will be used later. Appendix D contains expressions for the densities in the TF and TG regimes as well as η. It also contains the calculation of γ_{avg} across the array of tubes which will be described in the next chapter.

Chapter 4 : Experimental Observation of the Tonks-Girardeau Regime

To experimentally observe the TG regime we looked at two features of the 1D Bose gas, the total 1D energy, and the local pair correlation function. We looked at both features across coupling regimes, from the BEC regime to the TG regime, up to $\gamma \approx 11$ for the latter.

4.1 Qualitative discussion of coupling regimes

Fig. 4.1 shows a cartoon of the 1D atomic distributions in the limiting and intermediate γ regimes.

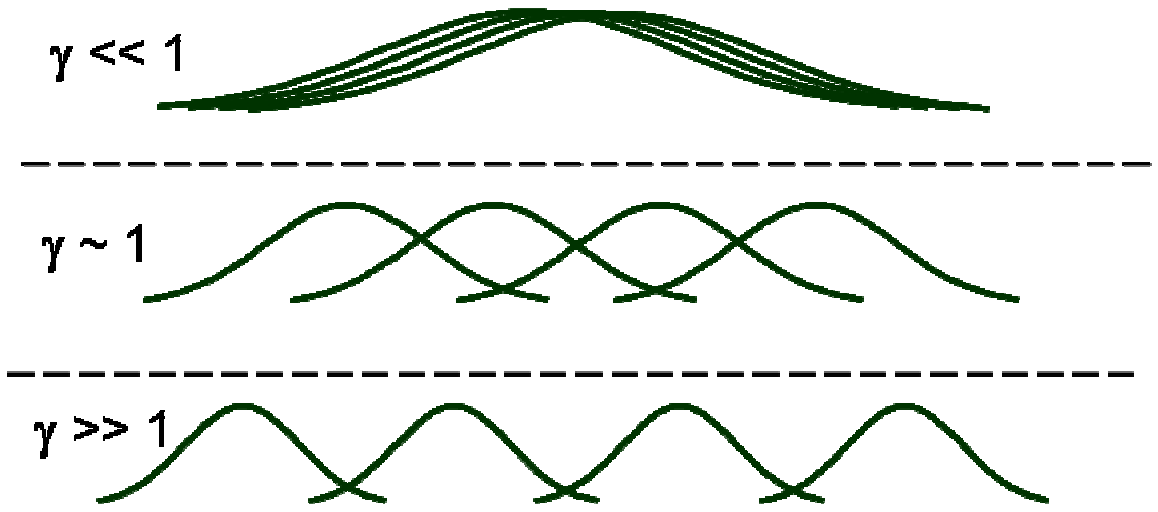

Figure 4.1: Cartoon of 1D atom distributions. The extent of the wave functions in the drawings represent the correlation lengths of the atoms. As γ increases, the correlation lengths approach the interparticle spacing. When γ exceeds 1, the kinetic energy associated with maintaining the correlations in the wavefunctions , which make them less likely to be found in the same place, exceeds the mean field energy, which is associated with their overlap. For very large γ, the probabilty of measuring two particles in the same place is zero, even though the size of the single particle wavefunctions greatly exceeds the interparticle spacing.

When $\gamma << 1$, the system is in the BEC regime, where there is substantial wave function overlap, and the coherence length $l_c >> r$, the interparticle spacing. In this regime if you increase the transverse confinement, effectively squeezing the cloud, the mean field energy will increase and the cloud length will get larger. Squeezing the cloud will continue to increase γ. By the time $\gamma \approx 1$, $l_c \approx r$. Even though individual wavefunctions spatially extend across the entire atomic cloud, the probability of finding two particles in the same place decreases. By the time $\gamma >> 1$, the wave function overlap is zero, i.e., bosons are fermionized. l_c becomes smaller than the interparticle spacing and hence ceases to have any meaning. At this point, further squeezing of the cloud has no effect on either the 1D energy (since there is no mean field energy left to increase) or the 1D cloud length.

4.2 Turning on the 2D optical lattice

To create 1D systems, we must turn on the 2D lattice adiabatically. We increase the lattice power exponentially to achieve this. The lattice must be turned on slowly enough to avoid the excitation of 1D breathing modes, keeping the atoms in the axial ground state. Although an exponential is not the optimal functional form for turning on the lattice, we found it easiest to implement and sufficiently slow to satisfy the above condition. We ensure this by looking at the in situ cloud size after various holding times in the lattice. We turn on the lattice slowly enough, that the amplitude of the oscillations in cloud size are less than 10% of the cloud size. We checked that the atoms are still near zero temperature by ramping the lattice back down after turning it on and checking the purity of the 3D BEC in the crossed dipole YAG trap. We found that ~80% of the atoms return to the BEC, setting a clear bound on the entropy introduced by non-adiabatic lattice changes.

The lattice beams have a 600 μm waist, are detuned 3.2 THz blue from the D2 line, and have a maximum power of 700mW per beam. This gives a maximum depth for the lattice of $U_0 = 16\mu K = 87E_{rec}$ where $E_{rec} = \frac{\hbar^2 k^2}{2m} = 180nK$ is the atoms recoil energy, $k = \frac{2\pi}{\lambda_{lat}}$ is the lattice wave vector. The maximum transverse oscillation frequency is $\frac{\omega_\perp}{2\pi} = 70.7kHz$. As discussed in Chapter 3, the axial oscillation frequency ω_z is only very weakly affected by the lattice antitrap in the 1D direction ($\leq 2.8\%$). Therefore, we can scan the lattice power, thus scanning γ, without significantly affecting the axial

confinement. Additionally, the very large lattice beam waist compared with the initial cloud size (~12 μm) means that both $\omega_\perp$ and ω_v are nearly the same for each of the ~6400 occupied 1D tubes. The tubes differ only in the number of atoms they contain, which depends on the distribution among the tubes at the superfluid to Mott insulator transition they must undergo during the lattice turn-on [54].

4.3 1D energy measurement

To measure the 1D energy per particle, we suddenly shut off the 1D trap, and observe the ballistic expansion while the atoms are still in 1D, that is, while the 2D lattice is still on. The total energy is the sum of the mean field energy, and the kinetic energy associated with localization. We took two sets of data at different initial atomic densities. For each set, we scanned the lattice power from very nearly 0 up to 87 E_{rec}, thus scanning γ. When we reach BEC in the YAG trap, each YAG beam has a 50 μm waist, and a power of 12mW. For this data, we then decompress the YAG trap to a waist of 70 μm. For the low density, high γ data we simply turn on the lattice at this point with a time constant of 20ms. For the high density, low γ data we increase the YAG power to 320mW before turning on the lattice with a time constant of 3 ms. At the low initial atomic density, we can reach a γ_{avg} of ~5.5 (TG regime), where γ_{avg} is the average value of γ over all of the 1D tubes. At the high initial atomic density, we reach γ_{avg} as low as ~0.2 (BEC regime).

4.3.1 Measuring the 1D energy

To measure the 1D energy, ε, we suddenly turn off the YAG trap after the 2D lattice is turned on, and let the atoms expand ballistically in the 1D tubes for 7 and 17 ms. From this we can get a 1D temperature,

$$T_{1D} \propto \frac{\Delta V_2^2 - \Delta V_1^2}{t_2^2 - t_1^2}, \tag{4.3.1}$$

where ΔV is the 1/e^2 cloud width in the 1D vertical direction after expansion, and t is the expansion time. The 1D energy is $\varepsilon_{1D} = 1/2k_B T_{1D}$.

4.3.2 Calculating the average γ

We image the tubes from the side with high intensity fluorescence imaging onto a ccd camera. The resonant light is 3000 times above saturation intensity, and is pulsed on for 25 μs, short enough that the cloud does not expand significantly during this time. Typically, the average of 5 images is recorded. We integrate the signal transverse to the tubes, thus getting the average over the tubes of the 1D distribution. This turns out to fit very well to a Gaussian even though the individual 1D distributions are parabolic (BEC regime), or square root of a parabola (TG regime). We calculate the average gamma, γ_{avg}, over all tubes by calculating

$$\gamma_{tube} = \frac{2}{n_{0TF}\left|a_{1D}\right|}, \tag{4.3.2}$$

where n_{0TF} is the peak 1D density calculated using mean field theory,

$$n_{0TF} = \left(\frac{9}{64} N_{tube}^2 (m\omega_Z / \hbar)^2 \left|a_{1D}\right|\right)^{1/3} \quad [24] \tag{4.3.3}$$

and $a_{1D} = \frac{-a_\perp^2}{a_{3D}}\left(1 - C\frac{a_{3D}}{\sqrt{2}a_\perp}\right)$. We calculate γ_{tube} for each tube and do a weighted average over the number per tube dependence of

$$N_{tube} = N_{tube\max}\left(1 - \frac{r^2}{R^2}\right), \tag{4.3.4}$$

where $r_{\max}$ is the 3D radial cloud length calculated from mean field theory.

$$R = \sqrt{\frac{2\mu}{m\omega_r^2}} \quad [25] \tag{4.3.5}$$

Where the chemical potential is,

$$\mu = \left(\frac{15\hbar^2\sqrt{m}}{2^{5/2}} N\sqrt{2}\omega_r^3 a_{3D}\right)^{2/5} \quad [25] \tag{4.3.6}$$

Equation 4.3.4 assumes a parabolic distribution of atoms among tubes. This is undoubtedly not a perfect assumption. There is some rearrangement of atoms among tubes during the early stages of the lattice turn on, when the system is still on the superfluid side of the superfluid-Mott insulator transition. However, as we shall see later, the final result for γ_{avg} is quite insensitive to the initial distribution of atoms among tubes.

4.3.3 1D energy results

Fig. 4.2 shows the results for the two sets of data, (a) is low density and (b) is high density.

a)

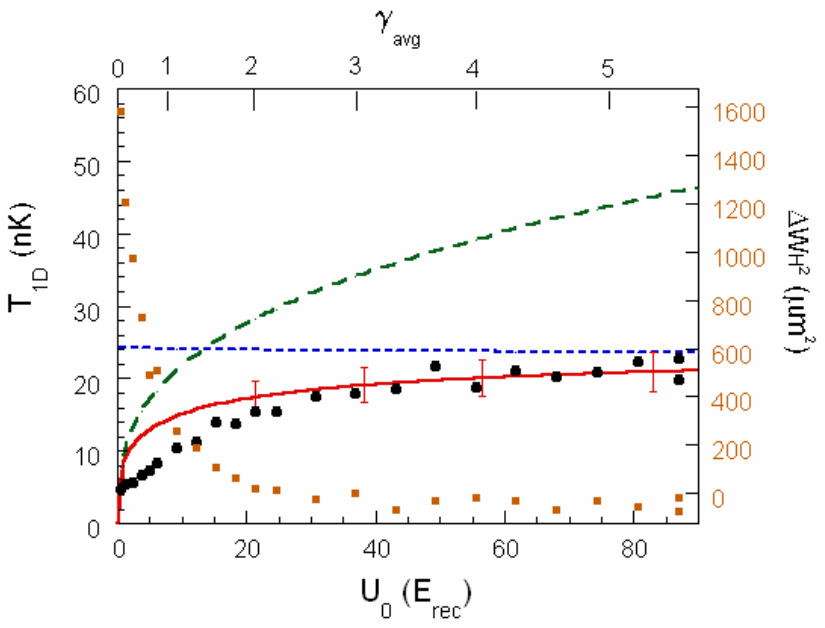

b)

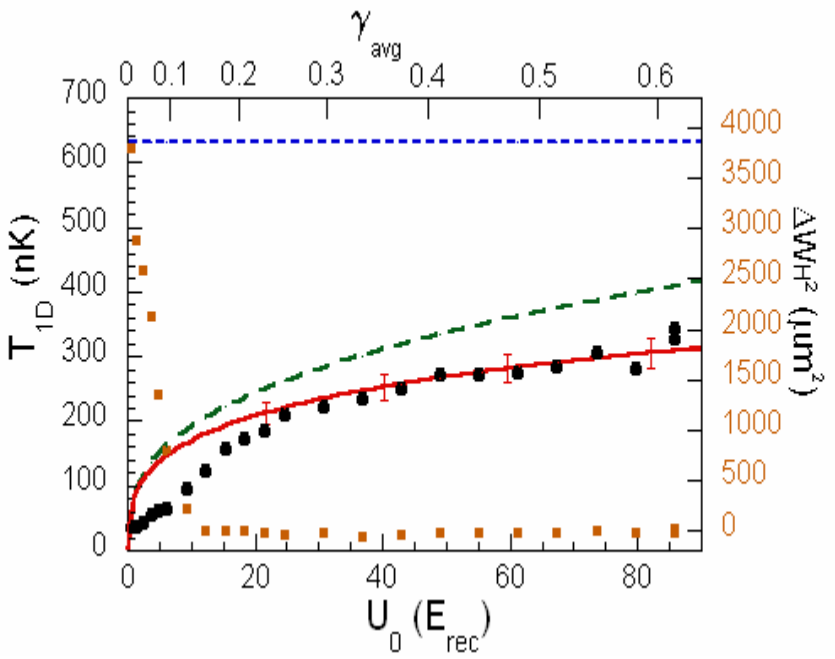

Figure 4.2: Plot of the 1D temperature versus the transverse confinement. (a) At P=12mW, the atoms act like a TG gas. (b) At P=320mW, the atoms act like a BEC. The circles denote T_{1D}, which is proportional to ε. TG theory curves (short-dashed line) are valid for $\gamma >> 1$, mean field theory curves (long-dashed line) are valid for $\gamma << 1$, and exact 1D Bose gas theory curves (solid line) are valid for all values of γ. The theory curves have no free parameters. Error bars in the theory curves reflect uncertainty in the input experimental parameters, the most important being the crossed dipole trap size ($\pm 2\mu m$) and , secondarily, the atom number ($\pm 10\%$). The solid squares represent the change in the square of the horizontal width, Δw_h^2, measured from 7 to 17ms after the crossed dipole trap has been shut off. The system is purely 1D only above $U_0 \sim 20E_{rec}$, when the interaction between tubes is negligible.

The black circles are the data, the solid line curve is the 1D temperature calculated using the exact theory as a function of U_0 and N_{tube}. The dashed line curve is the 1D temperature calculated using mean field theory (valid for $\gamma << 1$) and the dotted line curve uses TG theory (valid for $\gamma >> 1$). The theory curves have no free parameters and the agreement between the data and the exact theory is excellent in both limits of coupling strength. When $\gamma_{avg} = 5.5$, T_{1D} is already quite close to its asymptotic TG limit. The insensitivity to further transverse squeezing can be seen in the flattening out of the data at high γ. In (b) the exact theory more closely resembles the mean field theory curve, and T_{1D} does not level off to the same degree as in (a). The difference in the horizontal width Δw_h^2 between the two different expansion times increases when U_0 goes below $20\,E_{rec}$ in (a). This is evidence that the atoms are tunneling between tubes when the lattice depth is sufficiently low. When this happens the system is no longer 1D, which is why the data deviates from the theoretical curve in this region. In (b) the increase in Δw_h^2 appears not to occur until $10\,E_{rec}$. However, the lattice parameters are identical in both cases, so the atoms, in theory, should be able to tunnel between tubes. The reason Δw_h^2 remains near zero in (b) below $20\,E_{rec}$ must be related to inter-tube mean field interactions (some self trapping mechanism) [26]. Nevertheless, the system is still not 1D in this region.

4.4 1D cloud size measurement

We also looked at the in-situ 1D atomic cloud root mean square (rms) full widths, w_{rms}, as a function of U_0. Here, we hope to directly observe the flattening out of the 1D cloud size with increased transverse confinement. We again use high intensity fluorescence imaging. The result is shown in Figure 4.3.

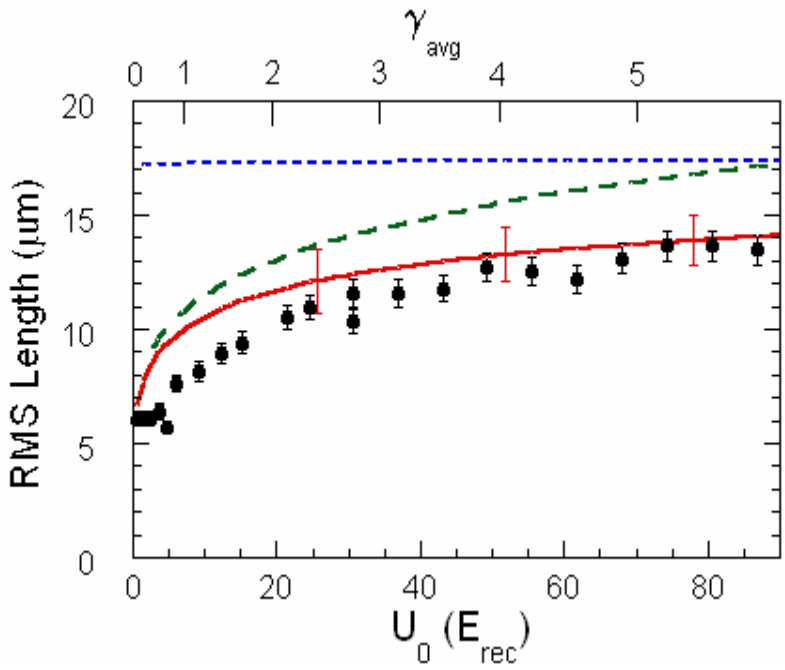

Figure 4.3: Plot of the rms full width of the 1D atom cloud versus the transverse confinement at P=12mW. The circles represent the measured values, with the instrumental resolution deconvolved. Error bars on the experimental points reflect residual trap excitations that arise when the lattice is turned on. The curves for TG theory (short-dashed line), mean field theory (long-dashed line), and exact 1D Bose gas theory (solid line) are shown [27]. Error bars on the theory curve reflect uncertainties in experimental parameters and are dominated by a 5% uncertainty in w_{ir}. With no free

parameters, the data conform to the exact theory [27] above $U_0 \sim 20E_{rec}$, where the system is purely 1D.

The density distribution in any individual tube is either an inverted parabola ($\gamma << 1$) or the square root of an inverted parabola ($\gamma >> 1$) [24]. To compare the experimental results to theory, we take the width of the Gaussian fit to the raw data, w_{ex}, and deconvolve from it the instrumental resolution of our imaging system, w_{ir}. We experimentally determine w_{ir} by looking at the in-situ distribution of a 3D BEC at increasingly higher YAG beam powers and determine it to be ~20 μm. The increased confinement makes the BEC size smaller and smaller. When we can no longer see any decrease in size, we've reached the instrumental resolution of our system. Assuming that both the atomic distribution and instrumental resolution are nearly Gaussians, which is a reasonable approximation for an inverted parabola, the width becomes $w_m = \sqrt{w_{ex}^2 - w_{ir}^2}$. The difference between w_m and the exact theoretical prediction w_{rms} is between 2 and 4%. Because this is smaller than our dominant systematic error, our knowledge of w_{ir}, no adjustments are made to account for this difference. Since these results, we have improved w_{ir} to ~14 μm by more carefully aligning the imaging lenses.

With no free parameters the measured widths agree with the exact 1D Bose gas theory (solid curve in figure 3) [24]. Mean field theory (long dashed curves of figure 3) predicts a larger size and a larger rate of increase with γ. By $\gamma_{avg} = 5.7$ (a larger value than in

figure 2 because there are 12% fewer atom in this scan), the size is still 20% below the asymptotic value (dotted line in figure 3), indicating that the cloud size approaches the asymptotic value much slower than the total energy.

Looking at figures 2 and 3 together, we see that figure 3 shows that the actual cloud length is smaller than that calculated from mean field (Thomas Fermi) theory, which means the 1D density is larger. But even with a larger 1D density, figure 2 shows that the total energy of the atoms is 2.5 times smaller than the mean field theory value. This can only mean that there is substantial reduction in wave function overlap, i.e. fermionization of the 1D gas.

4.5 Averaging the predicted quantities over the tubes

To do the averaging over the 1D tubes the following distribution function is used:

$$\frac{2}{\pi R^2}\left(1-\frac{r^2}{R^2}\right)2\pi r dr \text{, for } r < R. \tag{4.5.1}$$

This inverted parabola results from the 3D BEC being well in the Thomas-Fermi limit. To get the theoretical value for T_{1D} for the TG, and BEC regimes, we simply do a weighted average over the tubes as follows,

$$T_{1Davg} = \int T_{1D}^{tube}(r)\frac{2}{\pi R^2}\left(1-\frac{r^2}{R^2}\right)2\pi r dr. \tag{4.5.2}$$

The r dependence of T_{1D}^{tube} stems from having a different number of atoms, N_{tube}, as a function of r. The result changes by less than 5% if a single tube with γ_{avg} is considered. As stated in section 4.3.2, our knowledge of the exact atomic distribution among tubes is limited. To see the size of any possible error due to this, we repeat the calculations for γ_{avg} and T_{1Davg} with a flat-top atomic distribution and find that they also change by less than 5%.

For w_{rms}, we calculate, in the same way as described above, the cloud radius in the TG or BEC regime, R_{Tonks} and R_{TF} respectively. The w_{rms} can then be easily calculated from these values. For the TG and the TF (BEC) distributions the actual w_{rms} is larger than what it would be for a single tube with γ_{avg} by $c_{TG} = 5\%$ and $c_{TF} = 2.5\%$ respectively. Acquiring w_{rms} for the exact 1D Bose gas theory presents a minor complication, as different tubes have different distribution functions. Using Olshanii, et al.'s results for the exact rms width of the distribution in units of R_{TF}, we obtain w_{rms} for a single tube with γ_{avg} and then multiply by $\frac{c_{TF+}c_{TG}\gamma_{avg}}{1+\gamma_{avg}}$ to correct for the difference.

The following theoretical results are from Ref. [24]:

$$R_{TF} = \left(\frac{3N_{tube}\left(\frac{\hbar}{m\omega_z}\right)^2}{|a_{1D}|} \right)^{1/3} \tag{4.5.3}$$

$$R_{Tonks} = \sqrt{2N_{tube}\frac{\hbar}{m\omega_z}} \tag{4.5.4}$$

$$T_{1DTF} = \frac{2}{5k_B} mR_{TF}^2 \omega_z^2 \tag{4.5.5}$$

$$T_{1DTonks} = \frac{2}{8k_B} mR_{Tonks}^2 \omega_z^2 \tag{4.5.6}$$

The exact 1D Bose gas theory values were numerically tabulated for us by Olshani et. al. in units of R_{TF} or T_{1DTF} as function of γ.

4.6 Second order correlation function measurement

Another way to measure the degree of fermionization of the gas is to look at the 2nd order correlation function at zero particle separation, $g^{(2)}(0)$. This is proportional to the probability of observing two particles in the same place at the same time, and is defined as:

$$g^{(2)} = \left\langle \Psi(z')^{+2} \Psi(z')^2 \right\rangle / n_{1D}^2 , \tag{4.6.1}$$

where $\Psi(z')$ is the atom field operator and $n_{1D} = \left\langle \Psi(z')^{+} \times \Psi(z') \right\rangle$ is the 1D linear density [33]. The local [27-30] and non local [31, 32] pair correlations of atoms have

previously been measured in contexts other than 1D Bose gases. We use photoassociation to measure $g^{(2)}(0)$.

4.6.1 Definition of local pair correlation function

In the mean field or BEC regime, the 1D gas has $g^{(2)} \approx 1$, just as in a 3D BEC. In the TG limit, the wave function overlap approaches zero, and so $g^{(2)} \to 0$, mimicking noninteracting fermions in 1D. The measurement of $g^{(2)}$ is a direct measurement of the degree of wave function overlap, which is the essence of fermionization of the gas. In contrast, the total energy measurement is rather indirect.

4.6.2 Experimental Overview

For this measurement, after reaching BEC, we adiabatically change the YAG beam waist to 120 μm. After turning on the 2D, blue detuned by 3.2 THz, optical lattice in the same manner as described above, we have between 1000 and 8000 parallel 1D traps, depending on the YAG power, P_{cd}. The weighted average number of atoms per tube, N_{tube}, is between 40 and 240. To avoid tunneling between the tubes on the timescale of the observations, the final lattice depth is kept above 30 E_{rec}.

As described in section 3.3, $\gamma \approx \frac{2a_{3D}}{n_{1D}a_{\perp}^2}$, where $a_{3D} = 5.3nm$ is the 3D scattering length, and $a_{\perp} \geq 35nm$, is the transverse oscillator length. To scan γ in this experiment,

we take sets of data with different n_{1D}, which we control by using different $P_{cd}'s$ before the lattice turn on. For each set, we scan the lattice depth, which in turn changes $a_{\perp}$. As P_{cd} is varied from 36mW to 3.1W, the 3D Thomas-Fermi radius ranges from 20 μm to 8.2 μm, N_{tube} for the central tube ranges from 65 to 390, and the axial oscillation frequency, $\omega_z / 2\pi$, ranges from 15Hz to 150Hz. In this way we can scan γ from 0.37 to 11.

The maximum spontaneous emission rates, using equation (1.3.8), are 0.4 s^{-1} due to the lattice light and 0.28 s^{-1} due to the YAG light. We can decrease the lattice detuning to 1.6THz for the lowest density case because the heating that results from spontaneous emission is less severe when the 1D density is lower. The reason for this is that atoms that spontaneously emit a photon are left in a random magnetic sublevel, but only the F=1, $m_F = 1$ and F=2, $m_F = -1$ sublevels are levitated by the gradient field. Unlevitated atoms accelerate away from the crossed dipole trap center. They impart collisional kinetic energy to other atoms, and the number of collisions depends the density. To minimize this effect, we make sure to keep the YAG trap depth shallow enough so that these unlevitated atoms can escape.

4.6.3 The photoassociation scheme

We measure $g^{(2)}$ by photoassociation, using light resonant with the molecular state $\left|0^-_g(\sim S_{1/2} + P_{3/2}), \upsilon = 1, J = 2\right\rangle$, located ~26.7$cm^{-1}$ (~79THz red detuned) below the D2

line, where υ and J are the vibrational and rotational quantum numbers respectively [34] (see figure 4.4)

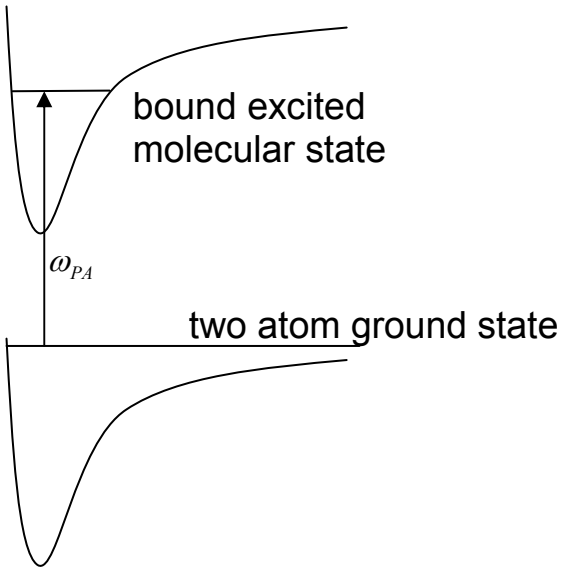

Figure 4.4: The photoassociation transition from the two atom ground state to an excited bound molecular state. The photoassociation laser, ω_{PA}, is detuned 79THz below the D2 transition.

Given the intensity of our PA beam, described in the next section, the stimulated transition rate between the two atom ground state and the bound molecular state, Γ_{stim}, is much less than the spontaneous decay rate of the molecule, $\Gamma_{spont}(\sim 2\pi \times 12MHz)$. This means that when a molecule is formed by photoassociation, it quickly decays spontaneously, with a very high likelihood, to a bound molecular ground state, which is not detected by fluorescence imaging. The photoassociation rate is therefore proportional to the measured loss of atoms.

The photoassociation rate, K_{3D}, can be calculated by two-body s-wave scattering theory [35]. For a pure 3D BEC,

$$K_{3D} = \frac{8\pi\hbar}{mk}\frac{\Gamma_{stim}}{\Gamma_{spont}}, \tag{4.6.2}$$

where $\hbar k$ is the relative momentum of the two particles. For the small $k's$ that prevail in ultracold atom experiments, Γ_{stim} is proportional to k, making K_{3D} velocity independent [35]. Photoassociation is most likely to occur at very short interparticle distances, between 1.6 and 1.9 nm [36]. This distance scale is much less than the typical extent of the atomic wave function, either axially in 1D (>~300 nm) or transversely (>35 nm). Therefore the photoassociation rate in 1D is proportional to the 3D photoassociation rate, but reduced by the loss of wave function overlap due to the 1D nature of the gas,

$$K_{1D} = K_{3D} g^{(2)}. \tag{4.6.3}$$

4.6.4 The photoassociation pulse

Figure 4.5 shows the experimental set up with both the YAG trap, the 2D optical lattice and the photoassociation, PA, beam.

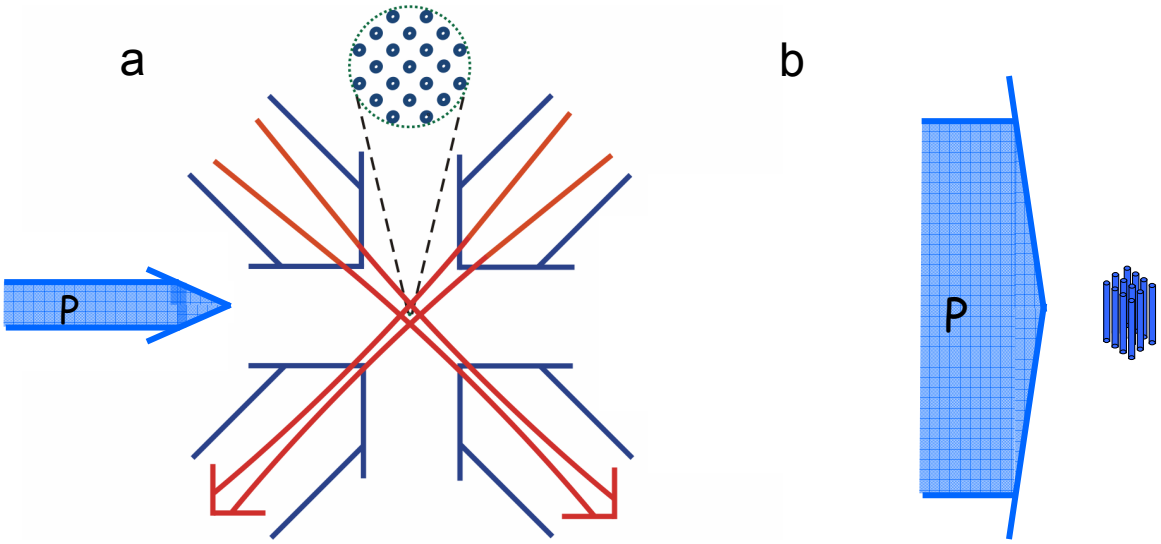

Figure 4.5: Experimental geometry. (a) Laser beam configuration, top view. Four blue detuned beams with 600 μm waists (fat, wide arrows) form the 2D optical lattice. This is superimposed on a the YAG trap (skinny red arrows) which are 120 μm in this experiment. The circular blow up shows the array of 1D Bose gases. The 280 μm waist photoassociation beam (PA), uniformly illuminates all of the 1D Bose gases. (b) Trapped atom distribution, side view. The atoms are confined radially in the vibrational ground state, with characteristic radii that range from 35 to 50 nm. The full axial lengths of the atom clouds range from 15 to 50 μm, much smaller than the photoassociation beam. The aspect ratios of the 1D Bose gases ranges from ~150 to 700.

The PA beam is 60mW, has a 280 μm waist, and is locked to a Fabry-Perot cavity that is, in turn, locked to the ^{87}Rb D2 resonance. The laser linewidth is less than 2MHz, smaller than the measured 13MHz linewidth of the photoassociation resonance. The beam is linearly polarized perpendicular to the 7 Gauss bias magnetic field and propagates in the horizontal plane of the optical lattice. It is much larger than the trapped atom region. It

is pulsed on for between 25 μs and 1 ms depending on the density, which is at most 1/65 of the axial oscillation period. This ensures that there is negligible axial redistribution of atoms, either due to loss of atoms, or the PA beam's dipole force. The atomic scattering rate due to the PA beam is 8 s^{-1} and can be neglected.

Immediately after the photassociation pulse, all traps are shut off suddenly, and a high intensity fluorescence image is taken [37] to determine the number of remaining atoms, N_{rPA}. We repeat the measurement with an off resonant PA pulse, 700MHz away from the molecular resonance, to determine the off resonant number, N_{orPA}, which causes less than 1% loss. The measured fractional loss due to photoassociation, f, is then $f = (N_{orPA} - N_{rPA}) / N_{orPA}$. Figure 4.6 shows f as a function of photoassociation time, T_{PA}, for both high density and low density trap conditions.

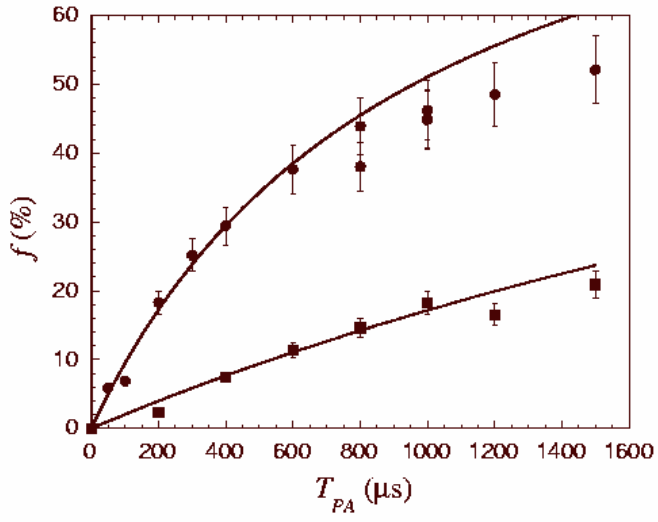

Figure 4.6: Atom loss by photoassociation. The fractional loss is plotted as a function of the photoassociation time. The circles (squares) correspond to $P_{cd} = 320mW (36mW)$. The solid curves are fits to a theory that assumes that

dN/dt is proportional to N^2 up to 600 μs (800 μs). The error bars reflect measured statistical fluctuations.

The solid curves are fits to the data at shorter times only to the solution of a two body loss equation, i.e. $\frac{dN}{dt} \propto N^2$. To simplify matters, we make sure to keep f less than 0.15 to ensure a constant loss rate (~linear region in figure 6). In this way we experimentally determine the fractional photoassociation loss rate per particle,

$$\Gamma_L = -\frac{1}{N}\frac{dN}{dt} = \frac{f}{T_{PA}}. \tag{4.6.4}$$

4.6.5 Photoassociation loss measurement results

As stated above, we collect data in sets characterized by the initial 3D BEC density, ranging from $3.2\times10^{13}\,cm^{-3}$ to $4.1\times10^{14}\,cm^{-3}$, by adjusting P_{cd}. At each initial density, we measure Γ_L both in the 3D BEC case, and for a range of optical lattice depths, which scans the transverse confinement in 1D. In figure 4.7, we plot the ratio of Γ_L normalized to the 3D BEC value of Γ_L as a function of the optical lattice depth in units of E_{rec}.

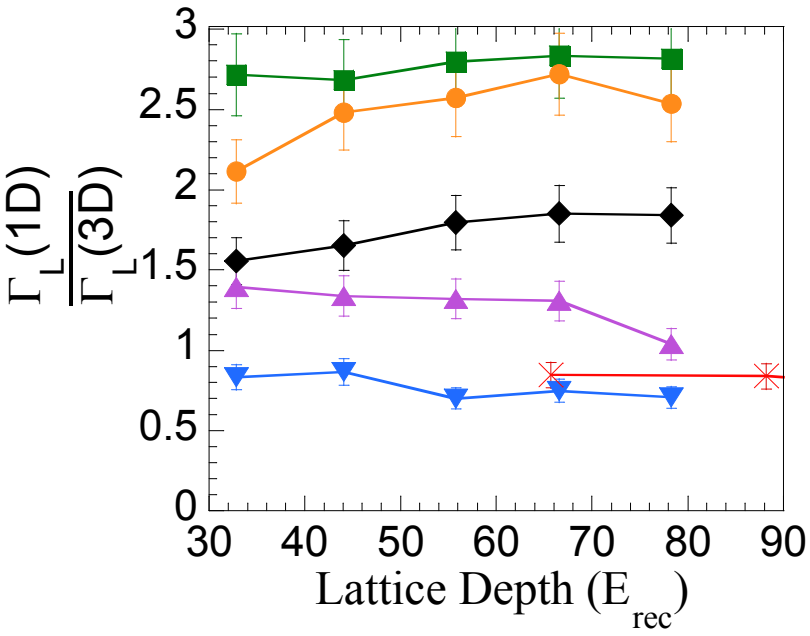

Figure 4.7: The effect of 1D confinement on photoassociative loss. The ratio of loss in 1D to loss in 3D is shown as a function of the 2D lattice depth. The error bars are standard deviations that characterize fluctuations in the total number of the atoms (which are 10%). The different curves correspond to different crossed dipole trap powers, and hence different n_{1D}. In order from higher to lower density, and from top to bottom on the graph: squares, $P_{cd} = 3.1$ W; circles, $P_{cd} = 1$ W; diamonds, $P_{cd} = 320$ mW; up triangles, $P_{cd} = 110$ mW; down triangles, $P_{cd} = 36$ mW. The crosses correspond to $P_{cd} = 36$ mW, but with a lattice detuning of 1.6 THz instead of 3.2 THz, and the larger E_{rec} points are omitted. The solid lines are to guide the eye.

Figure 4.7 demonstrates the decrease in $g^{(2)}$ with increasing γ in two ways. Within each curve, the axial confinement is fixed, as is N_{tube}. The individual curves show that Γ_L only weakly depends on the lattice depth, even though the atoms become more tightly confined as the lattice depth is increased, giving them a higher 3D density. A more

striking result is seen in comparing the curves from top to bottom. For the top curve, which corresponds to high initial density and low γ, turning on the lattice increases the loss by a factor of ~2.8. This extra loss can be understood as coming from the increased density that occurs when you confine the atoms in 1D tubes compared to the 3D YAG trap. However, this increased loss gets progressively smaller as the initial density is decreased (γ is increased). For the last two curves, which correspond to the lowest initial density, turning on the lattice actually decreases Γ_L. That is, despite the increased density associated with 1D confinement the loss rate is actually smaller than the 3D BEC case. This implies a stark reduction in $g^{(2)}$ associated with being in 1D.

4.6.6 Comparing our results to theory

To quantitatively compare our measurements to the exact 1D Bose gas theory, we need to extract an average $g^{(2)}$ from our loss measurements, and then plot them as a function of the universal parameter γ [33]. Each atom experiences a different local density, and hence a different γ, so we need to take an appropriate average γ for the ensemble. It turns out that $g^{(2)}$ varies roughly linearly with log (γ) over the range of γ in this experiment. We therefore define γ_{eff} for the ensemble of atoms such that log (γ_{eff}) is the weighted average over the tubes of log (γ). This allows us to compare theoretical values for $g^{(2)}(\gamma)$ to our ensemble measurement.

Specifically, we first compute $\gamma_{tubeavg}$ for each tube and then average over all tubes to get γ_{eff}. To get $\gamma_{tubeavg}$, we need the 1D density $n_{1D}(z)$, which depends on N_{tube} and the

trap details. This function can be calculated numerically using the results of Ref. [24] for the rescaled density $s = n / n_{TF}^0$. s(z) is defined by the equation

$$\frac{1}{2\eta} F\left(\frac{2}{\eta s(z)}\right) + \frac{z^2}{2} = \frac{b^2}{2}, \tag{4.6.5a}$$

where b is the distribution radius with the condition,

$$\int_{-b}^{b} s(z)dz = 4/3 \ , \tag{4.6.5b}$$

where $\eta \equiv n_{TF}^0 |a_{1D}| = \frac{2}{\gamma}$, and $F\left(\frac{2}{\eta s(z)}\right)$ is the dimensionless Gibbs energy which the authors of Ref. [24] numerically calculated for us. Solving equation (4.6.5a) for F and using the result for the Gibbs energy function we can solve for $s(z)$

$$s(z) = \frac{2}{\eta F^{-1}(\eta(b^2 - z^2))} \ . \tag{4.6.6}$$

For a given η and b we can numerically get a test $s(z)$. Then we adjust b, thus changing $s(z)$ until equation (4.6.5b) holds. This gives the actual $s(z)$ and hence the exact 1D density distribution.

Then, since $\gamma_{exact}(z) = \frac{2}{n_{1D}(z)|a_{1D}|} = \frac{2}{n_{TF}^0 s(z)|a_{1D}|}$,

$$\gamma_{tubeavg} = \frac{\int_0^b \frac{2s(z)}{n_{TF}^0 s(z)|a_{1D}|}dz}{\int_0^b s(z)dz} = \frac{3b}{n_{TF}^0|a_{1D}|} \ . \qquad (4.6.7)$$

We then do a weighted average over all tubes as described above for $\log(\gamma_{tubeavg})$ and get $\log(\gamma_{eff})$.

Note: To be consistent with the reasoning for using the average of $\log(\gamma)$, equation 4.6.7 should calculate the average of $\log(\gamma)$. In the TG and BEC (mean field) limits, i.e. using $n_{TG}(z)$ or $n_{TF}(z)$ instead of $s(z)$ in 4.6.7, the value $10^{\langle \log\gamma \rangle}$ is less than $\langle\gamma\rangle$ by 4.7% and 11.5% respectively. Therefore, the γ_{eff} axis and the blue theory curve in Fig. 4.8 below should be shifted to the right by about 8%.

Once we know γ_{eff} for each data point, we can calculate experimental values for $g^{(2)}(\gamma_{eff})$ without reference to the 1D theory. As for any two body loss process, the governing equation for Γ_L within a tube is

$$\Gamma_L = \frac{2K_{3D}}{N_{tube}} \int n_{3D}(r)^2 g^{(2)}(z) dV \ , \qquad (4.6.8)$$

where we have used the earlier equation $K_{1D} = K_{3D} g^{(2)}$. n_{3D} is within each tube and depends on n_{1D} and the 2D harmonic oscillator ground state wave function.

$$n_{3D}(\rho, z) = \frac{n_{1D}(z)}{\pi a_r^2} \exp(-\frac{\rho^2}{a_r^2}), \text{ where } \rho \text{ is the radial coordinate.} \qquad (4.6.9)$$

Replacing $g^{(2)}(z)$ by $g^{(2)}(\gamma_{eff})$ and pulling it outside the integral, we get

$$g^{(2)}(\gamma_{eff}) = \frac{\Gamma_L}{2K_{3D}\langle n_{3D} \rangle}. \qquad (4.6.10)$$

We calculate $\langle n_{3D} \rangle$ by averaging $n_{3D}(\rho, z)$ within each tube and then over all tubes in much the same way as we did for γ_{eff}. We assume that atoms are distributed among tubes with the original 3D BEC Thomas Fermi distribution of an inverted parabola. The actual distribution can change as a result of tunneling during the lattice turn on. The imaging resolution prevents an exact knowledge of the distribution. To address the uncertainty, we repeat our calculations with a flat top distribution among tubes (i.e. all tubes have the same N_{tube} and hence the same γ. In doing so, γ_{eff} and n_{3D} each change by less than 5%.

The result is presented in figure 4.8.

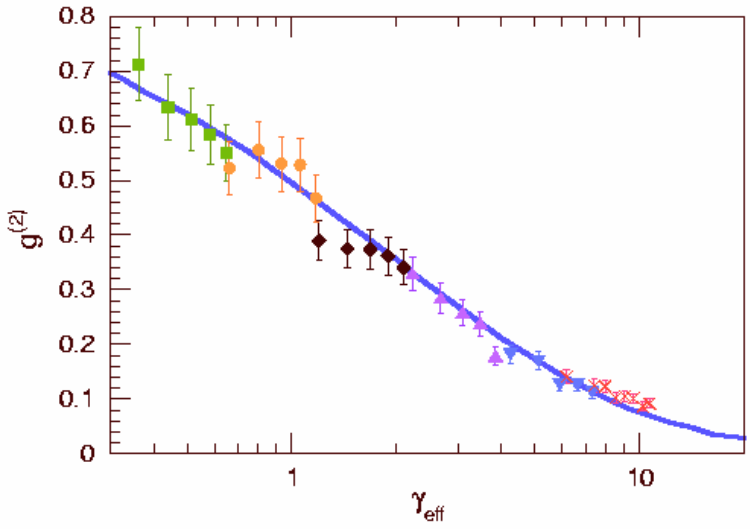

Figure 4.8: The local pair correlation function versus the coupling strength. The solid blue line is the 1D Bose gas theory [33]. The points and associated error bars are generated from the same data used in Figure 4.7. Here, $g^{(2)}$ is calculated for each point and the points are arranged according to the coupling parameter γ_{eff}. The data labels correspond to those in Figure 4.7. A scale factor proportional to K_{3D} has been determined by a weighted least squares fit of the data to the theory. This value of K_{3D} accords with our direct measurement of K_{3D} using 3D BEC's.

The solid curve is the result of the zero temperature 1D Bose gas theory for $g^{(2)}(\gamma)$ [33]. We plot the data from Figure 4.7 here in Figure 4.8 with corresponding labels using the above equations. K_{3D} is left as a free parameter and acts as a scaling factor. A weighted least squares fit to the theory determines a value of $K_{3D} = 4.3 \times 10^{-10} cm^3 / s$. Over our range of $\gamma_{eff} = 0.37$ to 11, $g^{(2)}(\gamma_{eff})$ varies by an order of magnitude and the agreement between the experiment and theory is excellent. In the mean field weak coupling limit $g^{(2)}$ approaches one, like a 3D BEC. In the strong coupling TG regime, $g^{(2)}$ approaches zero, showing the fermionization of the bosons.

We can measure K_{3D} in a more direct way using the Γ_L results from the 3D BEC's and equation (4.6.10) with $g^{(2)}$ set equal to 1. The average of these results is $K_{3D} = 4.7 \times 10^{-10} cm^3 / s$, with a statistical standard deviation of $\sigma_{Kst} = 0.3 \times 10^{-10} cm^3 / s$. The systematic uncertainty in this measurement is $0.6 \times 10^{-10} cm^3 / s$, primarily due to the uncertainty of $\pm 5 \mu m$ in the YAG trap beam waist, which affects n_{3D} in equation (6).

We can compare the direct measurement of K_{3D} to the value determined from Figure 4.8 in order to test the 1D Bose gas theory without any free parameters. Because the systematic uncertainty in the direct measurement of K_{3D} is highly correlated with the systematic uncertainty in $\langle n_{3D} \rangle$ for the 1D Bose gas, the systematic uncertainty in the scale for $g^{(2)}(\gamma_{eff})$ turns out to be less than 1% $(0.1 \times \sigma_{Kst} / K_{3D})$. Thus, the two separate determinations of K_{3D} agree to within 9%, or $1.3 \times \sigma_{Kst}$, and we have tested the 1D Bose gas theory to within this uncertainty.

4.7 1D momentum distribution of a TG gas

Further evidence of the gas being in the TG regime can be seen from the momentum distribution when the atoms are still in the trap. To measure this one cannot simply let the gas expand in the 1D tubes, since the momentum distribution changes during the expansion. In the mean field, BEC regime, there is mean field energy that is converted into kinetic energy during the expansion, thus changing the momentum distribution of the atoms. In the TG regime, although locally the strongly interacting bosons act like fermions, their momentum distribution is not fermionic. [38, 39]. When the TG gas expands in 1D, its momentum distribution evolves into to that of a trapped Fermi Gas [40-42]. The momentum distribution is actually quite different for a trapped TG gas than for a trapped Fermi gas as can be seen in Figure 4.9 [38].

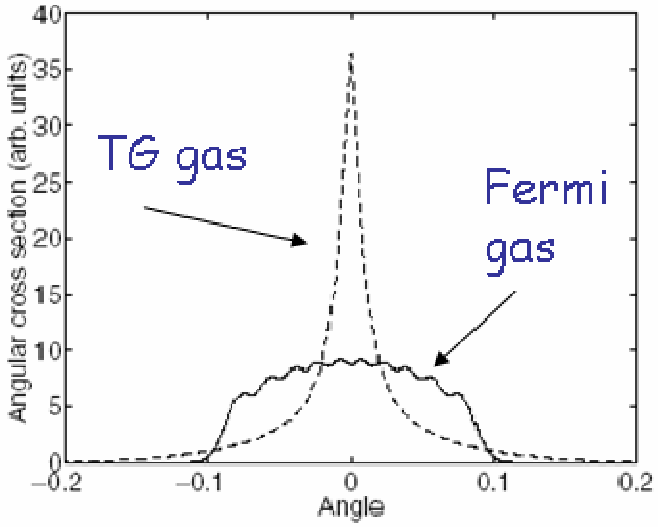

M.D. Girardeau, E.M. Wright, *PRL* **87**, 050403 (2001)

Figure 4.9: 1D momentum distribution for a TG gas and Fermi gas. The Fermi gas has the expected near flat top distribution. The TG gas is sharply peaked at p=0, with long tails at higher p.

The TG momentum distribution is characterized by a sharp peak at p=0 and long smooth tails at larger p. In order to access the trapped TG distribution, we must first shut off the interactions before expanding. To do this we turn off the 2D optical lattice adiabatically with respect to the transverse oscillations. The time constant for this is very fast, ($40\mu s$), compared to the turn on time constant of $\sim 40ms$ since we're only concerned with the very rapid transverse oscillation is this case. After this shut off, we expand in free space with only the levitation field for a few ms. The horizontal expansion is rapid due to residual transverse lattice kinetic energy. However, the vertical expansion is much slower and represents the momentum distribution the atoms had while in the trap plus undoubtedly some 3D mean field energy present after the lattice turn off. This energy is released early on in the expansion, however it does make this an imperfect measurement of the momentum distribution. Figure 4.10 shows one such distribution taken at $\gamma_{avg} \approx 3.5$.

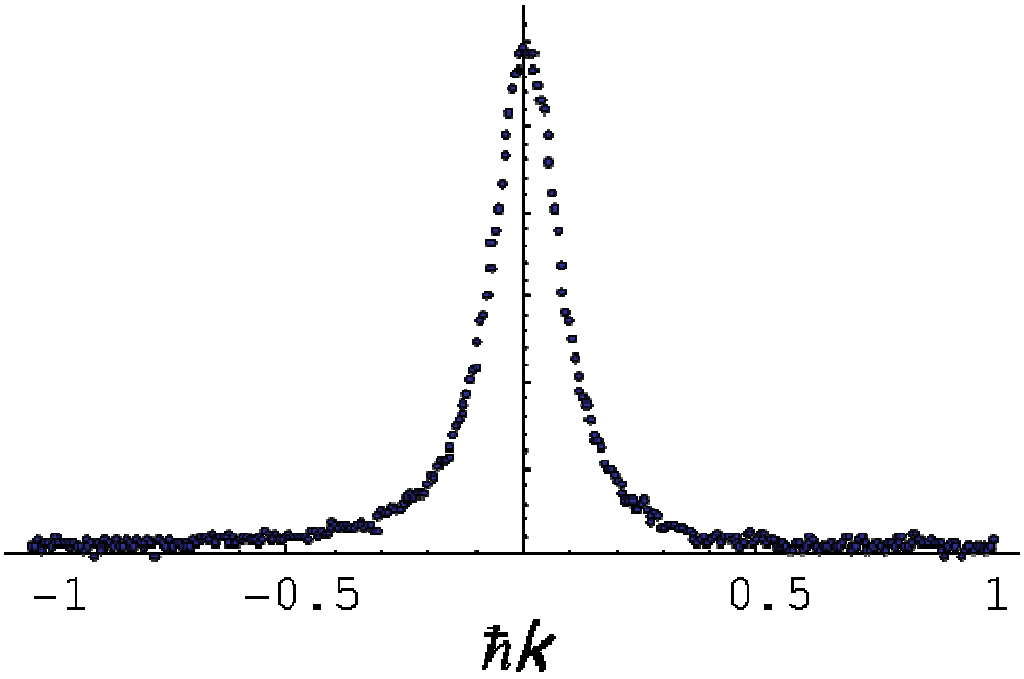

Figure 4.10: Momentum distribution of TG gas at $\gamma_{avg} = 3.5$. The qualitative characteristics of the TG momentum distribution are present. Namely, the p=0 peak and the long, gradual tails at higher p values.

One possible way to perfectly turn off the interactions would be to use a Feshbach resonance to set the scattering length to $a = 0$, thus making the mean field energy vanish.

The two detailed experiments described above show the behavior of a 1D Bose gas across an order of magnitude in coupling strength. The photoassociaton experiment dove fairly deep into the TG regime up to $\gamma = 11$. All data agree very well with 1D Bose gas theory across both regimes.

Chapter 5 : Non-equilibrium 1D Bose Gas, A Quantum Newton's Cradle

Another aspect of 1D gases that we want to look at is the nature of thermalization. In statistical mechanics, a closed system with many degrees of freedom (like a 3D thermal gas for example) randomly samples all equal energy points in phase space. When such a gas is initialized out of equilibrium, this ergodic sampling process leads to equilibration or thermalization. After a typically short characteristic time, the system reaches the largest entropy state with that energy, because that is the state with the highest multiplicity. Some complex systems have been proposed that are expected not to thermalize because their dynamics are integrable [43, 44], meaning every particles' phase space trajectory can be exactly calculated given the initial conditions. The 1D Bose gas with point like interactions is well known to be an integrable system, and thus is expected not to thermalize. However, experimental factors such as harmonic trapping in the 1D direction and non-perfect point like interactions may compromise the integrability of the system. In this experiment, we study non-equilibrium 1D Bose gases and find that they do not noticeably equilibrate even after thousands of collisions.

5.1 The Newton's Cradle analogy

To see qualitatively why 1D gases might not thermalize, consider the elastic collision of two isolated, identical mass classical particles in one dimension. Energy and

momentum can only be conserved if they simply exchange momenta. Clearly this process cannot alter the momentum distribution of an ensemble of such particles. This describes the well known behavior of a Newton's Cradle (Figure 5.1).

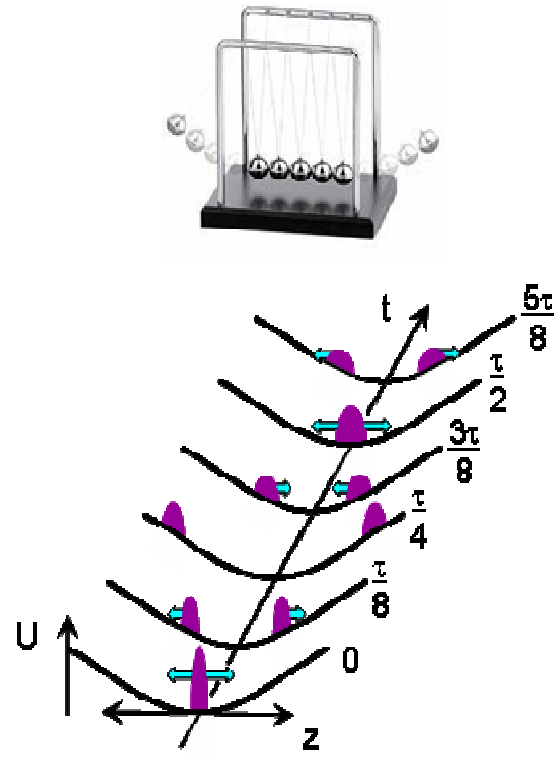

Figure 5.1: Top: Diagram of a classical Newton's cradle. Bottom: Sketches at various times of two out of equilibrium clouds of atoms in a 1D harmonic trap, U(z). At time t=0, the atoms are put into a momentum superposition with $2\hbar k$ to the right and left. The two parts of the wave function oscillate out of phase with each other with a period, τ. Each atom collides with the opposite momentum group twice every full cycle, for instance, at t=0 and $\tau/2$. Anharmonicity causes each group to gradually expand, until ultimately the atoms have fully dephased. Even after dephasing, each atom still collides with half the other atoms twice each cycle.

Even when several balls are simultaneously in contact, particles in an idealized Newton's Cradle simply exchange specific momentum values, though the explanation is more subtle [45]. In quantum mechanics, the situation is slightly different in that rather than just reflecting off of one another, the particles can also transmit through one another. However, when the particles are identical and the system is integrable, the final states for reflection and transmission are indistinguishable.

5.2 Overview of experiment

5.2.1 Caveats of Newton's Cradle analogy

In general, correlations and overlap among 1D Bose gas wave functions complicate the picture of independent particles colliding as in a Newton's cradle. There are circumstances in which 1D momentum distributions are known to change in time as discussed at the end of Chapter 4, albeit these involve a change in the momentum distribution only after trapping conditions have changed. The quantum Newton's cradle view of particles colliding with each other and either reflecting or transmitting can only be applied when the kinetic energy of the collision greatly exceeds the energy per atom at zero temperature at the prevailing density [24]. This effectively means the colliding atoms are well separated spatially before the collision. The collisions that we study satisfy this condition. We study non-equilibrium 1D Bose gases extending from the TG regime, where only pair-wise collisions can occur, to the intermediate coupling regime, where there can be three or more body collisions [46, 33, 22]. In both regimes, atoms

that are set oscillating and colliding in a trap do not appreciably thermalize during our experiment.

5.2.2 Experimental procedure

We again start with a pure 3D BEC in the $F = 1, m_F = 1$ ground state. We turn on the 2D optical lattice, which is again 3.2 THz blue detuned from the D2 line and $\sim 70 E_{rec}$ to avoid tunneling. In this experiment we take data at three different $\gamma's$, achieved by varying the YAG power and beam waist to change the initial 3D density, which ultimately changes $N_{tubeavg}$. After creating the non-equilibrium distributions, (see below) we allow the atoms to oscillate in the trap for a given amount of time, t before making a measurement. The axial oscillation period, τ, of the array of tubes is the same for each of the 1000 to 8000 tubes to within 6%.

To study the 1D Bose gases, we suddenly turn off the YAG trap and allow the atoms to expand in one dimension for 27 ms before taking an absorption image from the transverse direction. When we integrate the image transverse to the tubes, we get a 1D spatial distribution that corresponds to the momentum distribution after expansion, $f(p_{ex})$. Although the individual 1D gases have Thomas-Fermi or Tonks-Girardeau $f(p_{ex})$ profiles, we measure Gaussian $f(p_{ex})$ distributions. Numerical calculation of the distribution obtained when the $f(p_{ex})$ for many 1D Bose gases with different $N_{tubes}'s$ are summed after long expansion times also gives nearly Gaussian distributions.

5.2.3 Creating the non-equilibrium distributions, the double Z pulse

To create non-equilibrium momentum distributions, we pulse on a 3.2THz detuned 1D optical lattice in the axial direction (along the tubes), which acts as a phase grating for the atoms. Two pulses, with intensity 11 W cm^{-2} and pulse widths of 23 μs separated in time by 33 μs, can deplete the zero momentum state and transfer atoms to $\pm 2\hbar k$ peaks, [47, 48] where k is the wavevector of the 1D lattice light. After waiting for time, t, we measure $f(p_{ex})$. Figure 5.2 shows the zero holding time, $t = 0$, $f(p_{ex})$. We optimized the above parameters for the double Z pulse by using a 3D BEC and minimizing the p=0 component (<5%). When the pulse is applied with the 2D lattice on, the p=0 component is not so perfectly depleted, presumably because of the stronger interactions between atoms during the pulse sequence. The remant near p=0 is larger for denser 1D gases, where the energy scale of interactions is larger.

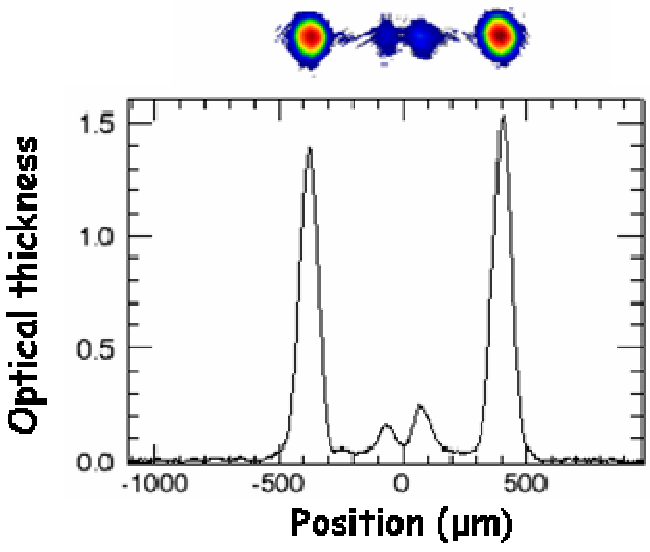

Figure 5.2: $f(p_{ex})$ for t=0 holding time after the double Z pulse. Lattice power is nearly 700mW and the initial γ_{avg} is ~ 4.0. The distribution is highly non-thermal. The absorption image is shown on top. Although the 1D axial direction is vertical in the experiment, images are shown oriented horizontally to correspond to figure 5.1.

5.3 Experimental results

5.3.1 The first oscillation cycle and dephasing

Figure 5.3 shows a time series of images spanning the 1st full oscillation period in the trap. The weighted average of the initial peak γ in each tube is $\gamma_{avg} = 1.0$ (see sect. 4.3.2).

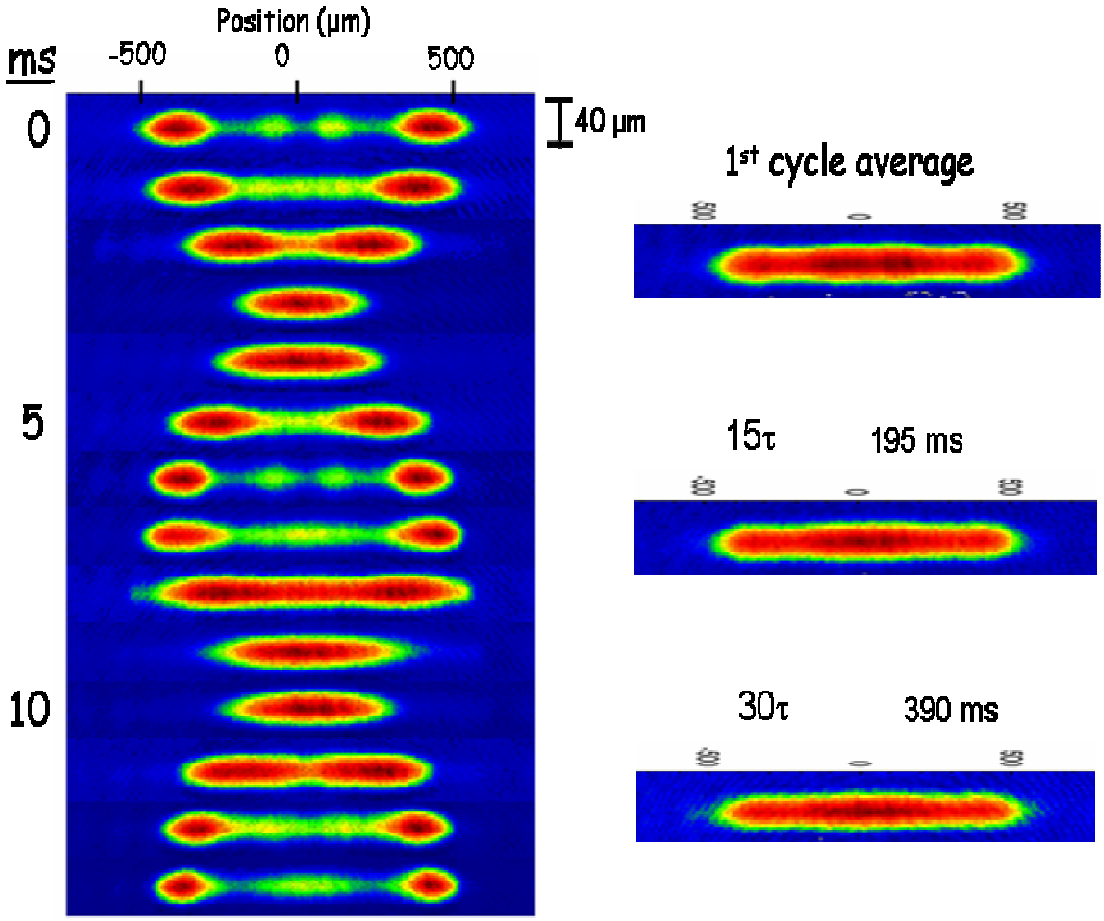

Figure 5.3: Absorption images in the first oscillation cycle for initial average peak coupling strength $\gamma_{avg} = 1$. Atoms are always confined to one dimension, in this case in 3,000 parallel tubes, with a weighted average of 110 atoms per tube. After grating pulses put each atom in a superposition of $\pm 2\hbar k$ momentum, they are allowed to evolve for a variable time, t, in the anharmonic 1D trap, before being released and photographed 27ms later. The false color in each image is rescaled to show detail. These pictures are used to determine $f(p_{ex})$. The first image shows that some atoms remain near $p_{ex} = 0$ at $t = 0$. How many remain there depends on n_{1D}, implying that these remnant atoms do not result from an imperfect pulse sequence, but rather from interactions during

expansion. The relative narrowness of the peaks in the last image compared to the first is indicative of the reduction in spatial density that results from dephasing (Figure 5.1). The transverse spatial width of each of the 14 image frames is $70\,\mu m$. The side figures, from top to bottom, are the 1st period averaged, $t = 15\tau$, and $t = 30\tau$.

The two momentum groups collide with each other in the center of the trap twice each full cycle, at $t = 0$, and at $t = \tau/2$, as shown in Figure 5.1. The total collision energy per particle is $\frac{8(\hbar k)^2}{2m} = 0.45\hbar\omega_r$. Since this is less than one-quarter of the energy needed for transverse vibrational excitation [49], we presume that no transverse excitatations occur, so the gas remains 1D. Any transverse excitations would have to involve the simultaneous collision of many atoms.

The first and last images in figure 2 are slightly different due to the fact that the oscillating atoms dephase in the trap. Dephasing results from the Gaussian YAG beam trap anharmonicity, which gives an 8% spread in τ within a single colliding cloud across its full width at half maximum. Therefore each colliding cloud tends to smear out as it oscillates. When it smears out, the density in each cloud is decreased, and so is the mean field energy. The result after expansion is that the individual clouds are slightly narrower because of their smaller mean field energy in the trap. This can be seen in figure 5.3. Eventually the increased size of each cloud is the major factor in the size after expansion.

5.3.2 Longer holding times

Eventually, the dephasing completely smears out the colliding clouds so that the distribution $f(p_{ex})$ is constant on the time scale of the oscillation. This occurs within about 10τ to 15τ, depending on the trap parameters. Figure 5.4 shows $f(p_{ex})$ for three different $\gamma's$ at different holding times, t.

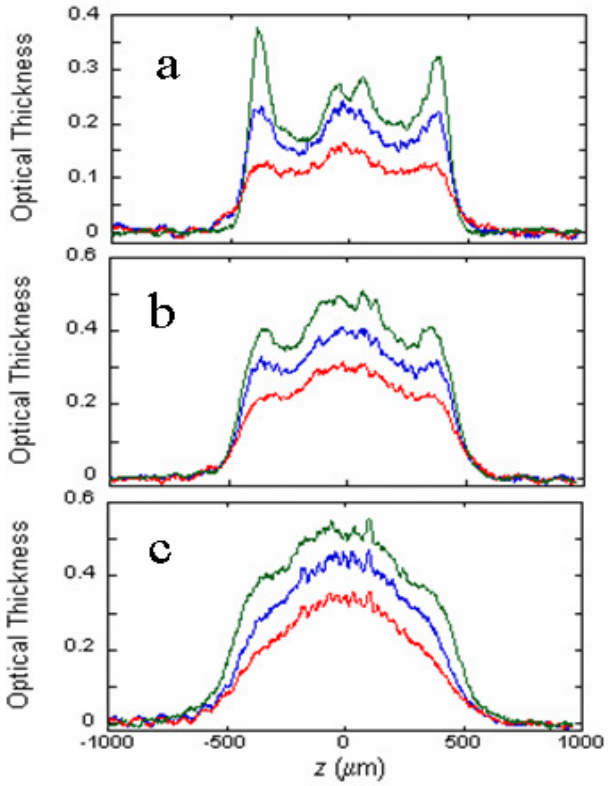

Figure 5.4: $f(p_{ex})$ for three different values of γ_{avg}. The curves are obtained by transversely integrating absorption images like those of Figure 5.3. The spatial position, z, is approximately proportional to the expanded momentum, p_{ex}. The vertical scale is arbitrary, but consistent among the curves. **a,** $\gamma_{avg} = 4$**; b,** $\gamma_{avg} = 1$**;** and **c,** $\gamma_{avg} = 0.62$. The highest (green) curve in each set is the average of $f(p_{ex})$ from the first cycle, that is, from the images like those in Figure 5.3. The lower curves in each set are $f(p_{ex})$ taken at single times, t, after the atoms have dephased: **a,** $\tau = 34ms$**,** $t = 15\tau$ (blue) and 30τ (red); **b,** $\tau = 13ms$**,** $t = 15\tau$ (blue) and 40τ (red); and **c,** $\tau = 13ms$**,** $t = 15\tau$ (blue) and 40τ (red). The changes in the distribution with time are attributable to known loss and heating.

The top curve in each (a-c) is the time average of $f(p_{ex})$ over the 1st oscillation cycle, while the bottom two curves in (a-c) are after dephasing has completed. Differences in the shape among these curves reflect the differences in the initial energy per particle, which increases with n_{1D}, and hence γ_{avg}^{-1}. When the initial density is higher (c), the mean field energy is greater and hence after expansion, $f(p_{ex})$ is smoother. The central observation of this experiment is the comparison of $f(p_{ex})$, only after dephasing, at different holding times to see if there is any equilibration. This avoids the complication of the evolution of the in-trap momentum distribution into $f(p_{ex})$, which may slightly depend on the initial spatial distribution.

All of the curves in Figure 5.4 are non-Gaussian. To the extent that the distribution is non-Gaussian, it has not equilibrated. We know this by checking equilibrium 1D Bose gases with nearly the same root mean square momentum. We do this by starting with a non T=0 equilibrium 3D BEC, and adiabatically turning on the 2D lattice. In this case the resultant $f(p_{ex})$ are nearly perfectly Gaussian.

5.4 Heating and loss

Heating and loss during the holding time in the trap affect the evolution of the distribution. We must take this into account when comparing distributions at earlier times to ones at later times in order to make reliable statements about thermalization. Fortunately, because the non-equilibrium distributions are large compared to the effect of the heating on the distribution, the final results are quite insensitive to how we account for the heating, as we shall see. First, Figure 5.5 shows the atom loss as a function of holding time.

5.4.1 Loss mechanisms

The loss can be attributed to 3 mechanisms. There is some initial loss (20% or less depending on γ_{avg}) that occurs in the first couple of hundred milliseconds, attributable to three body inelastic collisions. There is also 15% per second loss to background gas collisions which can be independently measured with a 3D BEC in only the YAG trap.

Finally, there is spontaneous emission from lattice light, which can leave atoms in untrapped magnetic sublevels and causes a 30% per second loss.

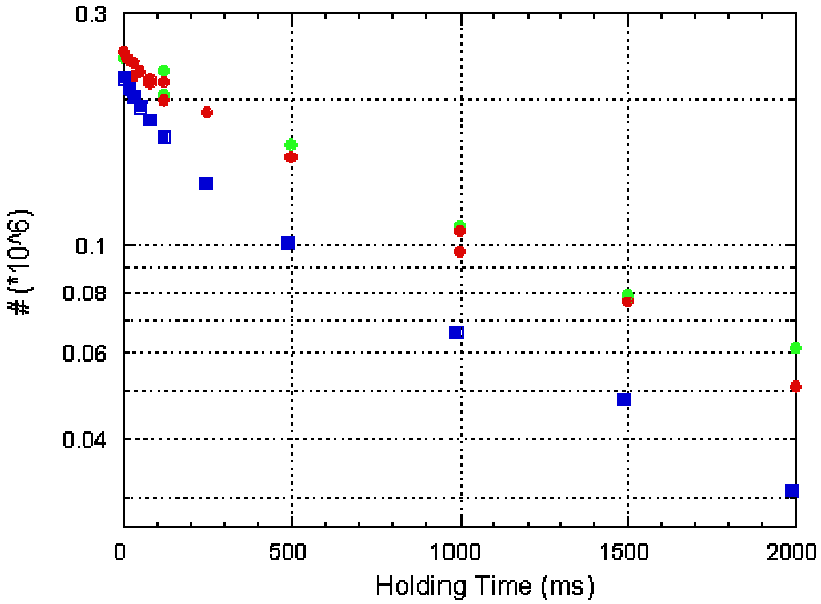

Figure 5.5: Atom number loss as a function of holding time in the 2D lattice for blue ($\gamma_{avg} = 0.62$), red ($\gamma_{avg} = 1$), and green ($\gamma_{avg} = 4$). The kink in the curve at around a few hundred milliseconds is the transition from 3-body loss to the other two mechanisms discussed above.

5.4.2 Heating analysis

To analyze the heating we repeat the same kind of measurements as in Figure 5.4 but without the 1D lattice grating pulses. Thus, we study the affect of heating and loss in the trap on a 1D T=0 distribution. Figure 5.6 shows curves for points corresponding to the same conditions as in Figure 5.4 but without the grating pulses. There are some qualitative differences in the time evolution due to the heating at different γ_{avg} values.

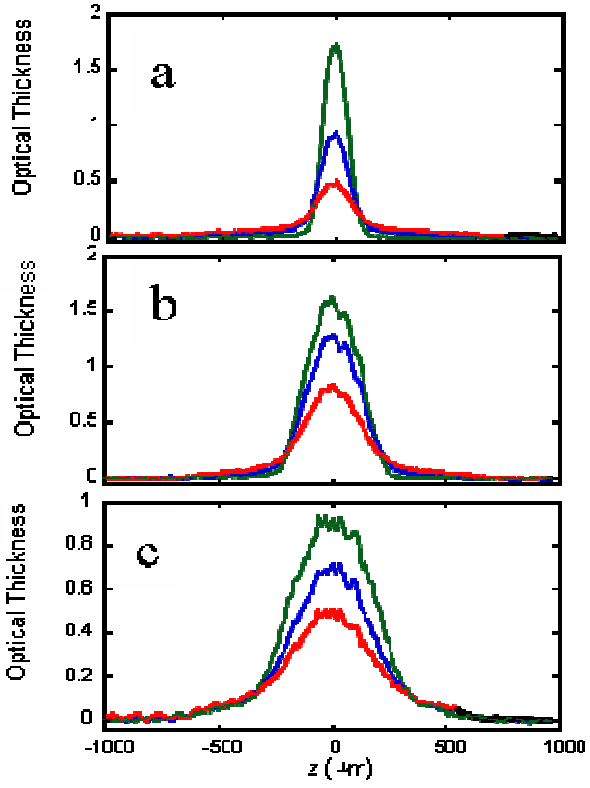

Figure 5.6: Time evolution of $f(p_{ex})$ for various γ_{avg}'s with no applied grating pulses. a) $\gamma_{avg} = 4$ and $t = 0$ (green), 15τ (blue), and 30τ (red). b) $\gamma_{avg} = 1$ and $t = 0$ (green),

15τ (blue), and 40τ (red). c) $\gamma_{avg} = 0.62$ and $t = 0$ (green), 15τ (blue), and 40τ (red). This figure should be compared to Figure 5.4 to gain a sense for the relative importance of heating to the projected curves.

In figure 5.6a, for $\gamma_{avg} = 4.0$, the $t = 0$ (green) curve fits well to a single Gaussian. The other, later time curves fit well to the sum of two Gaussians, with the width of the wider, bottom Gaussian constrained to have an r.m.s. width of 305 μm. Least squared fits of $f(p_{ex})$ to such a double Gaussian model at various vales of t, show that the relative population of the wider, bottom Gaussian simply grows linearly in time, reaching a value of 49% at $t = 30\tau$. The unconstrained r.m.s. width of the narrower, upper Gaussian grows linearly during this time, from 55 to 70 μm.

It might be tempting for the casual observer to attribute the wider, bottom Gaussian to a thermal component and the central, upper Gaussian to a BEC component, akin to how a 3D BEC behaves. However as stated above, we know this is not how a T>0 1D Bose gas behaves in equilibrium. The fact that the distributions become more non-Gaussian with a growing bottom component can be explained by heated atoms joining a new distribution which does then not thermalize with the original distribution. The wider Gaussian does not grow in width with time, which would be expected for a conventional heating process, but rather only in amplitude.

5.4.3 Heating mechanisms

Heating primarily results from spontaneous emission due to the 2D lattice light by two distinct mechanisms. As stated above, spontaneous emission usually leaves atoms in magnetic sublevels that are not levitated against gravity, so they fall up or down out of the trap. Such atoms can collide with $F = 1, m_F = 1$ atoms on their way out and impart their recently gained kinetic energy to them. Trapped atoms gaining energy in this way join the new momentum distribution which has the empirically determined r.m.s. width of 305 μm. We confirm this explanation experimentally by increasing the depth of the YAG trap so that atoms that aren't levitated remain trapped. These atoms then have multiple chances to impart their always increasing kinetic energy to $F = 1, m_F = 1$ atoms. The heating becomes worse with each additional sublevel that can be trapped as is supported by figure 5.7.

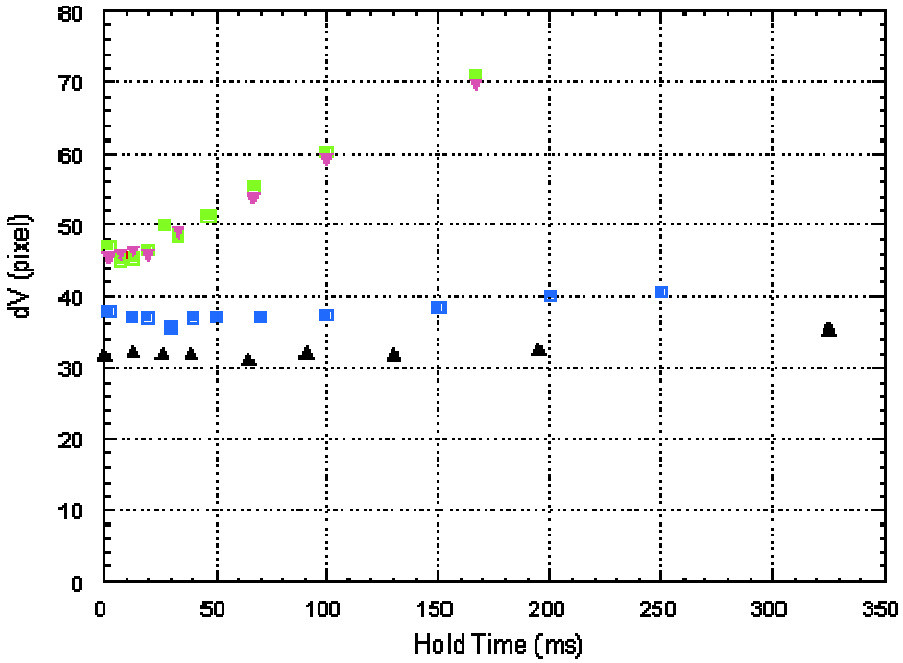

Figure 5.7: The vertical (axial) width is plotted in pixels (1 pixel=2.7 μm) as a function of holding time in the 2D lattice. All curves are taken at 700mW lattice power. The black curve has a YAG power of 37mW (2.41 μK) during lattice ramp up. The blue curve has a power of 110mW (7.22 μK) during ramp up and then is reduce to 37mW. The green, and pink curves all have powers of 110mW throughout, however the lattice turn on time constants are different, pink (10ms), and green (3.5ms). The larger heating rate at 110mW is attributed to the trapping of an additional magnetic sublevel that cannot be trapped at 37mW.

Due to this drastic effect we make sure that the depth of the YAG trap is always shallow enough so as not to trap unlevitated sublevels.

The second heating mechanism is the projection of photon recoil in 1D for those atoms that undergo spontaneous emission and return to the $F = 1, m_F = 1$ state. These atoms become part of a new distribution that is widened by the convolution of the initial cloud length and the non Gaussian $\sim 35 \mu m$ wide distribution of possible recoil projections. The r.m.s. width of this new distribution is $65 \mu m$, not much wider than the initial distribution. As atoms transfer to it, the net effect is the observed broadening of the narrower Gaussian.

The descriptions and explanations for Figure 5.6b are identical to those for Figure 5.6a, except that the initial Gaussian is wide enough that the effect of the second heating mechanism is not observable in this time, so the width of the central, upper Gaussian stays fixed. The r.m.s. width of the wider, bottom Gaussian is $350 \mu m$, and its population reaches 36% by 40τ.

For Figure 5.6c, the $t = 0$ curve for $\gamma_{avg} = 0.62$ is not a single Gaussian. This is probably caused by non-adiabatic heating during the preparation of that state, specifically, when the YAG trap depth is lowered after the 2D lattice turn on. This complicates the impact of the heating but the dominant mechanism (the width of the wider, bottom Gaussian) is comparable to the other two cases (305 μm). It has no effect on the measurement since we are only concerned with how an initial non Gaussian distribution created from the grating pulses evolves in time.

5.4.4 Correction for heating and loss and the results

To account for loss and heating in the time evolution of the distribution, we project how already dephased distribution (i.e. $t = 15\tau$) would evolve in the absence of any thermalization. We take $f(p_{ex})$ at $t = 15\tau$, rescale it to account for loss during the holding time, t_{hold}, and convolve it with Gaussian widths to capture the effect of the heating. Figure 5.8 shows the results for $\gamma_{avg}(\gamma_d) = 4(18),1(3.2),0.62(1.4)$, where γ_d takes into account the reduced density of the 1D gas after the grating pulses and dephasing.

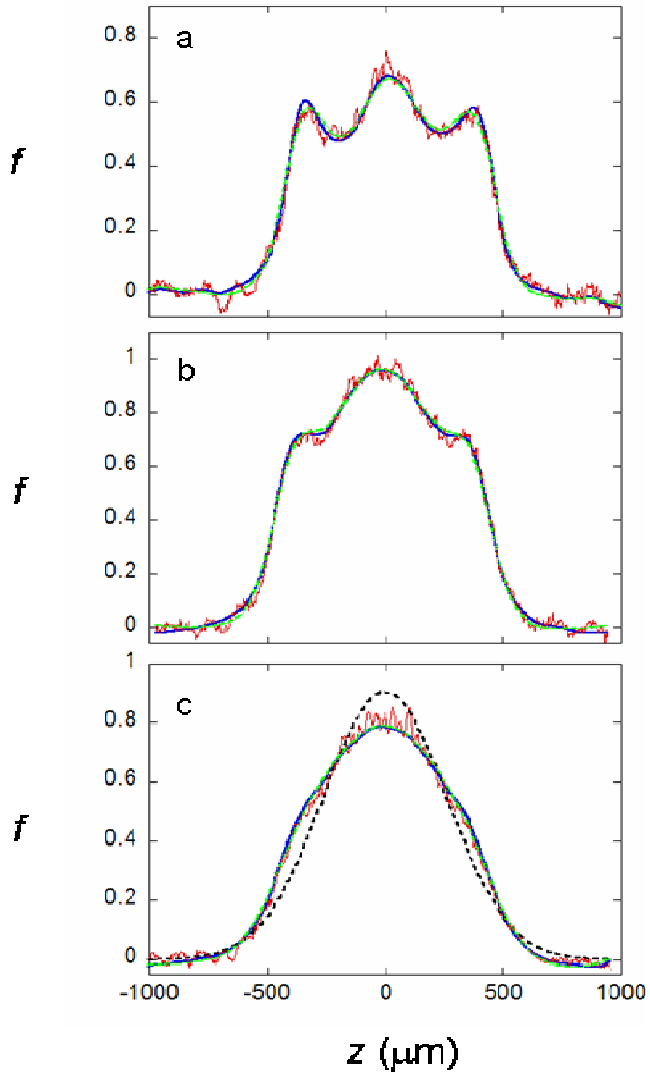

Figure 5.8: Projected versus actual $f(p_{ex})$ for various γ_d's. The blue and green curves are $f(p_{ex})$ for $t = 15\tau$, rescaled to account for loss and convolved with the known heating during the holding time. The blue curve's heating model is more sophisticated than that of the green curve, but the results are insensitive to the details. The red curves are the actual distributions at $t + t_{hold}$. a), $\gamma_d = 18$ and $t_{hold} = 15\tau$. b) $\gamma_d = 3.2$ and $t_{hold} = 25\tau$. c) $\gamma_d = 1.4$ and $t_{hold} = 25\tau$. The dashed line in c) is a Gaussian with the

same number of atoms and r.m.s. width as the actual distribution. To the extent that the actual distribution conforms to the projected distribution rather than to a Gaussian, the atoms have not thermalized.

We project the heating in two distinct ways which are shown as the blue and green curves in Figure 5.8. We assume that the atoms will be heated out of the initial distribution by the dominant mechanism at the rate measured from the population of the wider, bottom Gaussian in Figure 5.6. They thus will transfer into a new distribution that is a convolution of the curve at 15τ with the independently measured 305 μm r.m.s. width Gaussian. i.e.

$$f(p_{ex})_{conv}(z) = \int f(p_{ex})_{15\tau}(z_0) * \sqrt{\frac{2}{\pi}} \frac{1}{610} \exp\left(\frac{-2(z-z_0)^2}{610^2} \right) dz_0 \qquad (5.4.1)$$

The Gaussian $1/e^2$ full width is twice the Gaussian r.m.s. full width, hence the value of 610 in equation (5.4.1). The small effect of recoil heating is captured by similarly convolving the distribution of the rest of the atoms with the Gaussian associated with the broadening of the narrow, upper Gaussian in Figure 5.6. The final projection $f(p_{ex})_{proj2comp}$ is then the sum of these two Gaussian convolutions. These projected curves are the blue ones in Figure 5.8.

The second approach to account for the heating is much simpler. We do a least squares single Gaussian fit to the curves in Figure 5.6. This does not yield very good fits, but allows an approximate overall heating rate to be assigned to each γ_{avg} condition. The heating rates so determined are 73 nK/s, 135nK/s, and 230nK/s for $\gamma_{avg} = 4,1, and\, 0.62$ respectively. A single Gaussian reflecting this heating rate is then convolved with $f(p_{ex})_{15\tau}$. This procedure generates the green curves in Figure 5.8. We then do a reduced Chi squared (χ^2) analysis between the projected curves, $f(p_{ex})_{proj}$, and the actual distributions at later times (30τ for Figure 5.8a and 40τ for Figure 5.8b,c). The results for the χ^2 values using the blue curves (2 Gaussian convolution approach) are 1.2, 1.4, and 2.55 for Figure 5.8a, 5.8b, and 5.8c respectively, while for the green curves (single Gaussian approach), they are 1.4, 1.7, and 2.4.

Yet a third way to account for the heating is vary the single Gaussian heating rate to provide the best fit between the projected and actual curves. This does not use the independently measured heating data. The heating rates so determined are 15-50% smaller than those used in the single Gaussian method described above. Still, this approach yields comparable reduced χ^2 values of 1.2, 1.4, and 2.2 for Figure 5.8a, 5.8b, and 5.8c respectively. The projected curves also are nearly indistinguishable.

A possible imperfection in this analysis is that the heating is not necessarily the same after the grating pulse as compared to the no grating pulse data. We reason there are two dominant effects. First, the spatial extent of the 1D clouds is larger after the grating pulses, which increases the amount of time that an unlevitated atoms can accelerate, and therefore increases the energy available for transfer. After dephasing, this extra available

collision energy is proportional to $(2\eta k)^2$, where $\eta = 2/\gamma$ is the 1D gas parameter and k is the atom momentum. Second, the relative momentum of the atoms in the trap significantly increases after the grating pulses. The probability of reflective collisions is roughly proportional to $(2\eta k)^{-2}$ [23]. Combining these effects, it seems reasonable to expect comparable, but not necessarily identical, heating rates before and after the grating pulses.

For Figure 5.8b,c the YAG beam waist is 50 μm and the power is 37mW, giving a τ of 13ms, but $N_{tubeavg}$ is different by having different 3D densities during the lattice turn on, when atoms are trapped into tubes. After the lattice turn on the power is adjusted to the same value. In Figure 5.8a, the YAG waist is 120 μm and the power is 26mW, giving a τ of 34ms. Figure 5.8 shows excellent agreement between the actual distributions (red curves) and the projected distributions (blue or green curves) for all three coupling strengths. In each case, the difference between the projected and actual curves is far smaller than the difference between either of them and a thermal Gaussian distribution. To highlight the non Gaussian shape of Figure 5.8c, we have superimposed a Gaussian with the same atom number and r.m.s. width as the data. The slight discrepancies that exist between the projected and actual curves may result from the ~25% loss of atoms during t_{hold}, which reduces the interaction energy contribution to $f(p_{ex})$.

5.5 Determination of the lower bound on thermalization

By assuming that any deviation between the projected and actual distributions is a step along the way to thermalization, we conservatively determine a lower bound on the

thermalization time constant, τ_{th}. As described above we calculate χ^2_{ap}, the reduced χ^2 obtained from comparing the projected $f(p_{ex})$ to the actual $f(p_{ex})$. We also calculate χ^2_{ag}, the reduced χ^2 obtained from comparing the actual $f(p_{ex})$ to a Gaussian with the same atom number and r.m.s. width. We take χ^2_{ag} as a measure of the extent to which the gas in not thermalized. If we then assume that the entire χ^2_{ap} represents the small first step in an exponential approach of the actual distribution to a Gaussian, then

$$\chi^2_{ag} = (\chi^2_{ag} + \chi^2_{ap})e^{-t_{hold}/\tau_{th}} \tag{5.5.1}$$

implying,

$$\tau_{th} = t_{hold}(\chi^2_{ag} + \chi^2_{ap})/\chi^2_{ap} \ . \tag{5.5.2}$$

In doing so we find that the lower bounds on τ_{th} are 390τ, $1{,}910\tau$, and 200τ for $\gamma_{avg} = 4$, 1, and 0.62 respectively. This implies that as far as we can tell, there is no discernable thermalization of the 1D Bose gas.

To obtain the variance that normalizes the χ^2's we use the tails of the distribution where the atom signal is zero. Fluctuations in the absorption probe beam dominate the noise here. The χ^2 is calculated as:

$$\chi^2 = \sum_z (f(p_{ex})_{proj}(z) - f(p_{ex})_{actual})^2(z) / \sum_{tails} f(p_{ex})_{actual}(z)^2 \tag{5.5.3}$$

There is some fine spatial structure near the center of the atom cloud that is attributable to ~1% spatial variations of the lattice beam intensity. They result in sub nK micro traps that the atoms see in 1D as they expand. The spatial frequencies of these noise sources

are higher than the spatial frequencies of $f(p_{ex})_{proj}$, so they do not contribute to χ^2_{ap}. However they do reduce χ^2_{ag} in a physically meaningless way via normalization using the noise in the tails. Therefore we apply a point spread filter function that averages over a set number of points around some z_0 to smooth out the actual distributions. We increase the number of points used until the χ^2_{ap} is about 10% larger for the filtered distribution than for the unfiltered distribution. This is approximately when filtering starts to change the shape of the actual distribution on a scale relevant to the projected distribution. The projected distributions are already smoothed by the convolving processes and so are unaffected by this additional filtering.

The results, similar to Figure 5.8, of the projected distributions compared to the filtered actual distributions, are shown in Figure 5.9.

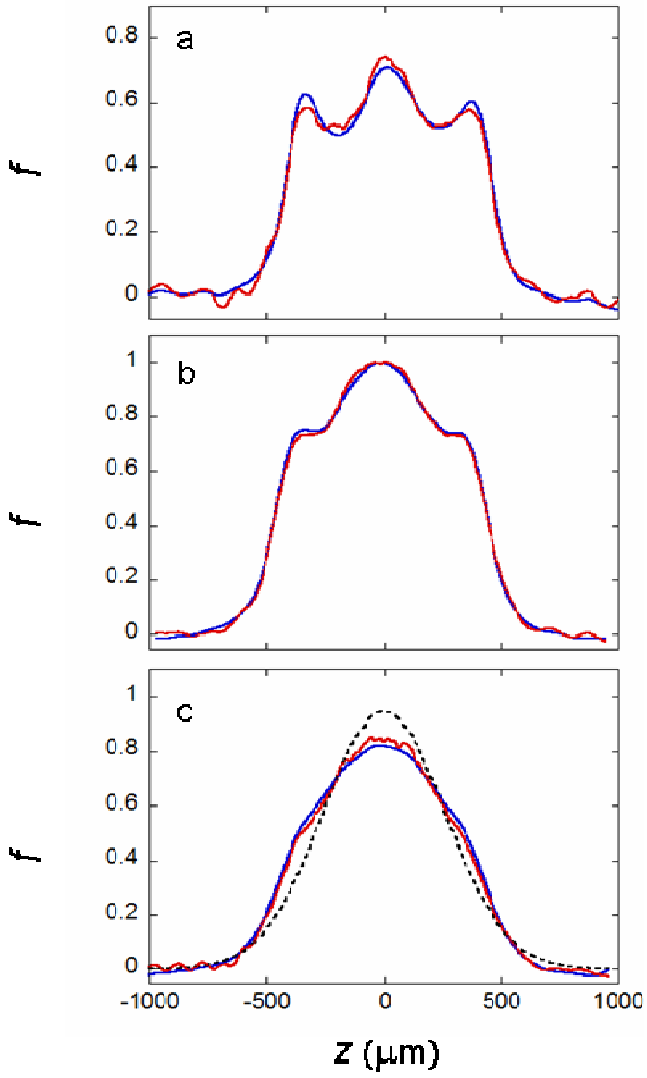

Figure 5.9: Projected versus actual $f(p_{ex})$ for various coupling, with filtered data. This figure is the same as Figure 5.8, but with a point spread function applied to the data as described above. The blue lines are the $f(p_{ex})$ for $t_0 = 15\tau$, rescaled to account for loss and convolved with the known heating. The red lines are the actual distributions at $t_0 + t_{hold}$. a), $\gamma_d = 18$ and $t_{hold} = 15\tau$. b) $\gamma_d = 3.2$ and $t_{hold} = 25\tau$. c) $\gamma_d = 1.4$ and $t_{hold} = 25\tau$. The dotted line in c) is a Gaussian with the same number and r.m.s. width as

the actual distribution. To the extent that the actual distribution conforms to the projected distribution rather than to a Gaussian, the atoms have not thermalized.

For $\gamma_{avg} = 4, 1.0, and\, 0.62$ respectively, the number of points used in the filter function is 11, 17, and 8; χ^2_{ap} is 1.29, 1.47, and 2.8; χ^2_{ag} is 32, 111, and 19.5; and the lower limit on τ_{th} is 390τ, $1{,}910\tau$, and 200τ. The results for τ_{th} are the ones stated above as well. Performing the same analysis with the single component Gaussian heating projections, the number of points used is 17, 19, and 9; χ^2_{ap} is 1.5, 1.8, and 2.7; χ^2_{ag} is 47, 125, and 21; and τ_{th} is 470τ, $1{,}690\tau$, and 220τ. The difference in τ_{th} using three different data analyses are in all cases less than 25% which we consider to be the approximate systematic uncertainty in τ_{th}.

Although collisions have no dynamical effect, we would like to roughly keep track of how many have occurred. Each atom passes $N_{tubeavg}/2$ atoms each half cycle. The probability of reflection, R, in a pairwise collision of 1D bosons with center of mass momentum $2\hbar k$ was calculated in Ref [23]. In the limit where $(2ka_{1D})^2 >> 1$, $R = (2ka_{1D})^{-2}$. For our confinement parameters, $R = 1/22$. Therefore, in the first full cycle, the number of $2\hbar k$ collisions in $N_{tubeavg}$, with $r = N_{tubeavg}/22$ reflections. After dephasing, each atom has as many collisions, but at center of mass momenta that range from $2\hbar k$ to near 0. As the relative velocity decreases, R increases quadratically (until it saturates), but the ability of a collision to redistribute momentum is reduced roughly

quadratically. Therefore, we use the r derived above to keep track of reflections even after the atoms have dephased. For the conditions in figure 7a, 7b, and 7c the average number of collisions that have occurred per atom during t_{hold} are 600, 2,750, and 6,250, respectively, and the average number of reflections are 27, 125, and 285. Using the results from Fig. 5.9, we can set lower limits on the number of reflections required for thermalization of 710, 9,600, and 2,300. These limits are obviously much larger than the 2.7 collisions that characterizes thermalization in a 3D gas [50].

5.6 Thermalization in 3D

To experimentally confirm the existence of collisions in this system, despite their lack of consequence in 1D, we apply the grating pulse to a 3D BEC without the 2D optical lattice, and thus create non-equilibrium distributions in 3D. Two BEC's with center of mass velocity $2\hbar k$ collide every half cycle. At the quarter cycle times, the two BEC's are well separated spatially, implying that collisions occur well above the Landau critical velocity. This allows particles to scatter out of the BEC [51]. The absorption image of the BEC at different times after the grating pulse is shown in Figure 5.10.

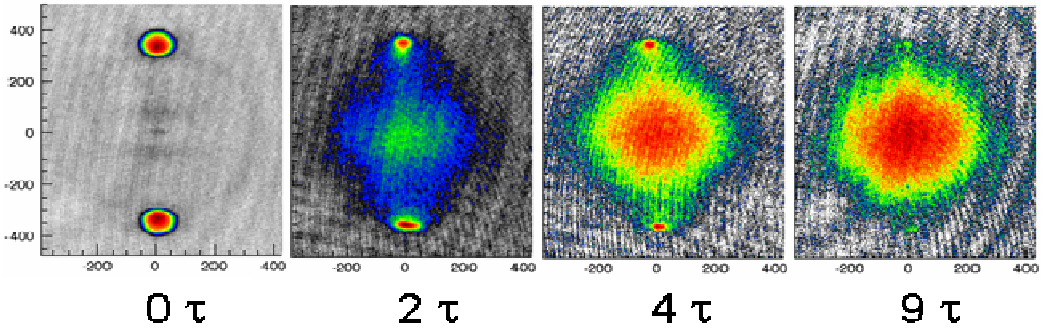

Figure 5.10: Absorption images of the thermalization of a non-equilibrium 3D BEC. The exact same grating pulse sequence was given to a BEC in the YAG trap with no 2D lattice. The system quickly evolves from a highly non-equilibrium state to a thermal, Gaussian, distribution.

We observe thermalization in a two step process. Atoms first scatter into a spherical shell in velocity, which corresponds to the outgoing s-wave. They then scatter into a broad range of final states when these s-wave shell atoms recollide with each other and BEC atoms. Even though the 3D densities are nearly an order of magnitude lower than in 1D tubes, thermalization occurs on a $<2\tau$ timescale, reinforcing the observed lack of thermalization in 1D.

Conclusion:

We have studied 1D Bose gases across an order of magnitude in coupling strength, demonstrating excellent agreement with 1D Bose gas theory in all regimes. 1D energy, atomic cloud size and the 2nd order pair correlation function, g_2, were all measured and fit to theory with excellent agreement. We have demonstrated entrance into the Tonks-Girardeau regime, creating a 1D system with a maximum γ of 11.

Starting from an all optical BEC, we turn on a blue detuned 2D optical lattice to form an array of 1D tubes. Since the axial confinement is derived from a separate optical dipole trap (YAG) and the because the 2D lattice is blue detuned, we can scan the depth of the 1D tubes, and thus the coupling strength, with only minimal change to the axial confinement (<2%). This allows for a meaningful scan of the 1D gas parameter, γ, as we measure the 1D energy and size.

We have seen nearly an order of magnitude decrease in g_2 as we scan γ from 0.3 to nearly 11 using a photoassociation scheme. Highly excited molecules are formed during a photoassociation laser pulse resulting in a measured number loss which can be converted into a measure of g_2.

The nature of non-equilibrium 1D Bose gas distributions was also studied. As expected from the known integrability of perfect 1D systems, we see no evidence of thermalization of the 1D Bose gas, even after thousands of reflections.

Future Directions:

The success of the fits to theory for the 1D energy, size, and g_2 data is both exciting and encouraging. 1D Bose gases are one of the few complex systems which is exactly solvable. Hence, there is extensive theory to rely on when doing these experiments. Other systems, such as 2D Bose gases or even fractional dimension Bose gases, achieved by lowering the 1D tube depths and allowing tunneling, are not exactly solvable. The fact that our data fits to the 1D Bose gas theory with no free parameters gives us confidence that data taken in higher dimension systems can be trusted. Studying such systems with experiments may help the development of theory.

As we have shown, if you allow there to be tunneling from tube to tube in the 1D array, thermalization of the Bose gas proceeds. The exact mechanism of this thermalization, for instance how the energy is shared between the dimensions, is not well understood however. Nor is it known if the mechanism for thermalization depends on the coupling strength. Implementing a Feshbach resonance to increase the scattering length would allow us to scan γ over a much larger range and help us to answer such questions.

Other avenues to pursue include searching for the Kosterliss-Thaullis transition for 2D Bose gases. It may be possible to directly observe this transition from looking at the atom cloud itself. Also, non-linear self trapping in 2D could be studied. This has been experimentally observed in 1D, using a 1D optical lattice [52], and theoretically studied in 2D [53].

For both of the above, we would need to implement a new imaging system that allowed us access to view the atoms from the top. Then we could view the 2D pancakes

from face on, or the 1D tubes axially, to better view the atom distribution from the relevant direction.

Appendix A: Timing Program: Supertime v2.0.vi

Overview

The timing program supertimev2.0 is a labview 6.1 vi used to control the timing of the experiment. Once set in motion it controls every aspect of the experiment via voltages that are output at designated timing edges. Further, it will automatically repeat the timing sequence as many times as desired to allow for averaging of the signal to reduce signal to noise.

The main program is located in C:\mastertime\Timing in the timing computer. The front panel user interface is divided into five sections which will be described in detail below. It allows the user to easily create new timing sequences or alter existing sequences with minimal effort. There are typically 36 voltage channels and hundreds of timing edges where one or more voltage channels are updated. Therefore it is very important that any change in the timing sequence (for instance when scanning a variable) can be done with relative ease and in minimal time.

Hardware

The supertimev2.0 vi's data is outputted via four national instruments boards. Three of them are identical PCI – 6713 analog output boards. These boards are 12 bit digital to analog converters with an output voltage range of -12V to +12V giving an output voltage resolution of about 5mV. They each have eight analog output channels. There is also a

homemade analog to digital converter box which takes 2 of these analog output channels and converts them into 14 digital output channels. The fourth national instrument board is a PCI – 6534 high speed digital I/O timing card. This card generates the timing signal which in turn updates the analog output boards. This process will be described in detail later.

Front Panel – Control Functions

Most of the front panel interface software had already been written. Consequently some of the sub-sections were simply not used at all in running the actual experiment. They may be of some use at some point but in so far as they were never used in the set of experiments in this thesis, I will not describe them here. The data sets to output sub-section of Control Functions is one such sub-section.

The clock resolution sub-section sets the resolution of the timing card. The minimum resolution of the timing card is 1 s and this value is always used for the target resolution. The toggle switch just below the target resolution input is disconnected in the back panel and is therefore useless. It's one time purpose was to switch between two modes of writing to the timing card. One such mode proved superior and is now always used.

The generate signal button acts in conjunction with the output values at this edge only button in the Edges section to start or stop output of the timing signal and output voltages. Once this button is pressed it will turn blinking red and read stop generation. This means the voltages are updated continuously. There are two modes of operation:

static mode and running mode. If the output values at this edge only box is checked, this is static mode. In this case, the output voltage channels can only be updated by hand in the channels section of the front panel. If the output values at this edge only box is unchecked, this is running mode. In this case, the timing sequence will be generated by the data in the Edges section and the output channels will be updated automatically according to the timing signal.

Front Panel – Data Functions

This section allows the user to save new timing programs or restore previously saved programs. After the generation of a program, i.e. all of the edges information and channels information are input, you can save the program by clicking the save button in this section. All of the programs for this set of experiments are saved in C:\mastertime\Timing\Modules.

Front Panel – Edges

This is one of the two main heart and soul sections on the front panel, the other being channels. The edges section describes what the timing sequence is and allows the user to alter it. Each edge corresponds to an update in voltages during the timing sequence. The edit/view edge box allows the user to select an edge, and it gives the absolute time in ms with respect to the start of the timing sequence of this edge. When in static mode as described above, the edge that is selected will correspond to the voltages that are output

on the channels. When in static mode for extended periods of time the selected edge should be Start Cycle Ref to ensure that voltages for Lower and Upper Mot and Yag E.O. are zero. Large voltages on the lower or upper Mot channels corresponds to large currents in the Mot coils which if left on can melt the coils themselves. Large voltage on the Yag E.O. channel corresponds to a large voltage across the QX 1320 crystal which if left on can permanently damage the crystal.

To edit an edge, therefore, first make sure the output values at this edge only box is checked and the generate signal button is off (i.e. not blinking), in that order. The user may then change the selected edge and the voltages will not be updated. The parameters for the selected edge are given in the edge box. These parameters are first defined when the edge is created, which will be described later. To edit the parameters, the Lock Edge Info box must be unchecked. Edge name is self explanatory. The Defined with Respect to box indicates the edge with which the selected edge is defined and gives the absolute time of this edge. The Relative Time box is the time in ms when the selected edge occurs with respect to the defined with respect to edge. The absolute time box gives the absolute time in ms of the selected edge. Therefore, the absolute time box value is always the sum of the relative time box value and the absolute time in the defined with respect to box. For time type, in this set of experiments, relative was always used. Selecting the variable time type allows the timing of an edge to be a variable defined in the variables section on the front panel. In practical use, it was always easier to simply vary relative time by hand rather than selecting a different variable and so it was never used. Channel Values at this Edge simply displays what the voltage is defined to be for every channel at the selected edge.

The Add/Remove Edge button allows the user to add new edges or delete existing edges. When pressed a sub-program appears called Add New Edge.vi. To add a single edge, make sure the adiabatic change circle is unmarked. The sub sections of edge name, defined with respect to, relative time, and time type are identical to those described above. Simply enter the parameters, then click the confirm adiabatic choice box. This box must light up before you can add the edge or even exit the sub program. Then you can click the add it button and then exit. Keep in mind you may have to click the confirm adiabatic choice box again before exiting if the green light is not lit.

To remove an edge, simply click the confirm adiabatic choice box, then go to the remove edge sub section. Click on the edge or edges that you want removed so that they are blue and then click remove and exit.

The rest of the input in this sub program is for adding an adiabatic change. In this set of experiments the only adiabatic changes that were made were for the X, Y, and Z lattice beam powers and the Yag beam power, and the Yag beam waist but that is not done in this program. The adiabatic change is normally done so that the change in power of the laser beam changes the oscillation frequency of that trap slowly with respect to the oscillation frequency itself. The array at the top labeled power start stop is where the user defines the start and stop powers of the adiabatic change. The labels Z, X, and Y correspond to the Z, X , and Y lattice A.O.M's which occur in that order on the optical table. For the lattice beams, first set the toggle to lattice AO's, select the number of beams to undergo the adiabatic change, 1, 2 or 3 and activate the corresponding A.O. boxes by clicking the circles. The labels 1^{st}, 2^{nd}, 3^{rd} correspond to Z, X, and Y respectively and you must enter the channel name in the respective boxes. Then set the

toggle to exp fn, which means the function used for the adiabatic change is an exponential. This function is used for practicality rather than absolute correctness. Enter for the total power into first A.O. the laser power of the lattice Ti Sapphire. This is usually around 2.35 Watts. Then enter the time constant for the exponential change and the time interval which is the time step between edges in the adiabatic change. If Psymmentric has the same value as the largest of start or stop power, then the entire adiabatic curve is produced. If it has some intermediate value then you only get that portion of the curve which goes from Psymmetric to the smaller of start or stop power. When everything is entered click the adiabatic change circle so that it is marked. The value for the voltages of the 1st 2nd and 3rd channels (A.O.'s) are then displayed in the array in the middle of the screen in the 1st 2nd and 3rd rows respectively. Each column in the array is one edge. Then click add it and exit and the adiabatic edges will appear in the edge data and the voltages will appear in the channel data on the main front panel.

For the Yag E.O. the procedure is identical except for the following. Set the toggle to Yag E.O. and only use the Z A.O. row in the power array since there is only one beam. Enter 1 for number of adiabatic beams and select the 1st A.O. box and enter Yag E.O. Enter the total Yag power of 10 Watts in the total power into 1st A.O. box. Set the toggle to t sq fn. This means the adiabatic function goes as $1/(1+t/to)^2$ where to is the time constant. This is the exact functional form resulting from the equation $\frac{dw}{wdt} << w$, where w is the oscillation frequency of the trap.

Front Panel – Variables

This sub section is used for defining variables used in conjunction with edge type when defining an edge. As stated above this aspect of the program was not used and therefore will not be discussed further.

Front Panel – Channels

This is the other main heart and soul sub section of the timing program. It allows the user to add or remove output voltage channels and to define the voltages of existing channels at each edge. The edit/view channel box allows the user to select a channel for viewing or editing. Once a channel is selected, its information is displayed in the Channel Array box. To alter any channel information the Lock Channel Info box must be unchecked. Channel name is self explanatory. The card # and channel # boxes define which analog output board (1, 2, or 3) and which channel number of that board the selected channel is defined to. These are first determined when the channel is added. The large white scroll box lists all of the edges in the sequence and the voltage value at each edge for the selected channel. The user can select an edge by clicking on the edge name (the edge will become encased in blue). The voltage value at this edge then appears in the Value at This Edge box just to the right of the scroll box. To change the voltage value simply enter a new value in this box and the channel information will be automatically updated. The Edge State box allows the user to more easily define all of the edge values for a given channel. If the edge state is none, changing the channel value at a given edge will only change it at that edge. However, many times a given channel

will want to remain at a constant voltage for many edges. The user can define an edge as begin in which case a small plus sign appears to the left of the edge in the scroll box. Then changing the channel value at this edge has the effect of making all of the channel values at every other edge below the same value until an edge that is defined in the end state is reached, or another begin state edge is reached. An end state edge is denoted by a small minus sign to the left of the edge in the scroll box. In this way large numbers of channel values can be changed with only one input by the user. It should be noted that if the order of edges in the edges array is changed or there is a new edge added, the channel values for a given channel will only update when that channel is selected. Therefore when this happens, on must click on every channel to ensure the proper updating. The signal type displays whether the channel is an analog or digital output channel. This is first defined when adding the channel. If it is a digital channel the only options for the channel value are 0 or 1.

To add a channel click on the add/remove channel box. When this is done the sub vi Add New Channel is displayed. Give the channel a name and define the channel position in the card # and channel # boxes. Take care not to define two channels to the same position. If this is done, an error message will appear. Select the signal type, digital output channels are located as the outputs of the homemade analog to digital converter box and should all be given a card # of 6. When the information is input, click add it and then exit and the channel will appear in the channel array. To remove a channel simply select the channel you want to remove in the scroll box and click remove it. Time Values at This Edge simply displays the edge information of the edge that is selected in the scroll box of the Channel array box and assigned channels lists all of the channels that are

defined. The channel plot gives a plot of the channel values in volts of the selected channel as a function of time in ms.

Front Panel - Other

All of the other boxes on the front panel outside of the main grey area are write boxes. This means they are not inputs, but rather outputs. Most of them are there as trouble shooting tools to analyze a problem. For instance the error boxes will let you know when there was an error in writing to any of the four national instruments boards. These were mainly used in getting the program up and running and haven't been used since the experiments have started. They can be ignored unless major changes to the back panel are made, in which case they may become necessary to trouble shoot again. Any such changes should be saved as a different program name.

Back Panel

The back panel of the program is viewable by clicking show diagram under the Window pull down menu. Due to the size of the program and the fact that much of it is cosmetic in nature and not important for the usability of the program, I will only talk about a few important parts of the back panel. The program is arranged by one large sequence structure which consists of 5 frames (0 thru 4). This structure is the second largest rectangle just inside the while loop which simply keeps the program continuously

running. I will briefly describe each sequence frame below, skipping the ones that are largely cosmetic.

Back Panel – Sequence frame 0

This frame displays the channel array information. The case structure at the top of the frame displays the specific channel information on the front panel when the user selects a channel from the edit/view channel bar.

The sequence structure at the bottom of the frame consists of three frames. The first one includes the add new channel sub vi. It then takes the newly updated channel array and searches for null elements, moving them to the end of the array. The second case structure in this frame searches for matching elements and if any are found causes the assigned channels box on the front panel to start blinking. The second frame in this sequence structure involves updating the channel values at each edge when the increment matching feature is used. This allows the user to increase or decrease a voltage value by a specified amount simply by clicking on the plus or minus boxes under increment value in the channels section of the main program. The third frame in this sequence involves updating the channel voltage information when the edge state feature is used as described above. Specifically it will go through each edge and determine if it is a begin, end, or none edge state and update the channel voltages accordingly.

Back Panel – Sequence frame 1

This frame displays the edge related information. The top of the frame consists of cosmetic code that displays edge information on the front panel when an edge is selected from the edit/view edge bar.

This frame includes the extremely important Add New Edge sub vi. This is a huge sub vi with many, many sub vi's of its own.

Add New Edge sub vi

Although there are four frames in the main sequence structure, the first (frame 0) and last (frame 3) are trivial. Frame 1 contains the sub vi Adiabatic Changer. This sub vi creates the time values and corresponding voltages that make up an adiabatic change. Within the Adiabatic Changer sub vi is located the sub vi Prepare Output Voltage Array sub vi. This sub vi creates the voltages for the adiabatic change for the specified lattice beams or Yag beam. Within this sub vi there are three sub vi's, Z Lattice Main, X Lattice Main, and Y Lattice Main. These sub vi's create the voltages vs time curve for the adiabatic change for the given beam. Z Lattice Main does either the Z Lattice beam or the Yag beam. Within each of these sub vi's is the Lattice Power Calculator rev3 vi. This vi calculates the power versus time curve for the adiabatic change via the specified function; either and exponential for the lattice beams or a inverse time squared for the Yag beam. This power versus time curve is then converted into an a.o.m. control voltage versus time curve via the Interpolate vi located in the Z, X, or Y Lattice Main vi's. This

is done using the user input a.o.m. calibration data that is hand entered into the front panel of the Adiabatic Changer vi.

Frame 2 of the main sequence structure in the Add New Edge vi is where the actual edges and corresponding voltages if it is an adiabatic change are added. This frame consists of a three frame sequence structure. Frame 0 simply inputs the correct edge information into the Define with Respect to and Edge to Remove scroll bars on the front panel of the Add New Edge vi. It also gathers all of the edge parameters for the edge to be added and passes it on to the next frame when action is taken (ie add it, remove it, or exit is pressed). Frame 1 of the three frame sequence structure is where the edge information is added or removed from the edge array. This frame consists of a three option case structure. Case 1 is if an edge or a series of adiabatic edges is to be added. Within Case 1 is a true-false case structure. The false Case is for adding a single edge and simply adds the new single edge into the edge array. The for loop at the top of this case takes the channel array and inserts a blank voltage value for the new edge and shifts the voltage values for edges that occur after the new edge down so that they remain associated with the correct edge. The true Case within Case 1 is for adding a series of adiabatic edges. This case consists of a four frame sequence structure. Frame 0 simply adds to the edge array the series of adiabatic edges adding the absolute time of the defined with respect to edge to the adiabatic time sequence. Frame 1 makes sure that you have listed a channel name in the appropriate A.O. boxes on the Add New Edge front panel. Frame 2 determines which of the A.O. boxes are selected and then creates an array whose elements correspond to the position in the channel array of the adiabatic channel or channels that are written in the A.O. boxes. Frame 3 adds the actual voltages

to the correct channel or channels in the channel array. This frame consists of a three frame sequence structure. Frame 0 adds the analog voltages of the adiabatic change to the correct channels. Frame 1 shifts the edge state information of all the channels so that the proper edge state information stays with the correct edge. Frame 2 initializes a value of 0 for the analog or digital voltage for the added edges for all channels that aren't involved in the adiabatic change. Case 2 of the three option case structure is if an edge or a series of edges is to be removed. This case consists of a two frame sequence. Frame 0 removes the selected edges from the edge array. Frame 1 removes the corresponding analog voltage, digital voltage, and edge state information from all of the channels in the channel array. Case 4 of the three option case structure is for exiting the Add New Edge sub vi. Frame 2 of the three frame sequence structure within frame 2 of the main sequence structure sorts the newly edited edge array in order of increasing absolute time so as to keep the edge array in proper chronological order.

Back Panel – Sequence Frame 2

Frame 2 in the back panel of the main program is for displaying the variable information of the front panel. It also includes the Add New Variable sub vi. Since this feature was never used in these experiments I will not go into detail on this frame.

Back Panel – Sequence Frame 3

This frame contains the code that restores, saves, exports, or clears a timing program when any of these buttons are pushed under Data Functions on the front panel.

Back Panel – Sequence Frame 4

This frame contains the code that writes and outputs the data to the analog and digital output boards. The digital output data is then sent to the timing box which converts the data into a train of digitals pulses which is the timing signal. This timing signal in turn triggers the analog output boards to update their output.

The first case structure within this frame is activated true when the generate signal button is pressed. The second case structure is determined by the Output Values at This Edge Only box on the front panel. If this box is checked, then this case is true. In this case the voltages that correspond to the edge selected on the Edit/View Edge scroll bar are outputted via the AO ONE PT sub vi. This is a built in lab view sub vi that outputs a single voltage on a single channel of an analog output device. If this box is unchecked this case is false, and the timing sequence is initiated.

The first step in this process is the sub vi Gen Array Data which configures the analog output voltages and digital output voltages so that they can be written to the buffers of the analog and digital output boards respectively. The digital output voltages will become the timing signal.

Generate Array Data sub vi

This sub vi consists of a three frame sequence structure, of which only two are important. Sequence frame 0 takes the channel array and creates an output voltage array which can then be written to the buffer of the analog output boards. The first step is the 5 choice case structure (0,1,2,3,6). Cases 1,2 and 3 correspond to the three analog output boards which are devices 1,2 and 3. Theses cases take for each channel the analog output voltages at each edge and put them into a 2D array which is labeled by channel number (row) and edge number (column) so that there is 1 2D array for each analog device. Case 6 corresponds to any channel that is a digital channel. All digital channels must be given a card number of 6 when they are created. There are fourteen digital channels that come out of the homemade analog to digital converter box. Two channels from analog output device # 3 (channels 3 and 6) are designated as sending two analog voltages to the adc box which encode two seven bit binary numbers which are decoded by the adc box and output on the digital output lines. Case 6 takes for digitals channels 0 thru 6 and 7 thru 13 the digital value at every edge and converts the two seven bit binary numbers at every edge into two decimal numbers at every edge. These numbers are then rescaled into voltages so that the 128 possible binary numbers are spread out evenly over the analog output voltage range of 24 volts. This is done by the for loop in the middle of the screen to the right of the 5 choice case structure. The for loop at the top of the screen to the right of the 5 choice case structure simply replaces the output voltages with the newly computed voltages in the channel array for the two designated analog to digital channels (card #3 channels 3, and 6). Then the 3 2D arrays of output voltages are combined into one array and are ready to be written to the analog output board buffers.

Sequence frame 1 in this sub vi creates the timing array which will become the timing signal. The timing signal is output via the NI 6534 digital output board (device #4). This board consists of 32 (0:31) channels, 31 of which are used in series to output the timing signal. Channel 31 is used as a trigger to update a counter and will be discussed later. The sequence at the top of the screen above the main for loop calculates the number of points (bits) in the timing array by dividing the absolute time of the last edge by the time step resolution (one microsecond) and then evenly distributes these bits over the 31 channels to determine the number of bits in each channel (# bits). Then in the small for loop to the left of the large for loop a 32 by # bits array is initialized and broken down into 4 sub arrays each 8 channels wide. This corresponds with how the digital output board groups its channels for purposes of writing data to it, namely into 4 groups of 8 channels. The sequence of code inside the large for loop but to the left of the 4 choice case structure takes the absolute time of each edge and determines which cluster of 8 channels in the digital output board this timing pulse belongs in. The 4 choice case structure (0,1,2,3) corresponds to the 4 clusters of 8 channels and the code is identical in each. Within this case structure are 2 for loops. In combination these for loops search for the correct position to place the pulse that corresponds to the current edge. The first (larger) for loop searches the 8 channels within each cluster and the second (smaller) for loop searches the # bits bits within each channel. The true false case structure within the smaller for loop does nothing (false case) until the correct pulse position is found (true case). When the correct pulse position is found another true false case is encountered. This checks to see if the pulse position is the equal to # bits (i.e. if it is the very last bit of the channel). If this is so (true case), it causes problems with the timing signal and so the

timing pulse is moved 1 time step resolution forward. If this is false no additional action is taken. Then the correct bit in the 2D array is made true to create the timing update pulse in the timing signal. Then the cluster of 4 2D arrays is sent to a small for loop which takes channel 31 and makes all of the bits false except the last one which is made true. This is the trigger pulse which will update a counter later on. Then the first bit of channel 0 is made false for safety. Then the array is configured for writing to the digital board. Each of the 4 2D arrays is transposed and the 8 bit binary number that exists at each bit position for the 8 channels together is converted into an integer. These are then put into a 1D array for each bit position and then a 2D array for each cluster of 8 channels. It is then transposed again and reduced to a 1D array and is then ready for writing to the digital output 6534 board.

After the Generate Array Data sub vi the analog voltages and the digital voltages for the timing signal are ready to be written to their respective boards. This is done via the five frame sequence structure located inside the true false case structure and inside a while loop following the Gen Array Data sub vi. This case structure is permanently set to true as the false case wrote to the boards in a slightly different and less efficient way. The while loop repeats itself as long as the generate signal button is pressed and the output values at this edge only box is unchecked. Frame 0 simply sets channel 1 on the 6534 board to low or zero so that the first timing pulse is seen. Frame 1 consists of a three frame sequence structure which simply gives two digital pulses on lines 0 and 1 of the digital output of the analog output board device # 1. These devices have 8 digital outputs that can only be operated statically and are never used except for these two lines. The pulses are to zero the two counters that are used later on to piece together the timing

signal. This process will be explained in detail later. Frame 2 actually writes the analog voltages to the 3 analog output boards. The sequence consists of three built in labview vi's which are in a typical order for writing to these types of boards and can be found in many labview built in examples from the help menu. The first vi AO Config defines which channels are to be written to and sets up a buffer to store the data that are written. The next vi AO Write writes the data to the buffer. The next vi AO Start generates the analog output. The clock source is set to I/O connector which means the voltages are updated by an external clock (i.e. the timing signal). Frame 3 is equivalent to frame 2 except it is for a digital output board. There currently is not such a board in use for output voltages and so the case structure is set to false. One could use another 6534 board to create digital output voltages directly and thus skip the analog to digital converter box, if this is implemented, this case would have to be set true. Frame 4 writes the data to the 6534 output board for the timing signal. It is again a common sequence of built in labview vi's that can be found in the examples. DIO Config sets up the buffer for storing the data. DIO Write writes the data to the buffer. Trigger Config sets up the board to start output via an external trigger, in this case a digital trigger synchronized to 60 Hz line so that the experiment starts at the same place every time with respect to line voltage. DIO Start generates the output, in this case it is set to output its buffer continuously since it must output the buffer 31 times to complete the timing signal (remember the timing signal is the first 31 channels of the 6534 board in series). It is set to update its output every microsecond (i.e. the timing resolution) via the clock frequency input.

The data is continuously output via the while loop in frame 0 of the two frame sequence structure directly to the right of the four frame sequence structure. This while loop runs until either the generate signal button is pressed (which is not normally done while the experiment is running) or the analog output boards have outputted their entire buffer. When the latter happens this means one run of the experiment is complete. The AO write vi will output a Boolean true when the buffer is completely output. Then this while loop ends, the analog and digital boards' buffers are cleared, and the larger while loop repeats itself, meaning the data is written again to the boards and the 6534 board starts its output upon receiving the line synched trigger. This process will continue until the user stops the output. The best way to do this is to check the output values at this edge only box, the current run the of the experiment will complete and the there will be static output on the analog boards corresponding to whichever edge is selected (should be Start Cycle Ref where there are no potentially damaging voltages being applied). This completes the back panel description of the timing program.

Timing Signal

The output of the 6534 board must be spliced together to create the actual timing signal that updates the analog output boards. This is done by a homemade digital circuit box located beside the timing computer and voltage output lines.

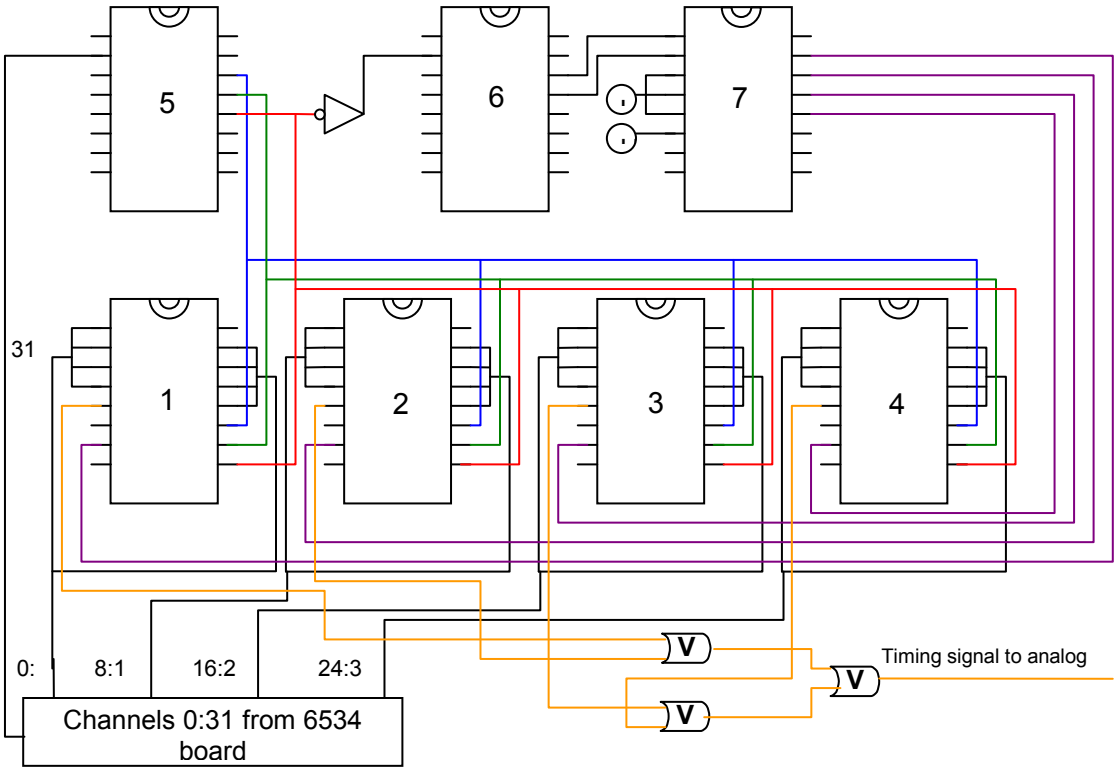
5
6
7
1
2
3
4
31
0:
8:1
16:2
24:3
Channels 0:31 from 6534 board
V
V
V
Timing signal to analog

Multiplexor

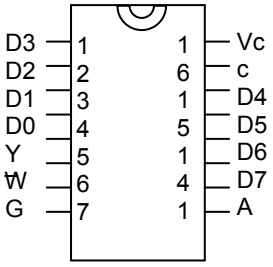

Demultiplexor

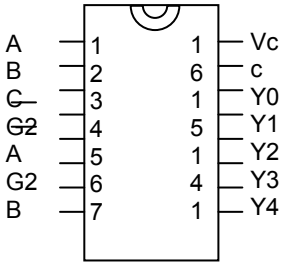

Counter

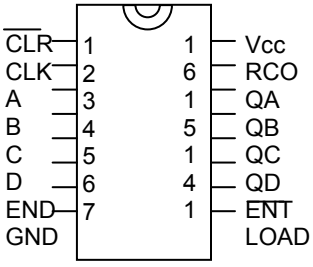

Multiplexor

Inputs				Outputs	
Select					
C	B	A	$\overline{G}$	Y	W
X	X	X	H	L	H
L	L	L	L	D0	$\overline{D0}$
L	L	H	L	D1	$\overline{D1}$
L	H	L	L	D2	$\overline{D2}$
L	H	H	L	D3	$\overline{D3}$
H	L	L	L	D4	$\overline{D4}$
H	L	H	L	D5	$\overline{D5}$
H	H	L	L	D6	$\overline{D6}$
H	H	H	L	D7	$\overline{D7}$

Demultiplexor

G1	$\overline{G2A}$	$\overline{G2B}$	C	B	A	Y0	Y1	Y2	Y3
H	L	L	L	L	L	L	H	H	H
H	L	L	L	L	H	H	L	H	H
H	L	L	L	H	L	H	H	L	H
H	L	L	L	H	H	H	H	H	L

Multiplexors : 1, 2, 3, 4
Counters : 5, 6
Demultiplexor : 7

Appendix B: Lattice Ti Sapphire motorized micrometer

In this experiment it is necessary to change the wavelength of the lattice light after the lattice cooling phase and before the ramping up of the 2D optical lattice. This must be done quickly and accurately during each individual experimental run. This is done using a Newport LTA-HS motorized micrometer which has a resolution of 35nm. It is connected to the bi-refrigent filter in the lattice Ti-Sapphire laser cavity via a homemade mount. This allows for a triggered changing of the laser frequency during the experiment and subsequent change back for the beginning of the next experimental run.

The experimentally determined best lattice wavelength for the lattice cooling phase of the experiment is 779.980 nm or 130GHz blue detuned from the D2 line of ^{87}Rb. In order to avoid heating via spontaneous emission during the 2D lattice phase we must further detune the lattice. We found an acceptable range from 3.15THz (773.9 nm) to 6THz (768.3 nm). To change the wavelength the motorized micrometer moves the bi-refrigent filter a specified amount via an external trigger from an output voltage channel. During the lattice cooling at 130GHz the lattice Ti-Sapphire is not locked at all. After changing the wavelength for the 2D lattice phase the laser is locked via the etalon feedback. The integrator is turned on by a remote switch controlled by an output voltage channel.

The micrometer is controlled by a Newport motion controller, model number ESP300, which is connected to computer 3 (the timing computer). The software to interact with the controller can be found under programs/ESP Motion Controllers/ESP-Util. First turn on the controller, the controller screen will prompt you to turn on the motor; then zero the

micrometer by the Home button on the controller face. The micrometer is connected to axis 1. Then open the ESP-Util software, the Select Com Port should be on 1 and the Select Port Type should be on Serial (RS232). After clicking on open port you will be prompted whether or not you want to reset the controller, select no. Then a box will appear saying the ESP300 has detected a LTA-HS stage on axis 1, click ok. Then click the terminal icon and a screen will appear where you can input commands. Since the stage is on axis 1 of the controller all commands must be preceded by 1. A list of commands and example programs can be found in the ESP300 user manual located in C:\Newport\ESPMotionControllers\Controllers\ESP300\Doc.

To read the current position of the micrometer type in 1tp and hit return, the position in mm will be outputted. To move the controller and thus change the wavelength of the laser, enter 1paxx, where xx is the position in mm where you want to move it to. The wavelength of the laser can be monitored by the wavemeter at the far end of the optical table. A template notepad program exists for automatically moving and returning the micrometer during the experiment (changedetbytrig). It is located in MyDocuments\StagePrograms and is shown below:

3xx

3ep

bo0h

2dl

0uh

1pa28.027

0ul

1pa28.307

2jl

qp

3ex

To use the program first confirm the micrometer positions that correspond to the desired wavelengths. Enter the position for the 2D lattice phase after the first 1pa line. Enter the position for the lattice cooling phase after the second 1pa line and save the program. Back in the ESP Util click on Transmit text file and open the changedetbytrig file. The program will be downloaded onto the command terminal screen. The micrometer will then move from its original position (ie the lattice cooling phase wavelength) to the 2D lattice wavelength upon receiving an external trigger (rising edge) and then will move back to the lattice cooling phase wavelength upon receiving another trigger (falling edge). After the wavelength is changed to the 2D lattice position the etalon is locked and just before it is changed back, the etalon is unlocked via another

external trigger. Going thru the program step by step, the first line erases program 3 which is the name of this program, so to write a new program 3 to the controller the previous program 3 must be erased. The next line 3ep enters the program mode, so that subsequent commands are not executed immediately but rather stored in memory as part on program 3. The line bo0h sets the digital input/output bit 0 as an output. This means value of this bit can be externally changed (in this case by the output voltage channel Ti:S Motor Trig) and its value can be read by the controller. The line 2dl defines this line as the beginning of a loop. When the command 2jl is encountered, the program jumps back to the line 2dl. The line 0uh causes the program to wait until bit 0 becomes high before continuing. The line 1pa28.027 moves the micrometer to the 2D lattice phase position. The line 0ul waits until bit 0 becomes low; then the micrometer returns to the lattice cooling position by 1pa28.307. The line 2jl jumps back to the line 2dl so that this loop continues indefinitely. The line qp quits programming mode and the line 3ex executes program 3 so that the program starts. Once the program is executed the loop will run continuously so that you never have to re enter the program even in between starting and stopping the main timing program. One can monitor that the wavelength is changing on the wavemeter. To stop the loop type in qp and hit enter. After stopping the program one should occasionally type in 0xx and hit enter to erase all programs from memory. If too many programs are stored in the memory the controller can crash and reset the velocity parameters ol and jw (which should be 0.5 mm/s); if this happens one must reset these velocities by entering ol0.5 and jw0.5. If these velocities are too high the micrometer may return an error and lock up.

Appendix C: One dimensional distribution analysis

For the 1D experiments, many times it is necessary to know the details of the distribution after expansion in the 1D tubes. Details about the shape are important, namely how close is the distribution to a Gaussian; also important is the rms width of the distribution and the integrated area (which is proportional to the number of atoms). The distributions are analyzed using a mathematica notebook, the details of which will be described below.

The first thing that was necessary to do was to compare the shapes of the distributions to Gaussians and to each other (Quantum Newton's Cradle paper). This mathematica notebook will be described first. Later, for the thermalization by tunneling paper, we wanted to know not only the shapes of the distributions but also the rms widths; for this purpose the original mathematica notebook was slightly modified. This modified notebook will be discussed second. These notebooks are located in the timing computer under C:\\mathematica files\ V-dist-of-thermalization.

Mathematical Notebook 1: Compare 1D distribution at early time to 1D distribution at later time

This particular file is in the folder gamma 1: V-dist-of-thermalization-data-w-convolution-15T-comp-40T-g-1.0-RAW-II-correct-0%.

Vaxis={-1021.020.....892.710}

Vaxis is the array which represents the 1D axis of the distribution in micrometers. This axis on the Curve Fit software is originally in pixels. This axis is converted into micrometers, zeroed at the maximum of the distribution and then made into a text file. It is then copied and pasted into mathematica.

fifteentau={-0.007……..-0.017}

This array, in this case, is the distribution at fifteen tau. It is the optical thickness (proportional to density) as a function of the Vaxis position. For every Vaxis position there is a corresponding value for optical thickness. It is similarly made into a text file and pasted into mathematica.

dist15tau=Thread[{Vaxis,fifteentau}]

Dist15tau combines Vaxis and fifteentau into one two dimensional array for purposes of plotting.

ListPlot[dist15tau]

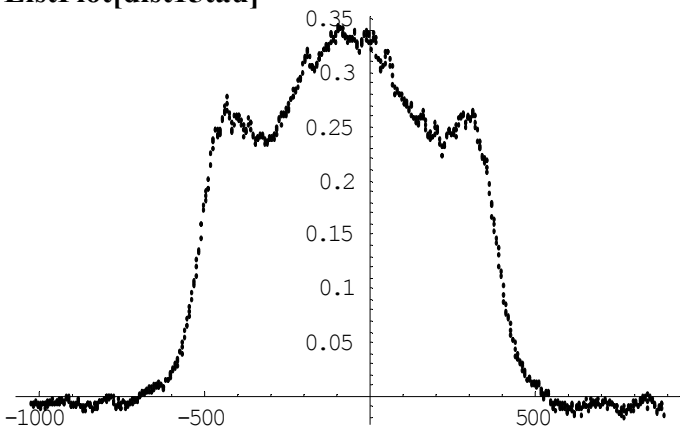

Graphics

ListPlot[dist15tau] plots each optical density point vs the corresponding Vaxis position and so is an exact plot of the distribution.

fun15tau=Interpolation[dist15tau]

InterpolatingFunction[{{-1021.02,892.71}},<>]

This step creates a continuous function fun15tau as a function of Vaxis so that for any value of Vaxis a value for the optical thickness is obtained by interpolating between the known values.

Plot[fun15tau[z],{z,-1021.02,892.71}]

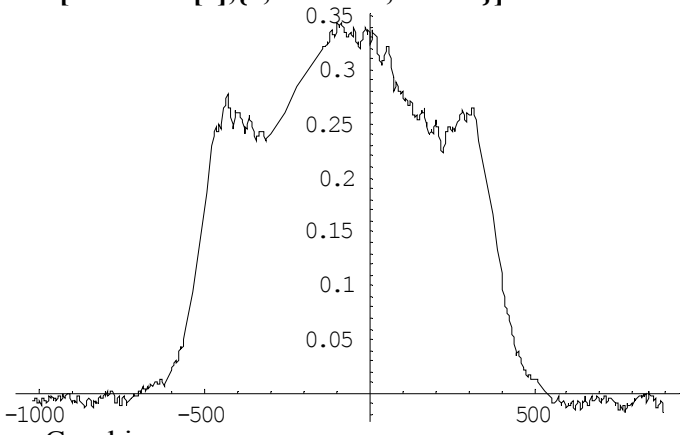

Graphics

This step plots the continuous function fun15tau.

$$\text{fun15tauconv} = \text{Table}\left[\text{NIntegrate}\left[\text{fun15tau}[z_0] * \sqrt{\frac{2}{\pi}} * \frac{1}{114.2}\, \text{Exp}\left[\frac{-2*(z-z_0)^2}{114.2^2}\right], \{z_0, -1021.02, 892.71\}\right], \{z, -1021.02, 892.71, 2.73\}\right]$$

This step convolves the distribution at the earlier time (15tau) by some gaussian to account for the heating that takes place during the holding time in the 1D tubes. It uses the continuous distribution created at 15 tau in the integral to create an array that represents the distribution after heating. In this case we want to compare the 15tau distribution to the distribution at 40tau.

fun15tauconv40t=Thread[{Vaxis,fun15tauconv}]

This step threads the new dist15tauconv40t array with Vaxis to create a 2D array.

ListPlot[fun15tauconv40t]

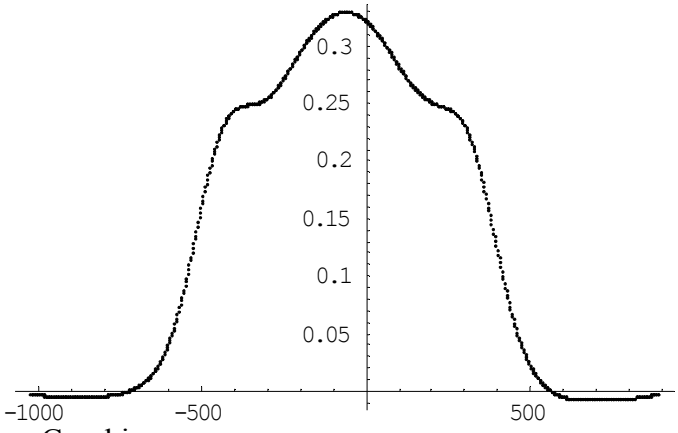

Graphics

fun15tauconv40tcont=Interpolation[fun15tauconv40t]

InterpolatingFunction[{{-1021.02,892.71}},<>]

Plot[fun15tauconv40tcont[z],{z,-1021.02,892.71}]

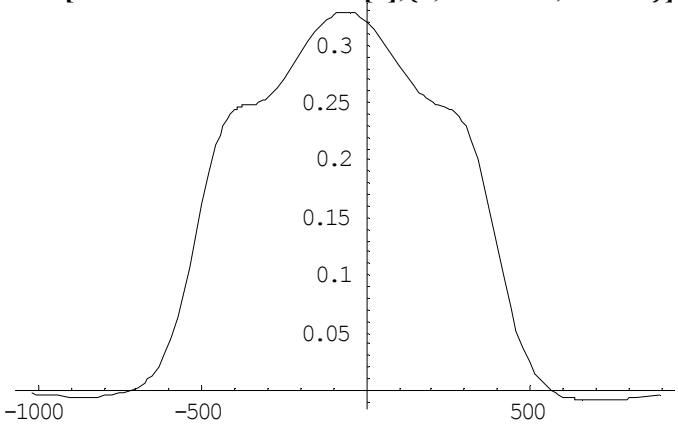

Graphics

These three steps are equivalent to those done for the 15tau distribution above. First the 15tau convolved array is plotted. Then this array is converted into a continuous function via interpolation and the new continuous, convolved distribution is plotted.

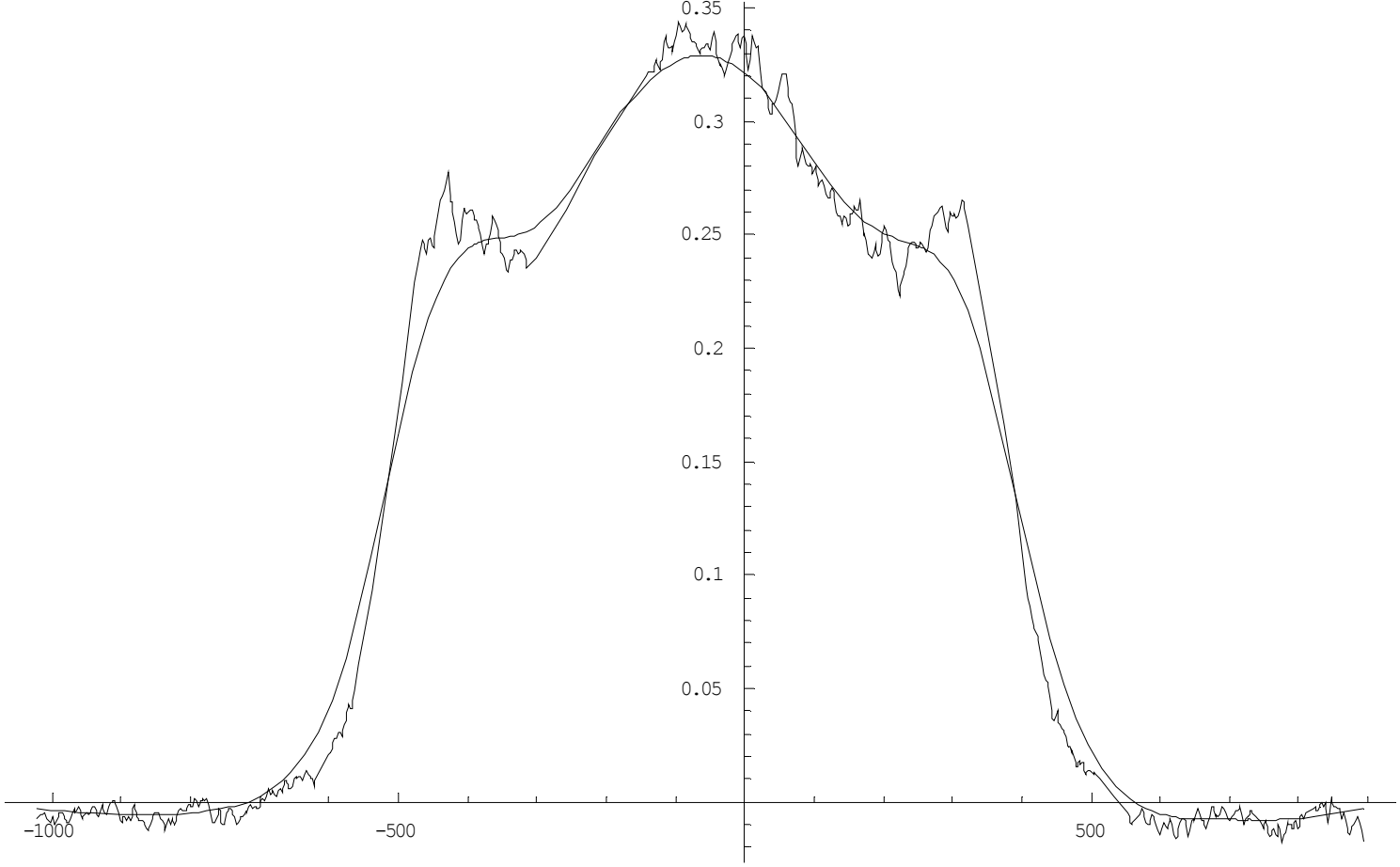

Plot[{fun15tauconv40tcont[z],fun15tau[z]},{z,-1021.02,892.71}]

Graphics

This step plots both of the continuous distributions for 15 tau and 15tau convolved 40tau so the effect of the heating can be seen directly.

fortytau={0.000…….-0.011}

This step creates the raw array for the actual distribution at 40tau via a text file in the same manner as was done for 15tau and Vaxis.

distfortytau=Thread[{Vaxis,fortytau}]

This creates a 2D array for the 40tau array and Vaxis.

funfortytau=Interpolation[distfortytau]
InterpolatingFunction[{{-1021.02,892.71}},<>]
Plot[funfortytau[z],{z,-1021.02,892.71}]

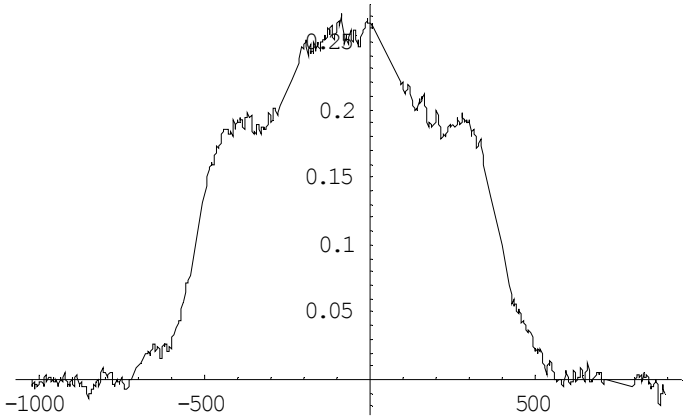

Graphics

These two steps create the continuous distribution at 40tau and plot it as a function of Vaxis.

Plot[{fun15tauconv40tcont[z]+.006,1.281*funfortytau[z]+.0031},{z,-1021.02,892.71}]

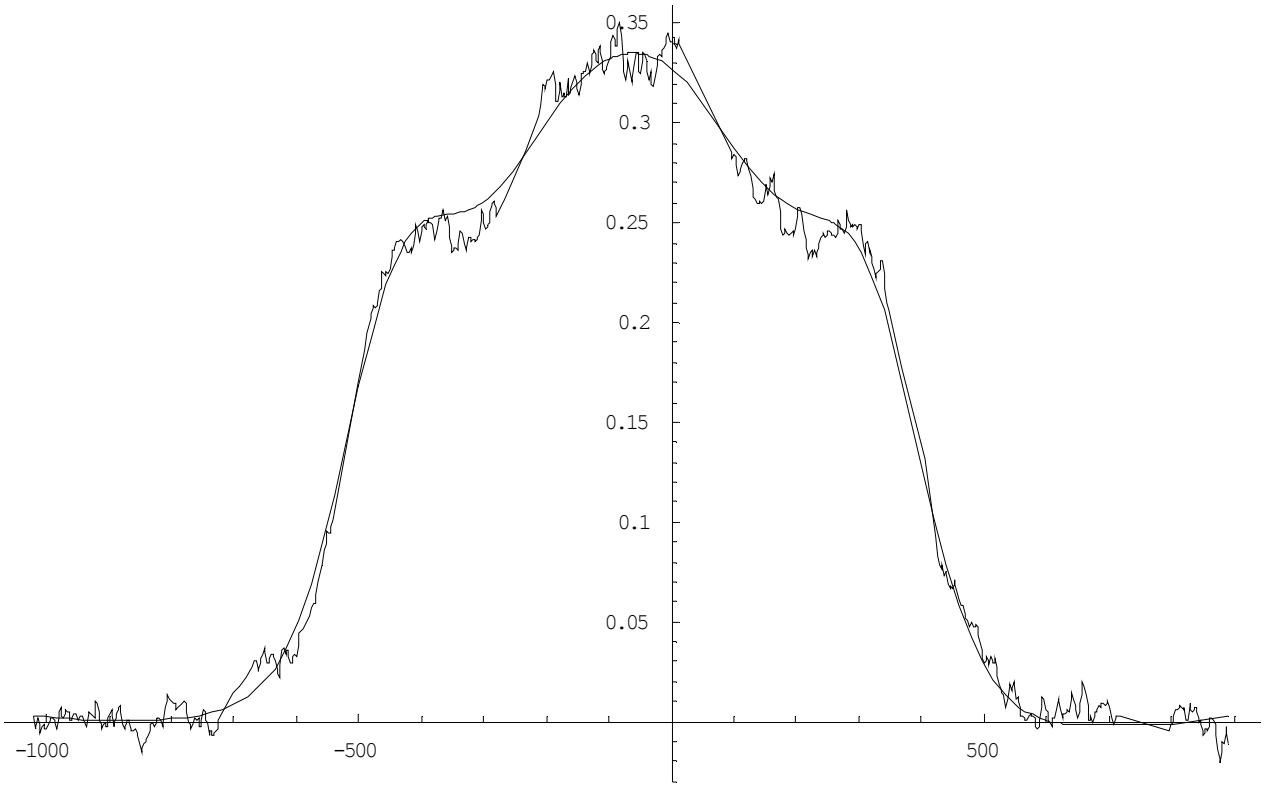

Graphics

This step plots together the 15tau distribution convolved and the 40tau distribution. Both of the offsets are adjusted to give a net zero offset by eye and the 15tau convolved

distribution is rescaled to account for atom number loss so that the total area is nearly equal. This is a first cut comparison plot only and is not the final result.

afterfilter=Thread[{Vaxis,Table[(Sum[funfortytau[If[(z+2.73*i) -1022,-1021.02,If[(z+2.73*i) 893,892.71,(z+2.73*i)]]],{i,-8,8,1}])/(2*8+1),{z,-1021.02,892.71,2.73}]}]

This step takes the 40tau distribution and filters it to reduce the noise. It does so by using an 8 point spread filter function where it takes every point and averages over plus or minus 8 points (ie 8*2.73 =22 micrometers). The new filtered 40tau array is threaded with Vaxis to create a 2D array.

fun40taufilter=Interpolation[afterfilter]
InterpolatingFunction[{{-1021.02,892.71}},<>]
Plot[{funfortytau[z],fun40taufilter[z]},{z,-1021.02,892.71}]

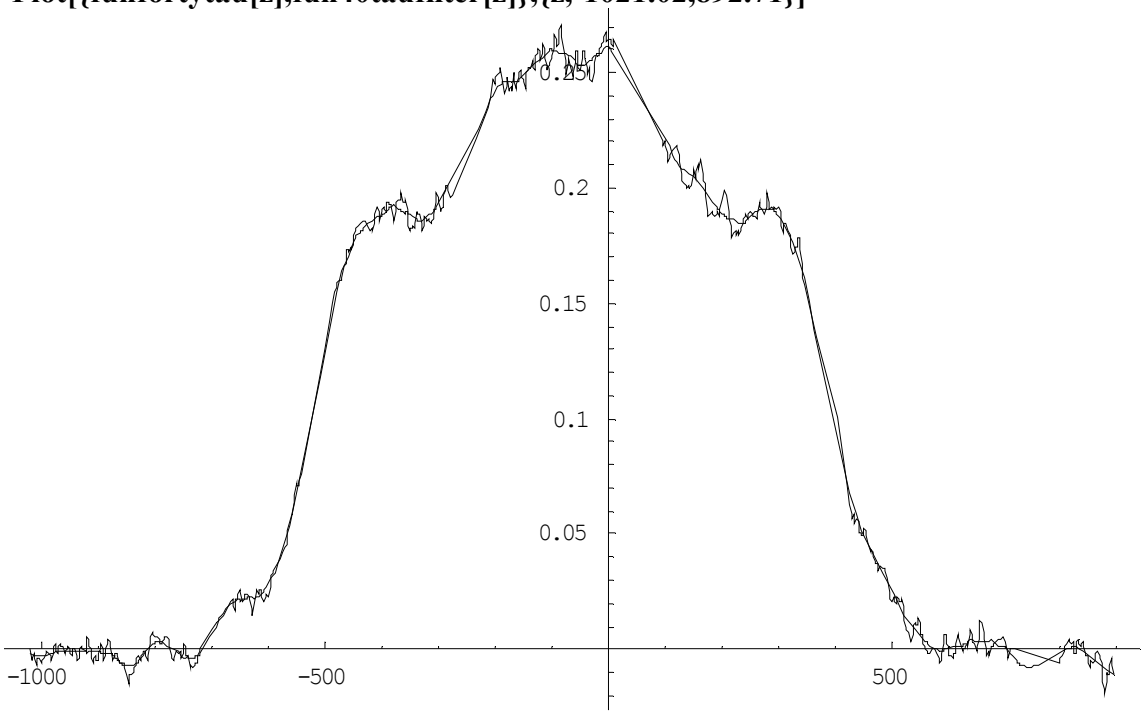

Graphics

This step converts the 40tau filtered array into a continuous distribution and plots the filtered distribution versus the unfiltered raw distribution.

The remainder of the steps involve comparing the distributions at 15tauconv and 40tau with each other and with a gaussian. Both the 40tau raw and 40tau filtered distributions were used, but here the 40tau raw distribution is used.

Chisq = Sum[((0.7773 * fun15tauconv40tcont[z] + .0049) - (funfortytau[z] + .0022))^2, {z, -1021.02, 892.71, 2.73}]

0.0302273

```
Minimize[Sum[((funfortytau[z] + A))^2, {z, -1021.02, -821.73, 2.73}] + Sum[((funfortytau[z] + A))^2, {z, 619.71, 892.71, 2.73}],
 {A}]
```

{0.00440539,{A 0.00223429}}

```
Minimize[Sum[((B * fun15tauconv40tcont[z] + C) - (funfortytau[z] + .0022))^2, {z, -1021.02, 892.71, 2.73}], {B, C}]
```

{0.0302266,{B 0.777323,C 0.00486528}}

These three steps in conjunction compute the Chi squared value of the 15tauconv distribution to the 40tau raw distribution. The first step computes the Chi squared. The second step minimizes the offset of the 40tau raw distribution by minimizing the sum of the square of the tails with respect to the offset. The third step minimizes the Chi squared of the 15tau convolved distribution to the 40tau raw distribution with the minimized offset with respect to B (the rescaling factor for the 15tau convolved distribution to account for atom number loss) and C (the offset of the 15tau convolved distribution).

Leftavg=Sum[funfortytau[z]+.0022,{z,-1021.02,-821.73,2.73}]/73
-0.000482192
Rightavg=Sum[funfortytau[z]+.0022,{z,619.71,892.71,2.73}]/100
0.000292

```
Var =
  (Sum[((funfortytau[z] + .0022) - Leftavg)^2, {z, -1021.02, -821.73, 2.73}] +
     Sum[((funfortytau[z] + .0022) - Rightavg)^2, {z, 619.71, 892.71, 2.73}]) / (73 + 100)
```

0.0000253203

In the end we want the reduced Chi squared (ie the deviation beyond the expected deviation due to noise alone). For this we must compute the variance (or the Chi squared due to noise). We use the 40tau raw distribution and compute the average value for the left and right side tails. The variance Var or the average of the square of the noise is then computed.

```
Chisqgof = Sum[((0.7773 * fun15tauconv40tcont[z] + .0049) - (funfortytau[z] + .0022))^2 / Var, {z, -1021.02, 892.71, 2.73}] / 701
```

1.70299
Plot[{0.7773*fun15tauconv40tcont[z]+.0049,funfortytau[z]+.0022},{z,-1021.02,892.71}]

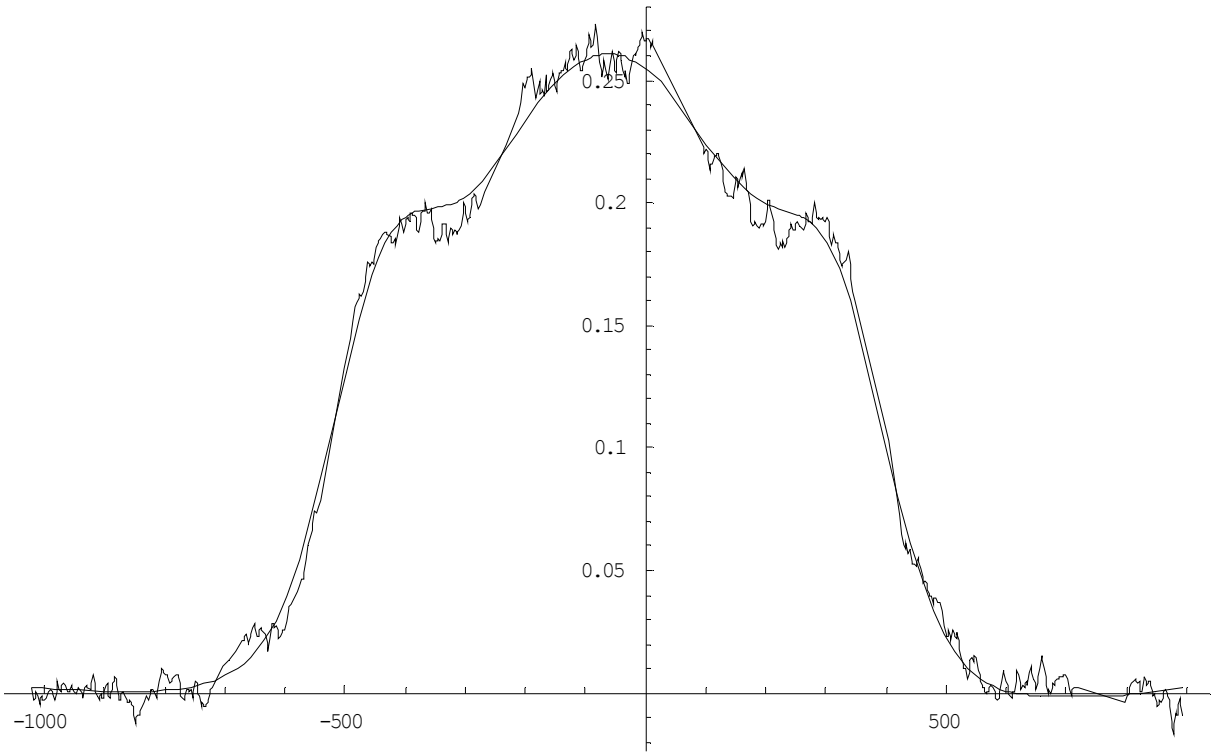

Graphics

We then compute the reduced Chi squared (or goodness of fit) by dividing the raw Chi squared by the variance. The next step plots the best fit results for the 15tau convolved and the 40tau raw distributions.

```
Plot[((0.7773*fun15tauconv40tcont[z] + .0049) - (funfortytau[z] + .0022))^2 - Var, {z, -1021.02, 892.71},
 PlotRange→ {-.0001, .0007}]
```

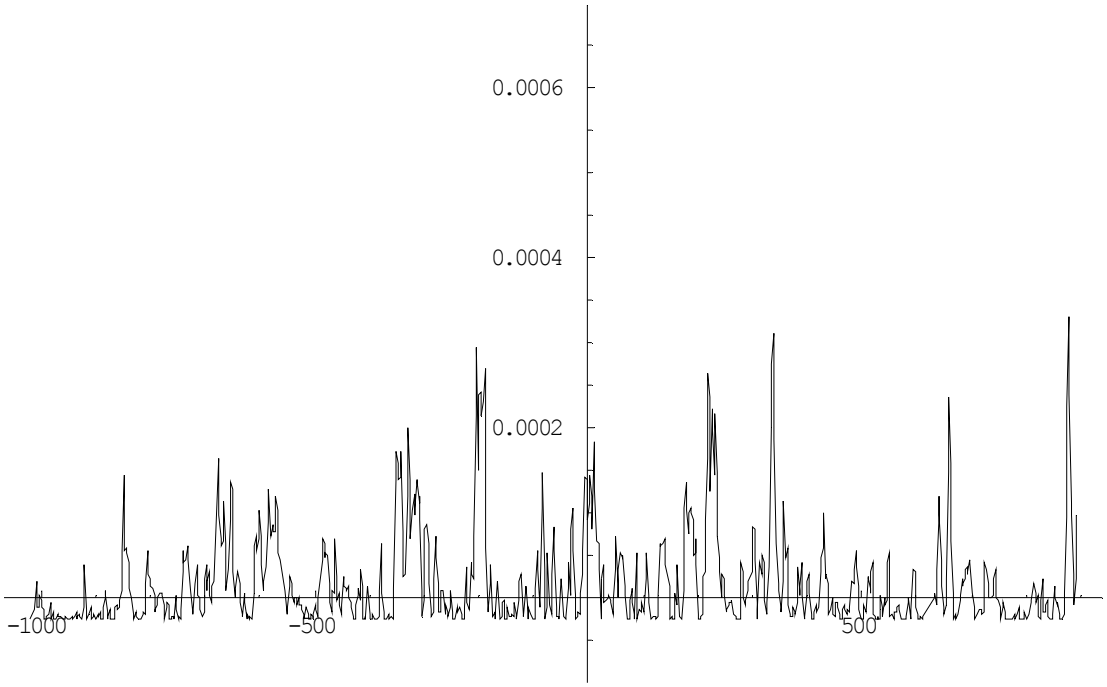

Graphics

```
Plot[((0.7773 * fun15tauconv40tcont[z] + .0049) - (funfortytau[z] + .0022))^1, {z, -1021.02, 892.71}, PlotRange → {-.03, .03}]
```

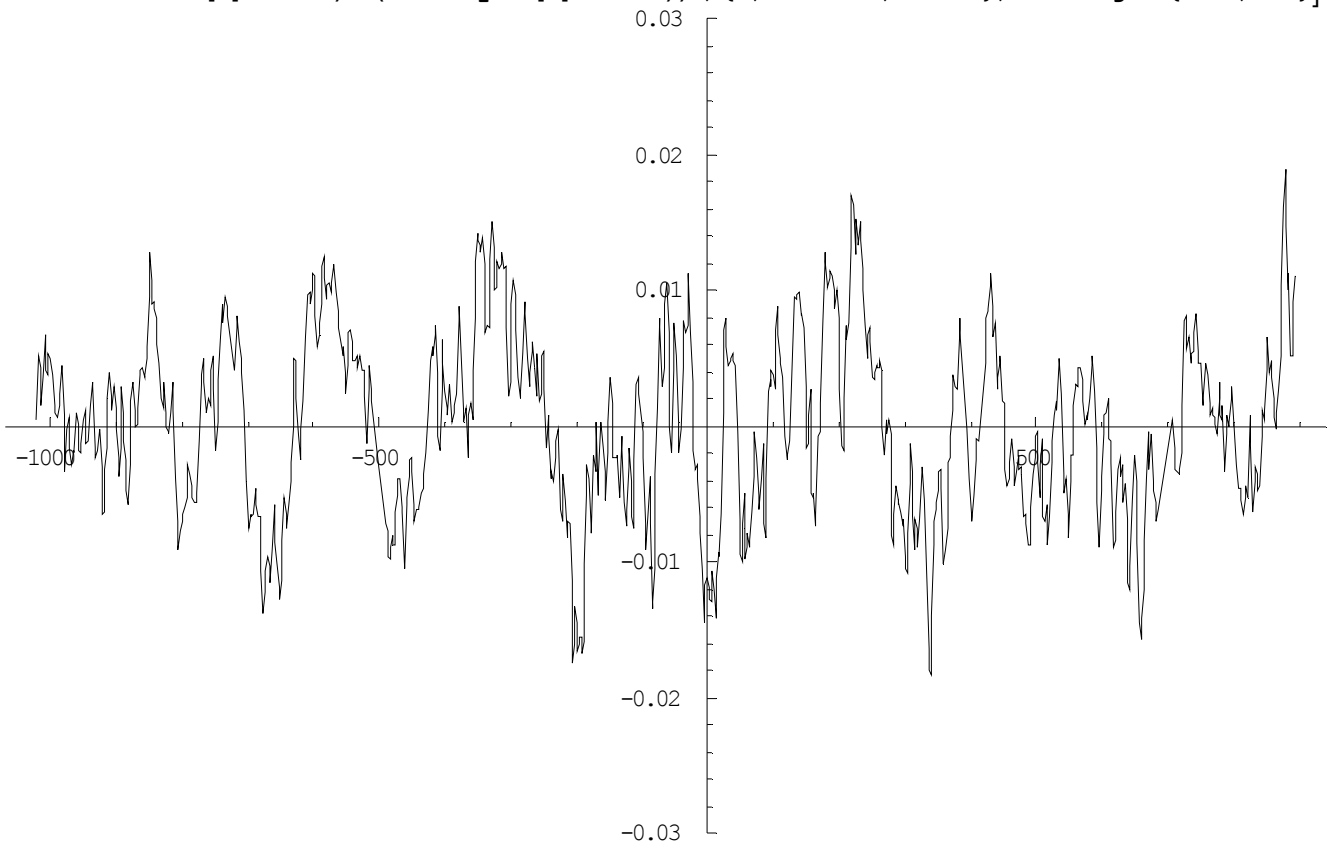

Graphics

The next two steps plot the difference of the Chi squared and the variance and the Chi respectively to check for any tendencies where the 15tau convolved distribution and the 40tau raw distribution may miss.

The remaining steps compare the distributions to gaussians.

```
fitresult = NonlinearFit[distfortytau, {A * Exp[-2 * (z - B)^2 / w^2]}, z, {A, w, B}, MaxIterations → 1000, AccuracyGoal → 10,
  PrecisionGoal → 10, ShowProgress → True]
```

Iteration: 45 ChiSquared: 0.374077 Parameters: {0.268984,624.327,-62.8774}
Iteration: 46 ChiSquared: 0.374077 Parameters: {0.268984,624.327,-62.8774}
Iteration: 47 ChiSquared: 0.374077 Parameters: {0.268984,624.327,-62.8774}
Iteration: 48 ChiSquared: 0.374077 Parameters: {0.268984,624.327,-62.8774}
Iteration: 49 ChiSquared: 0.374077 Parameters: {0.268984,624.327,-62.8774}

$$0.268984\, e^{-5.13105\times10^{-6}\,(62.8774+z)^2}$$

This step uses a best fit iteration to fit the 40tau raw distribution to a gaussian. The resulting Chi squared and gaussian function is then displayed.

fitresultplt=Plot[fitresult,{z,-1300,1300},PlotRange {-.05,0.3}]

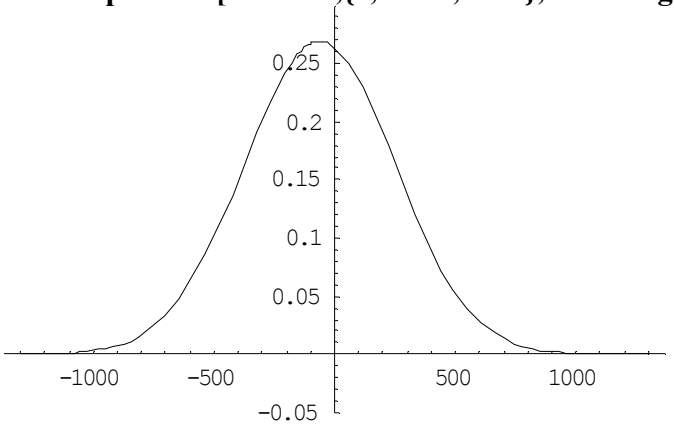

Graphics

AA=Plot[funfortytau[z],{z,-1021.02,892.71}]

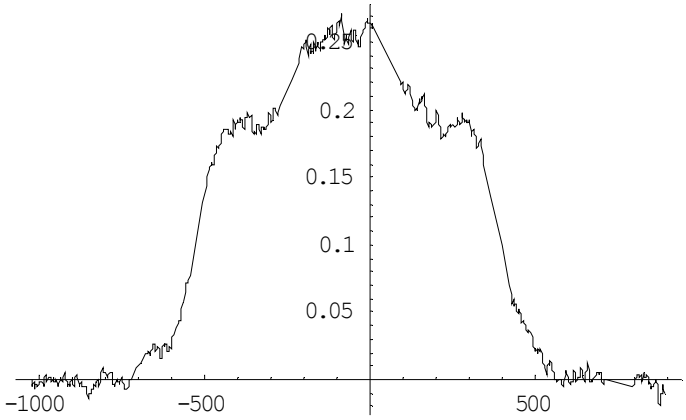

Graphics

Show[fitresultplt, AA]

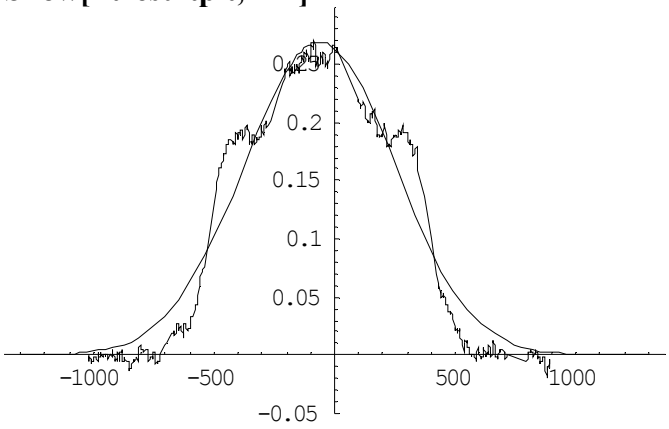

Graphics

The resulting gaussian is then plotted together with the 40tau raw distribution.

$$\text{Rms40tau} = \left(\frac{\text{NIntegrate}[(0.7773 * \text{fun15tauconv40tcont}[z] + .0049) * (z + 62.9)^2, \{z, -1021.02, 892.71\}]}{\text{NIntegrate}[(0.7773 * \text{fun15tauconv40tcont}[z] + .0049), \{z, -1021.02, 892.71\}]} \right)\text{^0.5}$$

272.643

$$\text{Rms40tau} = \left(\frac{\text{NIntegrate}[(\text{funfortytau}[z] + .0022) * (z + 62.9)^2, \{z, -1021.02, 892.71\}]}{\text{NIntegrate}[(\text{funfortytau}[z] + .0022), \{z, -1021.02, 892.71\}]} \right)\text{^0.5}$$

271.436

$$\text{RmsGfit} = \left(\frac{\text{NIntegrate}\left[0.3741 * \text{Exp}\left[\frac{-2*(z+62.9)^2}{545^2}\right] * (z + 62.9)^2, \{z, -1021.02, 892.71\}\right]}{\text{NIntegrate}\left[0.3741 * \text{Exp}\left[\frac{-2*(z+62.9)^2}{545^2}\right], \{z, -1021.02, 892.71\}\right]} \right)\text{^0.5}$$

271.696

Sum40tau=NIntegrate[funfortytau[z]+.0022,{z,-1021.02,892.71}]

205.281

$$\text{SumGfit} = \text{NIntegrate}\left[0.3007 * \text{Exp}\left[\frac{-2*(z+62.9)^2}{545^2}\right], \{z, -1021.02, 892.71\}\right]$$

205.303

A more correct analysis is to compare the 40tau raw distribution to a gaussian which has the same rms width and the same area (number). This is the gaussian which obeys conservation of energy and atom number. In the first step above the rms width of the 15tau convolved distribution is calculated (but not really used here). In the second step the rms width of the 40tau raw distribution is calculated. In the third step the rms width of a gaussian is computed. The width of the gaussian is varied until the rms width equals that of the 40tau raw distribution. Note the importance of the offset of the center of the distribution in these calculations. In the next two steps the area of the 40tau raw distribution and corresponding gaussian are calculated. The amplitude of the gaussian is adjusted such that these are equal.

$$\text{BB} = \text{Plot}\left[0.3007 * \text{Exp}\left[\frac{-2*(z+62.9)^2}{545^2}\right], \{z, -1021.02, 892.71\}\right]$$

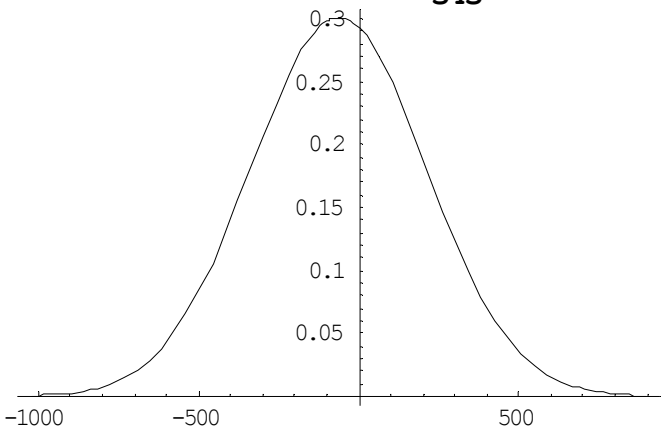

Graphics

AAA=Plot[funfortytau[z]+.0022,{z,-1021.02,892.71}]

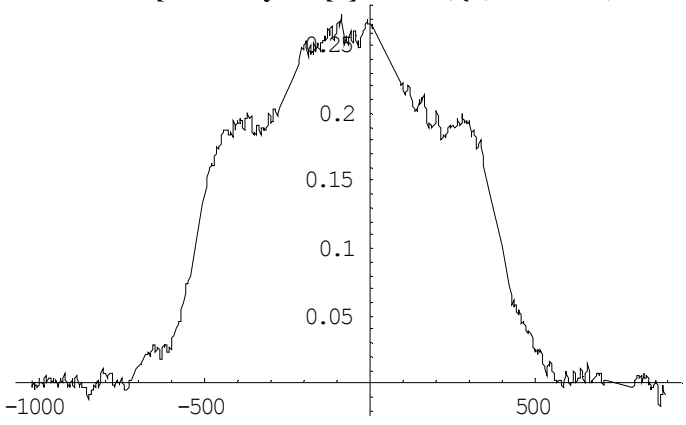

Graphics

Show[BB, AAA]

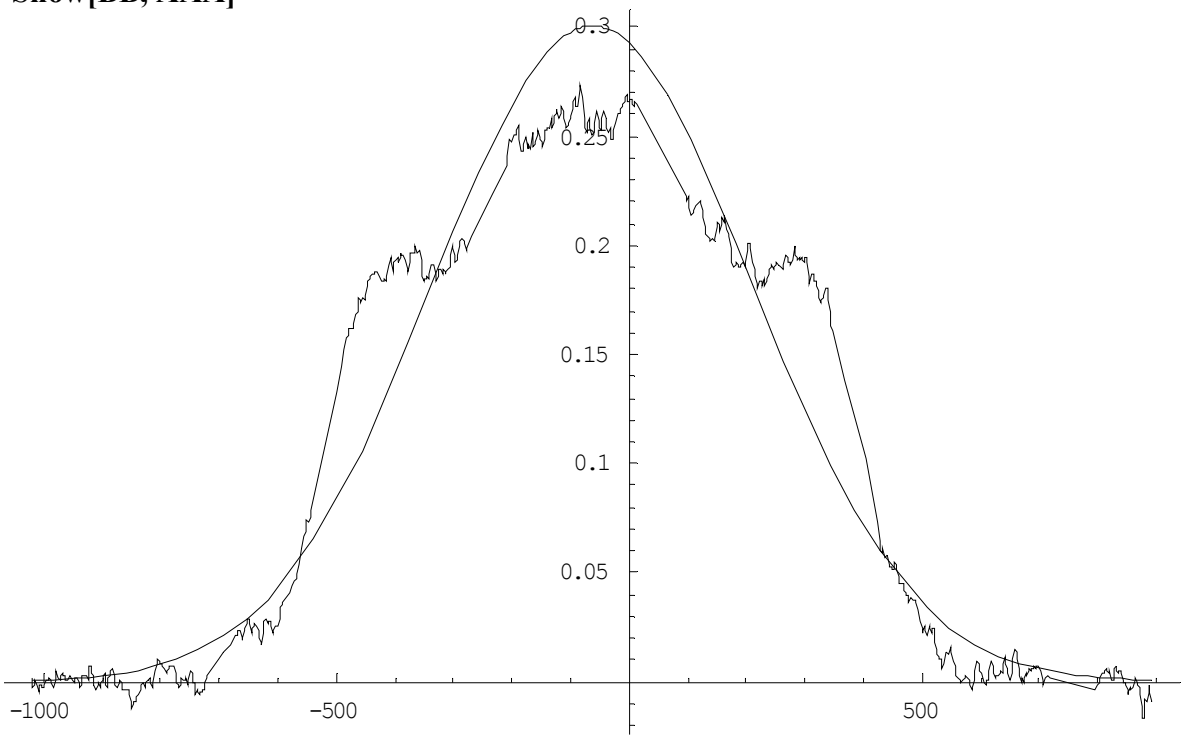

Graphics

The next three steps plot the same rms width and area gaussian and the 40tau raw distribution.

$$\text{ChisqtoG} = \text{Sum}\left[\left(0.3007 * \text{Exp}\left[\frac{-2*(z+62.9)^2}{545^2}\right] - (\text{funfortytau}[z] + .0022)\right)^2, \{z, -1021.02, 892.71, 2.73\}\right]$$

0.579392

$$\text{ChisqtoGgof} = \text{Sum}\left[\left(0.3007 * \text{Exp}\left[\frac{-2*(z+62.9)^2}{545^2}\right] - (\text{funfortytau}[z] + .0022)\right)^2 \Big/ \text{Var}, \{z, -1021.02, 892.71, 2.73\}\right] \Big/ 701$$

32.6426

The last two steps compute the raw Chi squared and the reduced Chi squared respectively of the 40tau raw distribution compared to the same rms width and area gaussian.

Mathematica Notebook 2: Compute the rms width of a 1D distribution after symmeterizing.

This particular file is in the folder V-therm-1Dto3D\gamma~1 4-13-06: Vtherm-data-w-conv-2-Z-comp-70T-3-243-350mW-3.2THz-auto ave offset.nb

Much of the code in this notebook is identical to the previous one and will be skipped. The main difference in this notebook is that the distribution is mirror reflected and averaged so as to make it symmetrical. There are also several steps taken to make the notebook more automated. Since we are not comparing two distributions here, I will start about midway down as the first half is identical code to the first notebook involving the convolution and such.

twentytau={-0.002……..0.001};
dist20tau=Thread[{Vaxis,twentytau}];
fun20tau=Interpolation[dist20tau]
InterpolatingFunction[{{-1124.76,969.15}},<>]

These steps create the array for the distribution, thread it with Vaxis and create the continuous function for the distribution. In this case the distribution is at 70tau even though it says twentytau. It is much easier to keep the name the same than change it every time, hence the discrepancy.

Plot[fun20tau[z],{z,-1111.11,982.8},PlotRange {-0.05,0.25}]

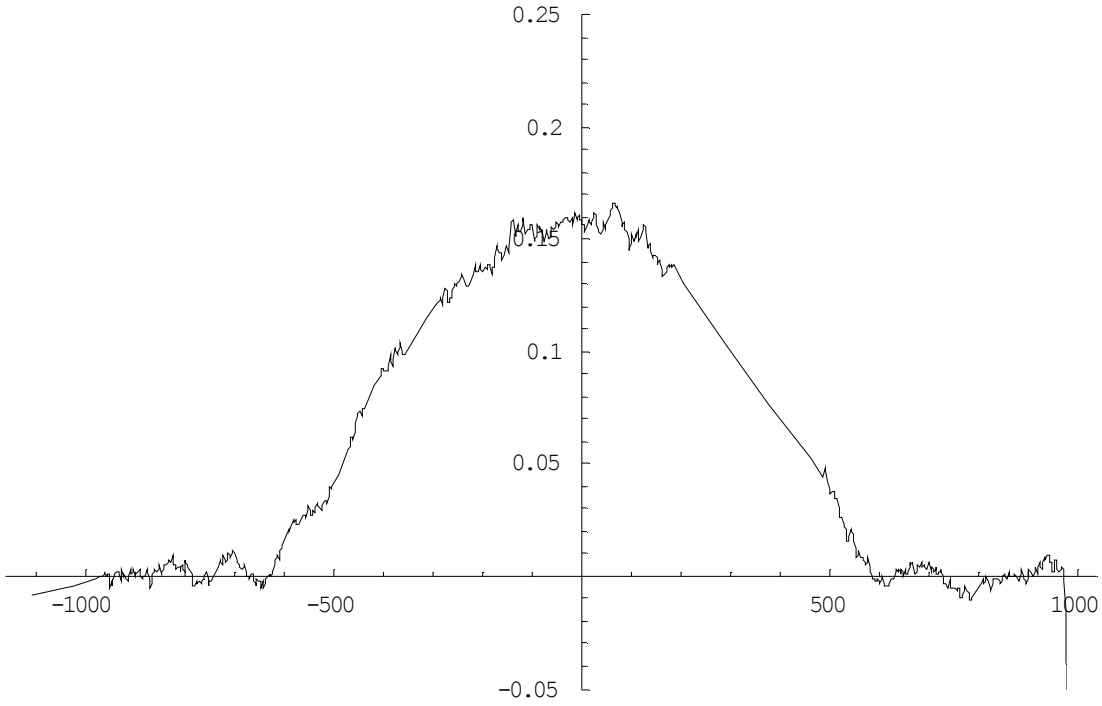

Graphics

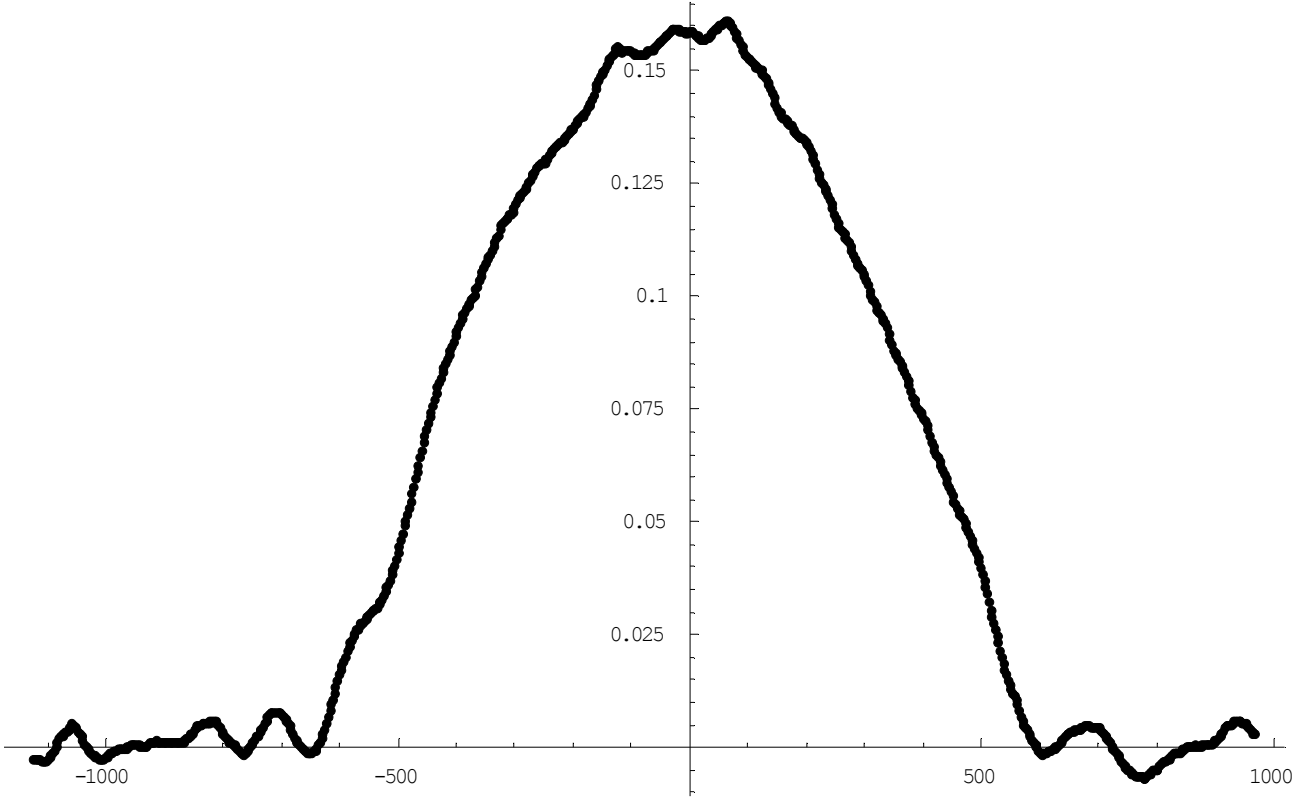

This plots the 70tau distribution.

vm=Min[Vaxis]
vx=Max[Vaxis]
offs=0.0005
fun20taufilter=ListPlot[Thread[{Vaxis,Table[(Sum[fun20tau[If[(z+2.73*i) (Round[vm]-1),vm,If[(z+2.73*i) Round[vx],vx,(z+2.73*i)]]]+offs,{i,-8,8,1}])/(2*8+1),{z,vm,vx,2.73}]}]]
-1124.76
969.15
0.0005

Graphics

These steps create a name for the minimum (vm) and maximum (vx) value for the Vaxis. Then a offset (offs) is defined for the distribution. Then the distribution is filtered with an 8 point spread filter function (as done in the first notebook), threaded with Vaxis and plotted.

afterfilter2=Thread[{Vaxis,Table[(Sum[fun20tau[If[(z+2.73*i) (Round[vm]-1),vm,If[(z+2.73*i) Round[vx],vx,(z+2.73*i)]]]+offs,{i,-8,8,1}])/(2*8+1),{z,vm,vx,2.73}]}];

This step filters the distribution by an 8 point spread filter function in an identical fashion as the previous step. However instead of creating a ListPlot it simply creates a 2D array.

$$\texttt{fitresult2 = NonlinearFit}\left[\texttt{afterfilter2, }\left\{\texttt{A*Exp}\left[\frac{\texttt{-2*(z-B)}^2}{\texttt{w}^2}\right]\right\}\texttt{, z, \{A, w, B\}, MaxIterations} \to \texttt{1000, AccuracyGoal} \to \texttt{10, PrecisionGoal} \to \texttt{10, ShowProgress} \to \texttt{True}\right]$$

Iteration: 60 ChiSquared: 0.0568908 Parameters: {0.167455,604.957,-20.8304}
Iteration: 61 ChiSquared: 0.0568908 Parameters: {0.167455,604.957,-20.8304}
Iteration: 62 ChiSquared: 0.0568908 Parameters: {0.167455,604.957,-20.8304}
Iteration: 63 ChiSquared: 0.0568908 Parameters: {0.167455,604.957,-20.8304}
Iteration: 64 ChiSquared: 0.0568908 Parameters: {0.167455,604.957,-20.8304}
Iteration: 65 ChiSquared: 0.0568908 Parameters: {0.167455,604.957,-20.8304}

$$0.167455\, e^{-5.46488\times10^{-6}\,(20.8304+z)^2}$$

This step does a best fit of the filtered distribution to a gaussian and reports the Chi squared and the best fit gaussian function.

fitresult2plt=Plot[fitresult2,{z,-1300,1000},PlotRange {-.05,0.25}]

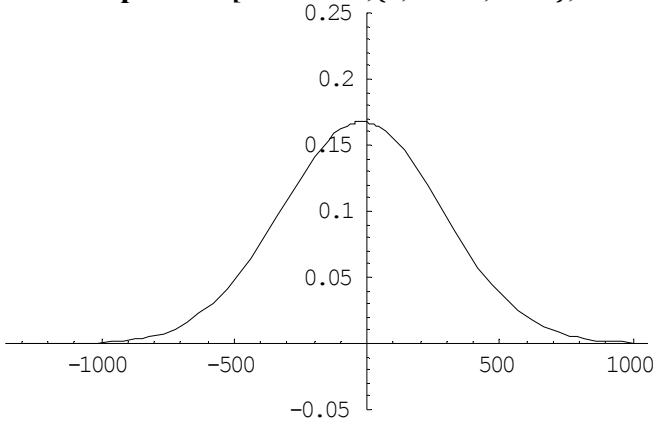

Graphics

Show[fitresult2plt, fun20taufilter]

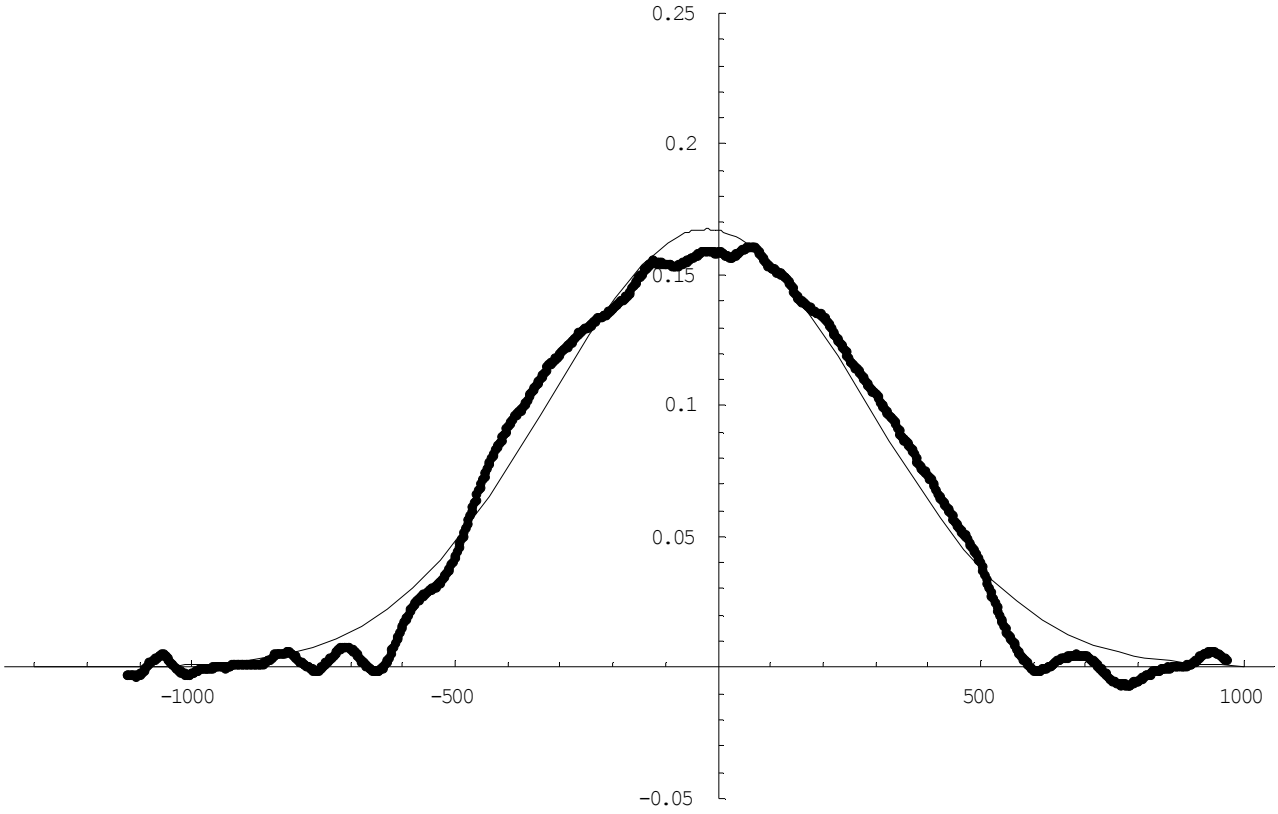

Graphics

The resulting best fit function and the filtered distribution are then plotted together.

fun30taufiltercont=Interpolation[afterfilter2]
vcc=14.98
InterpolatingFunction[{{-1124.76,969.15}},<>]
14.98

$$\text{Rms30taufiltercont} = \left(\frac{\text{NIntegrate}[(\text{fun30taufiltercont}[z]) * (z - \text{vcc})^2, \{z, \text{vm}, \text{vx}\}]}{\text{NIntegrate}[(\text{fun30taufiltercont}[z]), \{z, \text{vm}, \text{vx}\}]} \right) \text{^0.5}$$

274.557

wwtry = 529

$$\text{RmsofGauss} = \left(\frac{\text{NIntegrate}\left[\left(1.0 * \text{Exp}\left[\frac{-2*(z-\text{vcc})^2}{\text{wwtry}^2}\right]\right) * (z - \text{vcc})^2, \{z, \text{vm}, \text{vx}\}\right]}{\text{NIntegrate}\left[\left(1.0 * \text{Exp}\left[\frac{-2*(z-\text{vcc})^2}{\text{wwtry}^2}\right]\right), \{z, \text{vm}, \text{vx}\}\right]} \right) \text{^0.5}$$

529
264.194
Sum30taufiltercont=NIntegrate[fun30taufiltercont[z],{z,vm,vx}]

123.082

$$\text{atry} = 0.209$$

$$\text{SumofGauss} = \text{NIntegrate}\left[\text{atry} * \text{Exp}\left[\frac{-2*(z-\text{vcc})^2}{\text{wwtry}^2}\right], \{z, \text{vm}, \text{vx}\}\right]$$

0.209

138.545

$$\text{Plot}\left[\left\{\text{atry} * \text{Exp}\left[\frac{-2*(z-\text{vcc})^2}{\text{wwtry}^2}\right], \text{fun30taufiltercont}[z]\right\}, \{z, \text{vm}, \text{vx}\}\right]$$

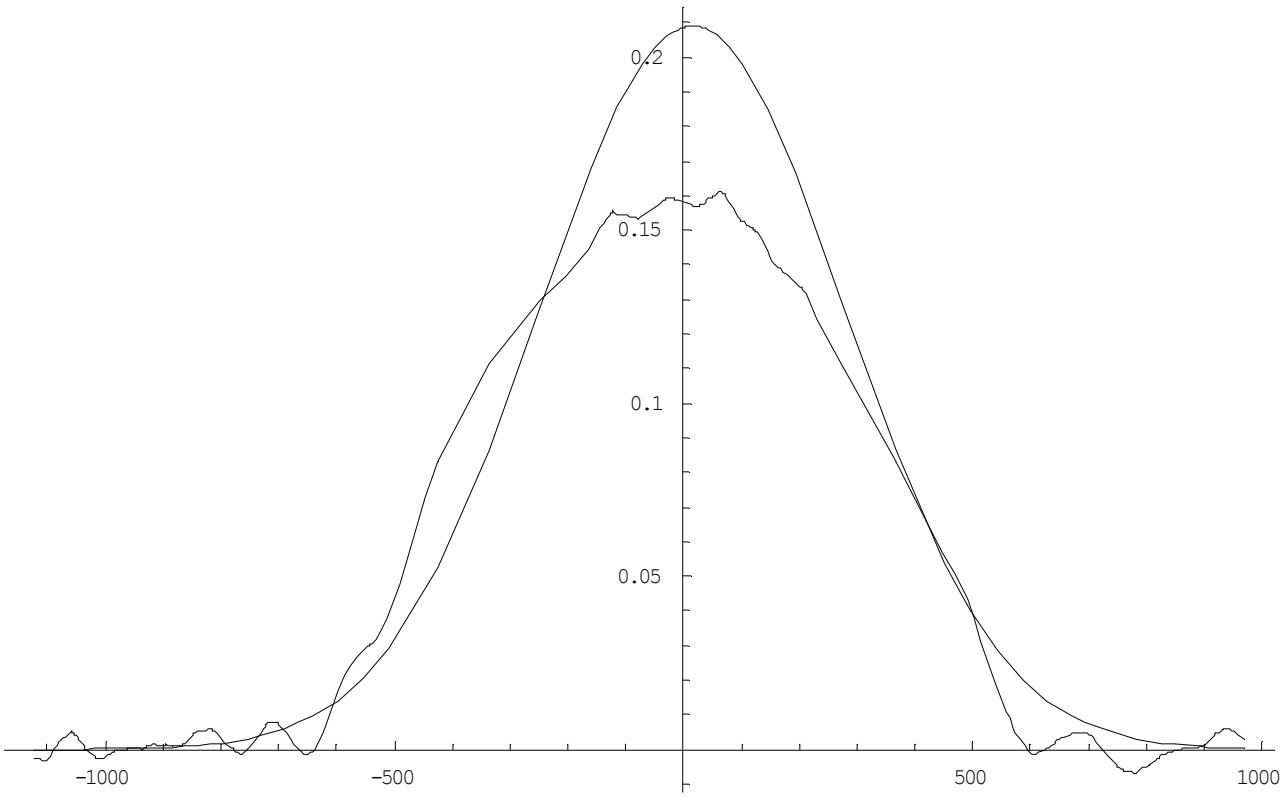

Graphics

These steps are nearly identical to those in the first notebook. First a continuous function for the filtered distribution is created. Again the name is 30tau simply because it is easier not to change the name. Then the center of the distribution is defined (vcc). Then the rms width and area of the filtered distribution and a corresponding gaussian are computed so as to match them and the resulting same rms and area gaussian and the distribution are plotted.

$$\text{ChisqtoG} = \text{Sum}\left[\left(\text{atry} * \text{Exp}\left[\frac{-2*(z-\text{vcc})^2}{\text{wwtry}^2}\right] - (\text{fun30taufiltercont}[z])\right)^2, \{z, \text{vm}, \text{vx}, 2.73\}\right]$$

0.328299

Finally, the Chi squared between the distribution and the same rms width and area gaussian is calculated.

Everything that follows from here is quite similar to what is described above except that it is done for the mirror reflected filtered distribution.

```
(*reflect 20tau array and average to get symmetric distribution*)
(*middle point element is*)
flipelement=(-vm-13.65)/2.73
 407.
 L=Length[twentytau]
 768
 (*must cut the first 412-(768-412) elements to ensure reflection about middle
point*)
 cut=(L-flipelement)*2
 722.
 Vaxis'=Take[Vaxis,-(cut-1)];
 twentytau'=Take[twentytau,-(cut-1)];
 mirror20tau'=Reverse[twentytau'];
 dist20tau'=Thread[{Vaxis',twentytau'}];
 distmirror20tau'=Thread[{Vaxis',mirror20tau'}];
```

The first step defines the flipping point for the mirror reflection. The next step defines the size of the raw 70tau distribution as L. To ensure symmetry after mirror reflection, the flipping point must be at the center of the distribution. The variable cut gives the size of the distribution that has the flipping point at the center. Then the Vaxis and raw 70tau distribution are shortened to this length. Then the shortened raw 70tau distribution is reversed (ie mirror reflected) and both the unflipped and flipped distributions are threaded with the new Vaxis' to create a 2D arrays.

```
Show[ListPlot[distmirror20tau'],ListPlot[dist20tau']]
```

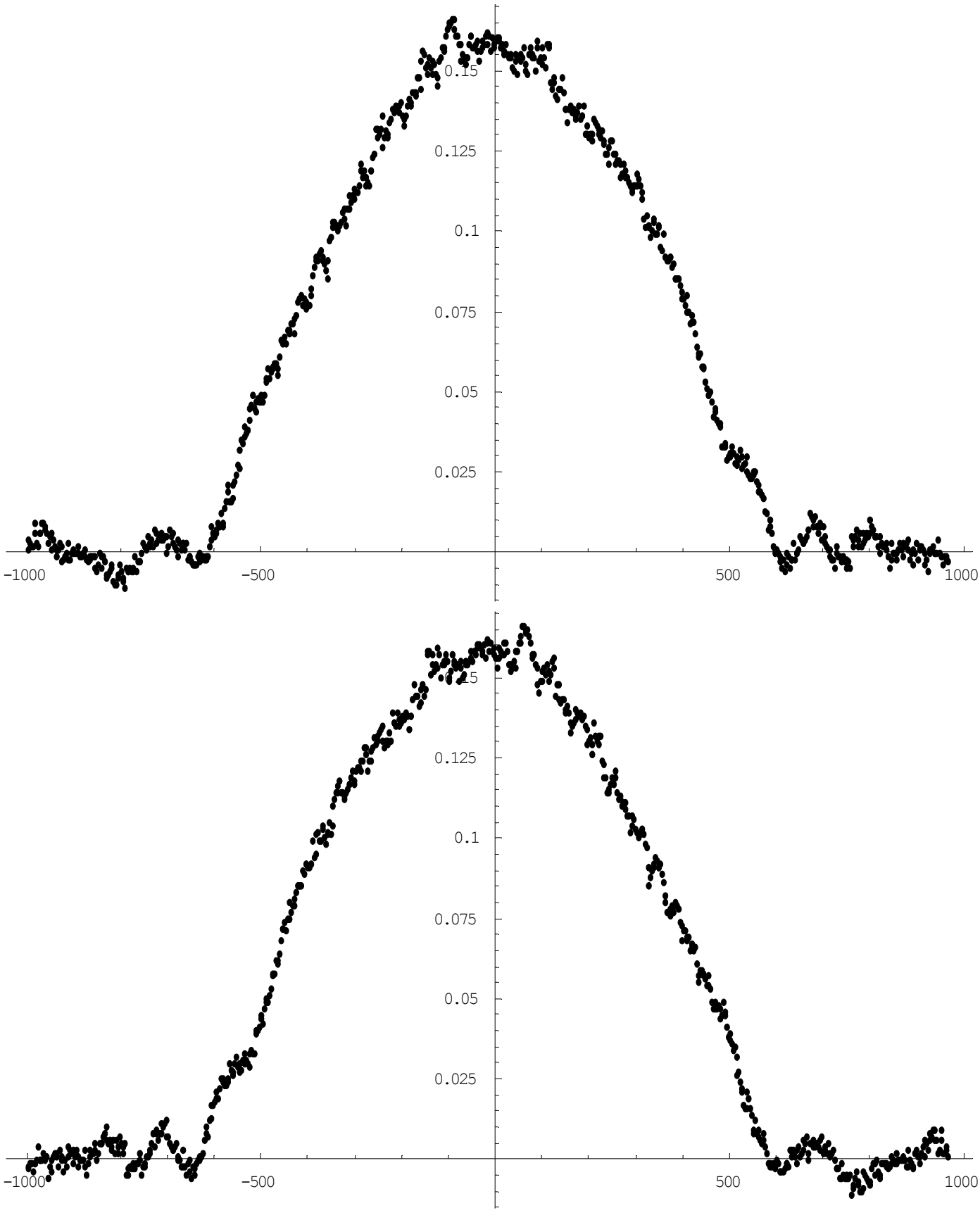
0.15
0.125
0.1
0.075
0.05
0.025
-1000
-500
500
1000
0.15
0.125
0.1
0.075
0.05
0.025
-1000
-500
500
1000

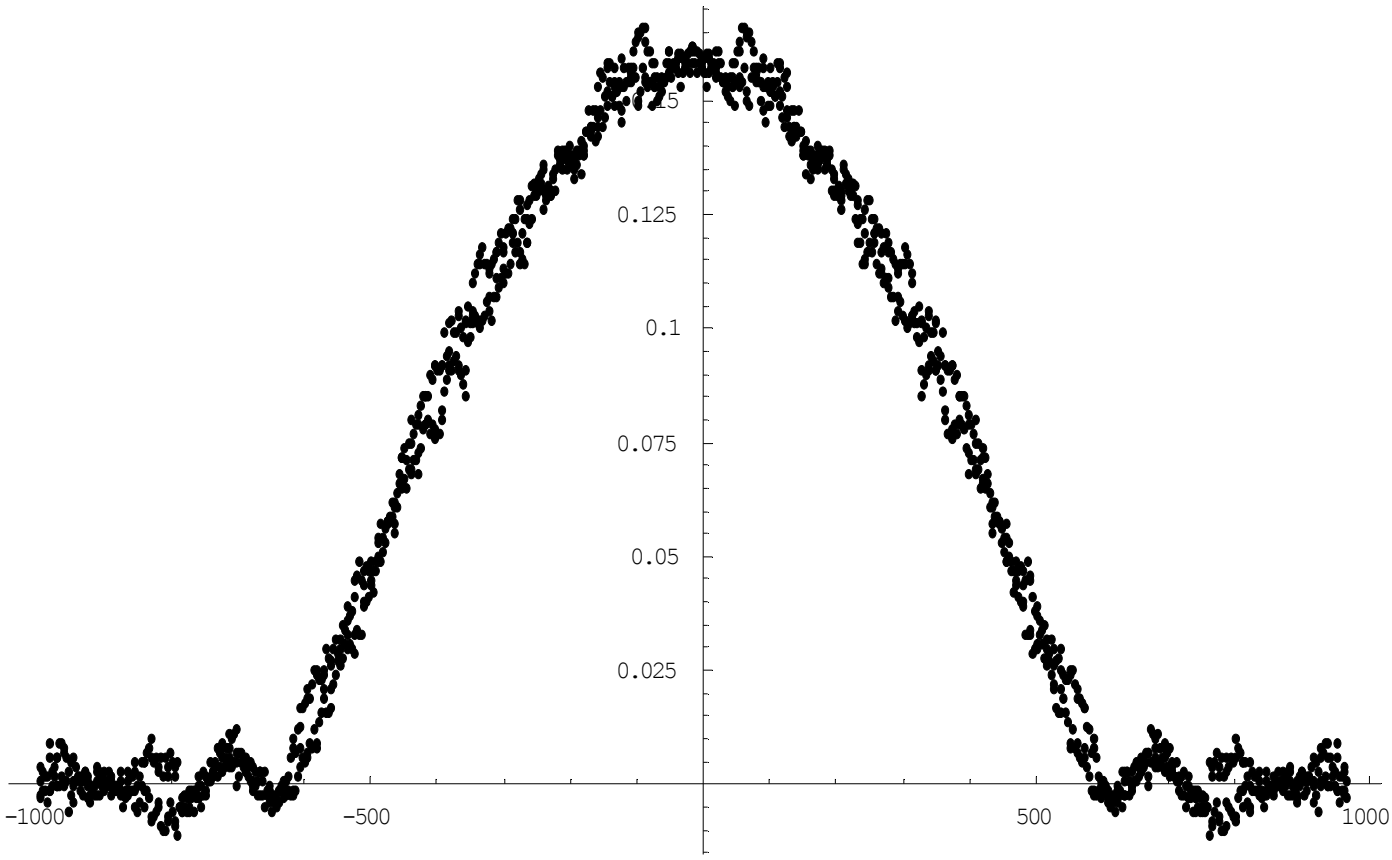

Graphics

Then the flipped and unflipped distributions are plotted both singly and on top of one another.

ListPlot[avesym20tau']

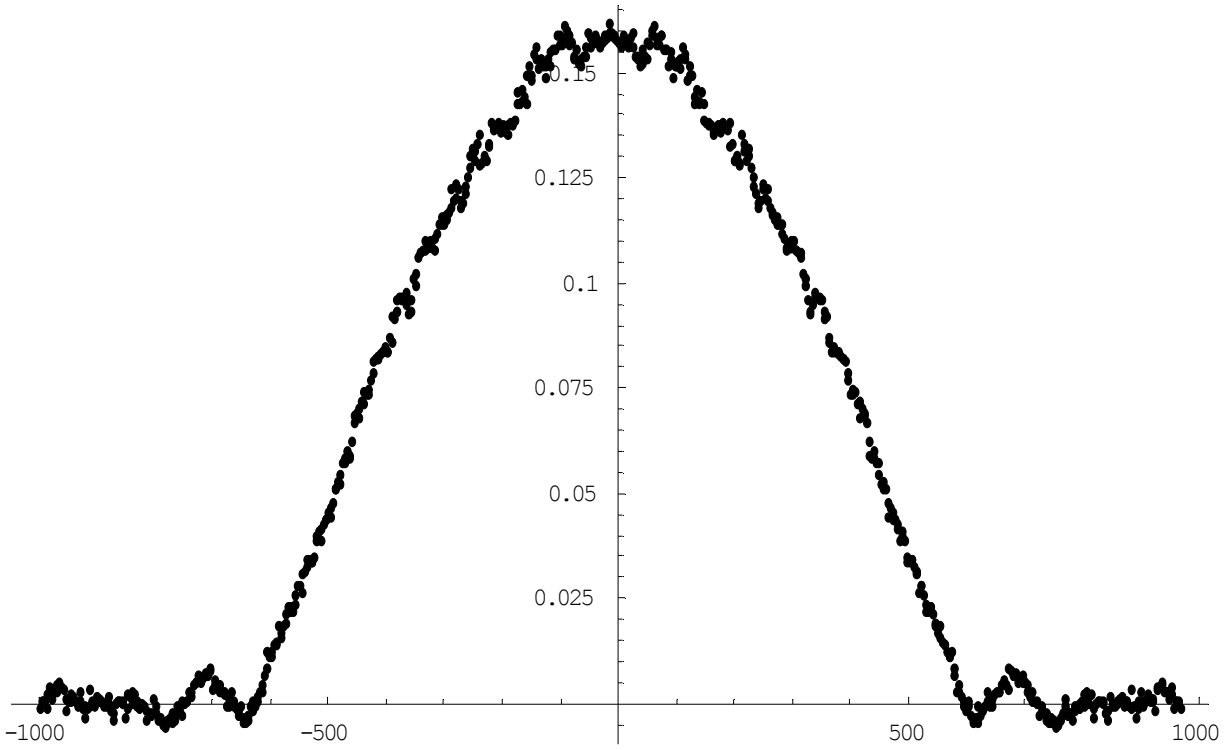

Graphics

Then the average of the flipped and unflipped distributions is taken and plotted into a single symmetric distribution.

funavesym20tau'=Interpolation[avesym20tau']
InterpolatingFunction[{{-996.45,969.15}},<>]
vmin=Min[avesym20tau']
vmax=Max[avesym20tau']
-996.45
969.15

A continuous function for the distribution is created and a new vmin and vmax for the Vaxis' is defined.

filter=Thread[{Vaxis',Table[(Sum[funavesym20tau'[If[(z+2.73*i) (Round[vmin]-1),vmin,If[(z+2.73*i) Round[vmax],vmax,(z+2.73*i)]]]-0,{i,-8,8,1}])/(2*8+1),{z,vmin,vmax,2.73}]}];
filtercont=Interpolation[filter]
InterpolatingFunction[{{-996.45,969.15}},<>]

Then the symmetric distribution is filtered with an 8 point spread filter function and the resulting filtered array is converted into a continuous function (filtercont).

```
vtail=Round[(300)/2.73]*2.73
sumofoffset=Sum[filtercont[z],{z,vmax-vtail,vmax,2.73}]
offB=-sumofoffset/(vtail/2.73)
Minimize[Sum[((filtercont[z]+A))^2,{z,vmin,vmin+vtail,2.73}]+Sum[((filtercont[z]+A))^2,{z,vmax-vtail,vmax,2.73}],{A}];
```

300.3
0.0797647
-0.000725134

Then the tail of the distribution is defined (where the atom density is 0). We take a tail length of 300 micrometers. Then the offset is determined by taking the average value of the tail and is defined as offB. The Minimize step that follows determines the offset by minimizing the sum of the square of the tail of the distribution but in the end wasn't used.

```
rmsdist=((Sum[(filtercont[z]+offB)^2,{z,vmin,vmin+vtail,2.73}]+Sum[(filtercont[z]+
offB)^2,{z,vmax-vtail,vmax,2.73}])/(2*110))^0.5
```
0.00227728

This step determines the rms value of the tail of the distribution with the offset added and is used later for purposes of error determination. The rms value is added and subtracted to the offset of the distribution and the relevant values are recalculated to determine an error.

```
funavesym20taufilter'=ListPlot[Thread[{Vaxis',Table[(Sum[funavesym20tau'[If[(z+
2.73*i)  (Round[vmin]-
1),vmin,If[(z+2.73*i)  Round[vmax],vmax,(z+2.73*i)]]]+offB+0*rmsdist,{i,-
8,8,1}])/(2*8+1),{z,vmin,vmax,2.73}]}]]
```

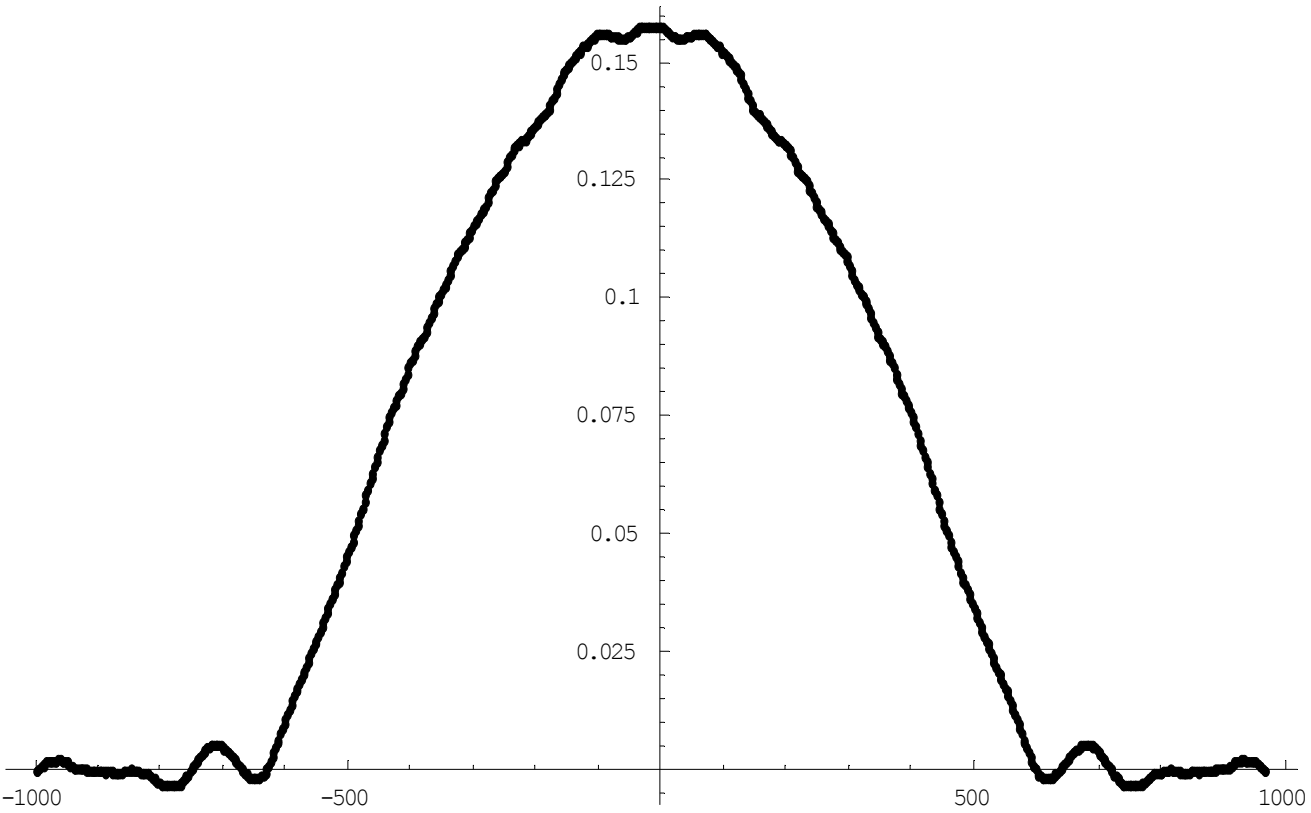

Graphics

This step creates a plot of the filtered symmetric distribution with the offset added.

```
fitting=Thread[{Vaxis',Table[(Sum[funavesym20tau'[If[(z+2.73*i)  (Round[vmin]-
1),vmin,If[(z+2.73*i)  Round[vmax],vmax,(z+2.73*i)]]]+offB+0*rmsdist,{i,-
8,8,1}])/(2*8+1),{z,vmin,vmax,2.73}]}];
```

$$\text{fitofsymdist} = \text{NonlinearFit}\left[\text{fitting}, \left(A * \text{Exp}\left[\frac{-2*(z-B)^2}{w^2}\right]\right), z, \{A, w, B\}, \text{MaxIterations} \to 1000, \text{AccuracyGoal} \to 10, \text{PrecisionGoal} \to 10, \text{ShowProgress} \to \text{True}\right]$$

Iteration: 60 ChiSquared: 0.0554121 Parameters: {0.166395,599.947,-13.65}
Iteration: 61 ChiSquared: 0.0554121 Parameters: {0.166395,599.948,-13.65}
Iteration: 62 ChiSquared: 0.0554121 Parameters: {0.166395,599.948,-13.65}
Iteration: 63 ChiSquared: 0.0554121 Parameters: {0.166395,599.948,-13.65}
Iteration: 64 ChiSquared: 0.0554121 Parameters: {0.166395,599.948,-13.65}
Iteration: 65 ChiSquared: 0.0554121 Parameters: {0.166395,599.948,-13.65}
Iteration: 66 ChiSquared: 0.0554121 Parameters: {0.166395,599.948,-13.65}

$$0.166395\, e^{-5.55652\times10^{-6}(13.65+z)^2}$$

This next step creates a 2D array for the filtered symmetric distribution with the offset added and then best fits a gaussian to this distribution and reports the Chi squared and the best fit gaussian.

fitofsymdistplt=Plot[fitofsymdist,{z,-1300,1000},PlotRange {-.05,0.25}]

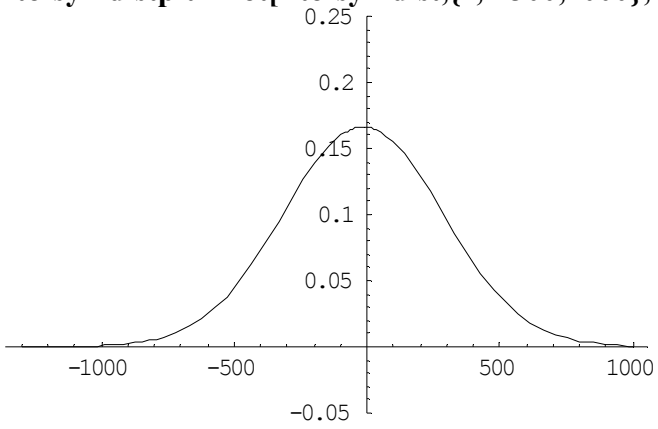

Graphics

Show[fitofsymdistplt,funavesym20taufilter']

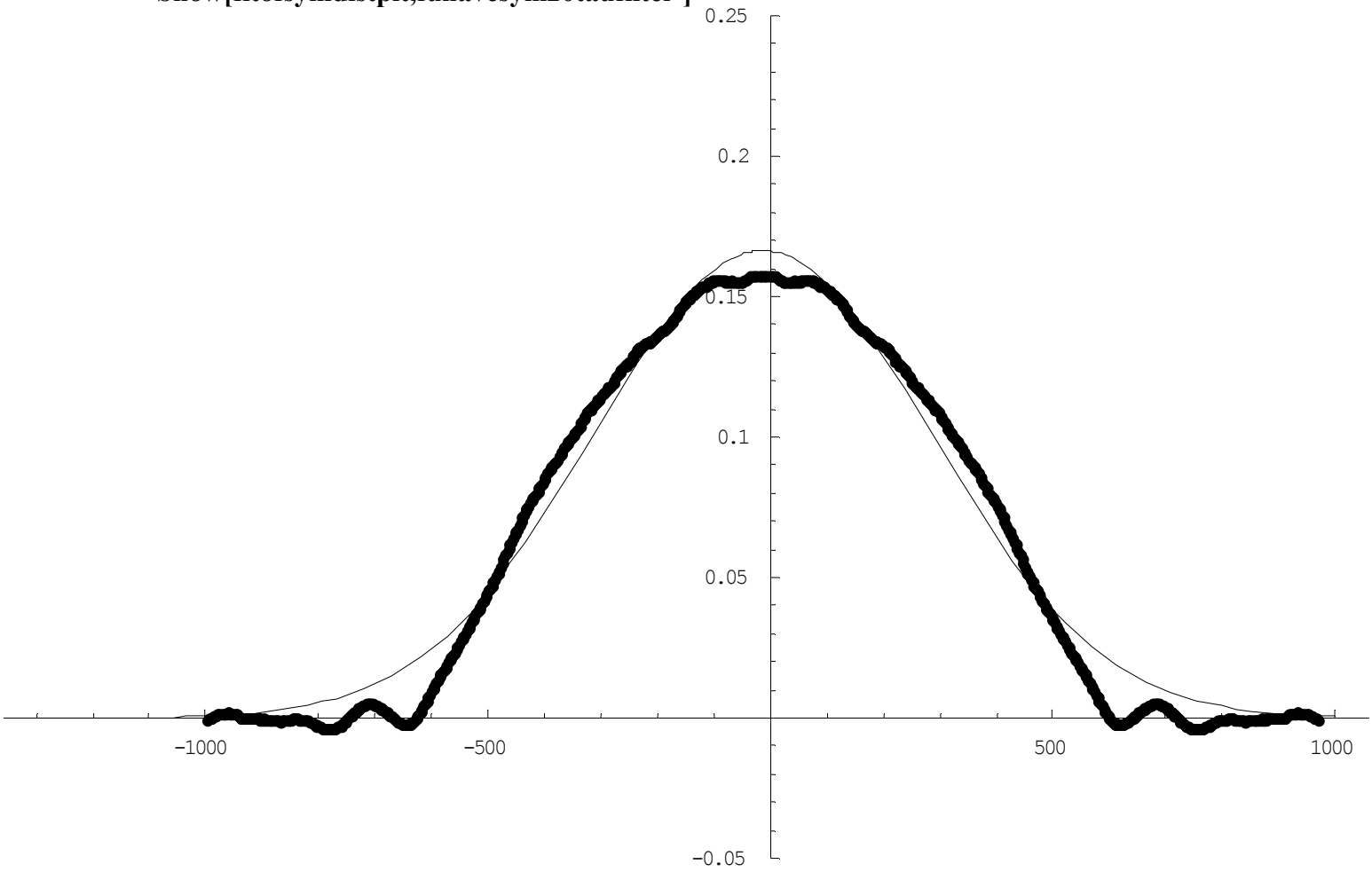

Graphics

The resulting best fit gaussian is then plotted together with the filtered symmetric distribution.

vc=-13.65
fun30taufiltercontsym=Interpolation[fitting]
-13.65
InterpolatingFunction[{{-996.45,969.15}},<>]

Then the center vc of the filtered symmetric distribution is defined and the distribution is made into a continuous function.

$$\text{Rms30taufiltercontsym} = \left(\frac{\text{NIntegrate}\left[(\text{fun30taufiltercontsym}[z]) * (z-vc)^2, \{z, vmin+vtail, vmax-vtail\}\right]}{\text{NIntegrate}\left[(\text{fun30taufiltercontsym}[z]), \{z, vmin+vtail, vmax-vtail\}\right]}\right)\text{^}0.5$$

263.278

```
wtry = 390;
```

$$\text{RmsofGausssym} = \left(\frac{\text{NIntegrate}\left[\left(1.0 * \text{Exp}\left[\frac{-2*(z-vc)^2}{wtry^2}\right]\right) * (z-vc)^2, \{z, vmin, vmax\}\right]}{\text{NIntegrate}\left[\left(1.0 * \text{Exp}\left[\frac{-2*(z-vc)^2}{wtry^2}\right]\right), \{z, vmin, vmax\}\right]}\right)\text{^}0.5;$$

```
wtryvalue = Table[wtry + i/4, {i, 600}];
```

$$\text{rmsvalue} = \text{Table}\left[\left(\frac{\text{NIntegrate}\left[\left(1.0 * \text{Exp}\left[\frac{-2*(z-vc)^2}{(wtry+i/4)^2}\right]\right) * (z-vc)^2, \{z, vmin, vmax\}\right]}{\text{NIntegrate}\left[\left(1.0 * \text{Exp}\left[\frac{-2*(z-vc)^2}{(wtry+i/4)^2}\right]\right), \{z, vmin, vmax\}\right]}\right)\text{^}0.5, \{i, 600\}\right];$$

```
rmsarray = Thread[{wtryvalue, rmsvalue}];
rmsarray' = Interpolation[rmsarray];
Minimize[Abs[rmsarray'[z] - Rms30taufiltercontsym], {z}]
wfinal = z /. Last[%]
```

{5.68434×10^-14, {z → 527.309}}
527.309
Sum30taufiltercontsym=NIntegrate[fun30taufiltercontsym[z],{z,vmin+vtail,vmax-vtail}]

120.696

```
amptry = 0.15
SumofGausssym = NIntegrate [amptry * Exp[-2 * (zz - vc)^2 / wfinal^2], {zz, vmin, vmax}];
amptryvalue = Table [amptry + 5 * i / 10000, {i, 1000}];
ampvalue = Table [NIntegrate [(amptry + 5 * i / 10000) * Exp[-2 * (zz - vc)^2 / wfinal^2], {zz, vmin, vmax}], {i, 1000}];
amparray = Thread [{amptryvalue, ampvalue}];
amparray' = Interpolation [amparray];
Minimize [Abs [amparray' [zz] - Sum30taufiltercontsym], {zz}]
ampfinal = zz /. Last [%]
```

0.15

$\{1.25439 \times 10^{-10}, \{zz \to 0.182664\}\}$

0.182664

Then the rms width and area of the filtered symmetric distribution are calculated and used to determine a gaussian function with the same rms width and area. This process here is completely automated.

```
Plot[{ampfinal * Exp[-2 * (z - vc)^2 / wfinal^2], fun30taufiltercontsym[z]}, {z, vmin, vmax}]
```

Graphics

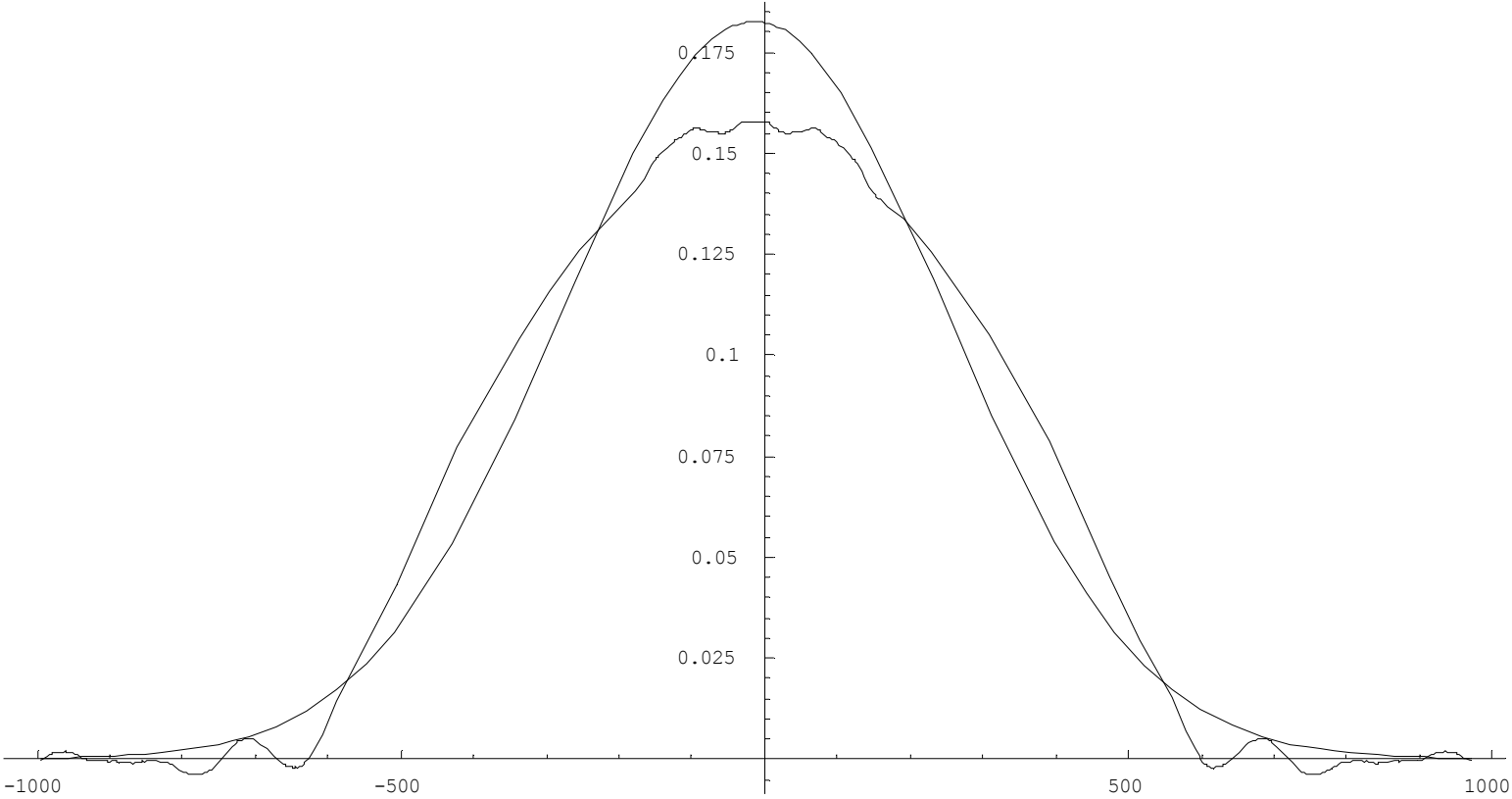

Then the filtered symmetric distribution and the same rms width and area gaussian are plotted.

```
results={wfinal,ampfinal}
v1=Round[(250)/2.73]*2.73;
v2=2*v1;
v3=3*v1;
ChisqtoGsym = Sum[(ampfinal *Exp[-2*(z-vc)^2/wfinal^2] - (fin30taufiltercontsym [z]))^2, {z, vmin, vmax, 2.73}]
ChisqtoGsym1 = Sum[(ampfinal *Exp[-2*(z-vc)^2/wfinal^2] - (fin30taufiltercontsym [z]))^2, {z, -v1+vc, v1+vc, 2.73}];
ChisqtoGsym2 = 2*Sum[(ampfinal *Exp[-2*(z-vc)^2/wfinal^2] - (fin30taufiltercontsym [z]))^2, {z, v1+vc+1, v2+vc, 2.73}];
ChisqtoGsym3 = 2*Sum[(ampfinal *Exp[-2*(z-vc)^2/wfinal^2] - (fin30taufiltercontsym [z]))^2, {z, v2+1+vc, v3+vc, 2.73}];
ChisqtoGsym4 = 2*Sum[(ampfinal *Exp[-2*(z-vc)^2/wfinal^2] - (fin30taufiltercontsym [z]))^2, {z, v3+1+vc, vmax, 2.73}];
weightedChisqtoGsym = Sum[Exp[-2*(z-vc)^2/wfinal^2]*(ampfinal *Exp[-2*(z-vc)^2/wfinal^2] - (fin30taufiltercontsym [z]))^2,
  {z, vmin, vmax, 2.73}]
ttt = Sum[Exp[-2*(z-vc)^2/wfinal^2], {z, vmin, vmax, 2.73}]
Norm8qChisqtoGsym=√(ChisqtoGsym/ampfinal^2/wfinal
StylePrint[ChisqtoGsym, wfinal, ampfinal, Norm8qChisqtoGsym, weightedChisqtoGsym /ttt]
```

```
{527.309,0.182664}
0.116042
0.066621
242.036
0.0812124
```

```
StylePrint[0.116042,527.309,0.182664,0.0812124,0.000275252]
```

Then the Chi squared between the same rms width and area gaussian and the filtered symmetric distribution is calculated and the final results for the rms width, amplitude, and Chi squared for various lengths of the tail are reported. Finally the normalized Chi squared is reported which accounts for various atom number and widths between distributions by dividing by the amplitude^2 * width.

Appendix D: Calculations relative to a 1D Bose gas in a harmonic trap

```
L = 7.738*10^-7; Lwidth = 2Pi.6*10^6; Isat = 16.4;
(*There is a 1.5 factor for linear polarization near the D2 line,
 but we'll add that to Isat for that case. This is the whole Isat for the Yag case.  There is also a different contribution from the D1 line for the lattice.*)
hbar = 1.055*10^-34; m = 87*1.67*10^-27; kb = 1.38*10^-23;
Detyag = 2Pi.9.9*10^13; Gee = 1.4603; FS = 2Pi.6.8*10^12;
(*Yag and lattice powers per beam; all lengths in meters*)
Isatlat = 3/2 Isat;
<<Graphics`Graphics`
```

All units are mks. The input above is for constants. L is the lattice light wavelength, Lwidth is the line width of the atomic transition. Isat is the relevant saturation intensity. Detyag is the YAG laser detuning which is fixed and FS is the fine structure splitting.

```
par = {a → 5.313*10^-9, Plat → 0.7, Detlat → 2Pi.3.2*10^12, Pyag → 9*11.5/121/243, woyag → 120*10^-6, wolat → 600.*10^-6, loadPyag → 9*11.5/121/243,
   loadwoyag → 120*10^-6, Nload → 3.05*10^5, N → 3.05*10^5, R_rms → 14.2*10^-6};
Print[par]
```

Most of these inputs are variable inputs and include, a, the 3D scattering length (a constant for these experiments). Plat is the lattice power, Detlat is the lattice detuning, Pyag is the YAG trap power, woyag is the YAG laser beam waist. wolat is the lattice laser beam waist. The load variable are those same variables during the lattice turn on. N is the number of total atoms.

```
(*Thomas-Fermi calculations relevant to
    \ BEC and loading*)
loadIyag = 2/Pi loadPyag/loadwoyag^2 ;(*only one Yag beam contributes horizontally*)
loadUyag = loadIyag/8 Isat Iwidth/Detyag hbar Iwidth;

loadKappayag = 4 loadUyag/loadwoyag^2 ; Print["loadUyag/kb =", loadUyag/kb /. par, "      loadKappayag =", loadKappayag /. par]
loadwr = Sqrt[(0*6.73514*10^(-22) + loadKappayag - 0*.821.295*10^-21)/m] ; (*1st term includes Yag and antifield for Bias 6.6G*)
loadwr0 = Sqrt[loadKappayag/m]
Print["chemical potential = ", mu /. par, "      loadwr/2Pi =", loadwr/2Pi /. par, "loadwr0/2Pi=", loadwr0/2Pi /. par] (*the initial horizontal oscillation frequency*)
mu = (15 hbar^2 m^(1/2) Nload Sqrt[2] * loadwr0 * loadwr^2 a)^(2/5) ; Print["The 3D temp , ie no lattice, is T3D = ", 2/3 2/7kb *mu /. par]
xcr = Sqrt[2 mu/(m loadwr^2)] ;
nc = 15/8Pi Nload Sqrt[2]/(xcr)^3 ; Print["Initial cloud size = ", xcr /. par, "      Initial peak density = ", nc /. par]
```

These calculations are relevant to the 3D BEC. First is the YAG intensity followed the YAG trap depth, spring constant and oscillation frequency. mu is the chemical potential, xcr is the 3D Thomas-Fermi radius and nc is the 3D density.

```
(*Calculations relevant to trapping in the 2D lattice.  Here we allow the number of atoms to have decreased from what they were in the 3D trap.*)

(*So in the central (L/2)^2 tube there are about N 2(L/2)^2/(Pi xcr^2) atoms, as is worked out in a calculation below*)

Ntube = N 2 (L/2)^2/(Pi xcr^2);

Ntubeavg = NIntegrate[{2/(Pi xcr^2) (1 - r^2/xcr^2) 2 Pi r Ntube} /. {N -> N (1 - r^2/xcr^2), Pyag -> Pyag * Exp[-2 r^2/woyag^2]}] /. par, {r, 0, xcr /. par}];

Print["The average Ntube, Ntubeavg, = ", Ntubeavg]

Iyag = 2 2/Pi Pyag/woyag^2; (*2 Yag beams, both contributing vertically*)

Ilat = 4 2/Pi Plat/wolat^2; (*each standing wave has retroreflection and interference, but they don't both contribute to the depth in both directions*)

Uyag = Iyag/(8 Isat) Lwidth/Detyag hbar Lwidth; Print["Ntube = ", Ntube /. par, "    Uyag/kb =", Uyag/kb /. par]

Ulat = Ilat/(8 * Isatlat) (Lwidth/Detlat + Lwidth/(2 (Detlat + FS))) hbar Lwidth;

Kappalat = 2 Ulat (2 Pi/L)^2; Print["Ulat/kb =", Ulat/kb /. par, "    Kappalat =", Kappalat /. par]

wr = Sqrt[Kappalat/m]; (*The transverse lattice oscillation frequency*);

Kappayag = 4 Uyag/woyag^2; Print["wr/2Pi =", wr/2Pi /. par, "    Kappayag =", Kappayag /. par]

Kappalatz = -2 * 4 Ulat/wolat^2 (hbar wr/(4 Ulat));

(* The factor of two is because both lattices antitrap vertically.  The last factor assumes that the atoms are in the ground state,
 where half their energy is potential. *)

wz = Sqrt[(Kappayag + Kappalatz)/m]; Print["Kappalatz =", Kappalatz /. par, "    wz/2Pi =", wz/2Pi /. par] (*the vertical  oscillation frequency*)

SEratelat = 2 Ilat/Isatlat (Lwidth^3/(8 Detlat^2) + Lwidth^3/(8 * 2 (Detlat + FS)^2)) (hbar wr/(4 Ulat));

(*The factor of two is because both lattice beams contribute zero point light to spontaneous emission.*)

SEtime = 1/(hbar wr/(4 Ulat)) Isatlat/(2 Ilat) 8 (Detlat^2 + 2 (Detlat + FS)^2)/Lwidth^2 * 27 * 10^-9; Print["SEratelat = ", SEratelat /. par, "    1/SEtime= ", 1/SEtime /. par]

(* Just a check of 2Pi factors*)

ar = Sqrt[hbar/(m wr)]; (*The radial ground state extension*)

a1D = -ar^2/a (1 - Cee a/(Sqrt[2] ar));

n1D = Ntube Sqrt[2]/(Sqrt[Pi] xcr); Print["ar =", ar /. par, "    a1D = ", a1D /. par, "    n1D = ", n1D /. par]

(*sigmaz is Sqrt[2] sigmar.  There may be a wrong numerical factor here.*)

noTonks = Sqrt[2/Pi^2 Ntube m wz/hbar];
```

```
RTonks = Sqrt[2 Ntube hbar/(wz m)]; Print["noTonks = ", noTonks /. par, "      RTonks = ", RTonks /. par]

RTonksavg = NIntegrate[((2/(Pi xcr^2))(1 - r^2/xcr^2)) 2 Pi r RTonks /. {N -> N[1 - r^2/xcr^2], Pyag -> Pyag*Exp[-2 r^2/woyag^2]} /. par, {r, 0, xcr /. par}];

Print["The average Tonks radius, RTonksavg, = ", RTonksavg]

noTF = ((9/64) Ntube^2 (m wz/hbar)^2 Abs[a1D])^(1/3);

RTF = (3 Ntube (hbar/(m wz))^2 / Abs[a1D])^(1/3); Print["noTF = ", noTF /. par, "      RTF = ", RTF /. par]

RTFavg = NIntegrate[((2/(Pi xcr^2))(1 - r^2/xcr^2)) 2 Pi r RTF /. {N -> N[1 - r^2/xcr^2], Pyag -> Pyag*Exp[-2 r^2/woyag^2]} /. par, {r, 0, xcr /. par}];

Print["The average Thomas Fermi radius, RTFavg, = ", RTFavg]

eta = noTF Abs[a1D]; (*This is the Dunjko et al. result, and seems all inclusive*)

etaavg = NIntegrate[((2/(Pi xcr^2))(1 - r^2/xcr^2)) 2 Pi r eta /. {N -> N[1 - r^2/xcr^2], Pyag -> Pyag*Exp[-2 r^2/woyag^2]} /. par, {r, 0, xcr /. par}];

Print["The average gas parameter eta is, etaavg=", etaavg /. par]

Print["The peak gas parameter eta peak is, etapeak=", eta /. par]

g1D = -2 hbar^2/(m a1D);

gamma = m g1D/(hbar^2 n1D);

gammaavg = NIntegrate[((2/(Pi xcr^2))(1 - r^2/xcr^2)) 2 Pi r gamma /. {N -> N[1 - r^2/xcr^2], Pyag -> Pyag*Exp[-2 r^2/woyag^2]} /. par, {r, 0, xcr /. par}];

Print["The average gas parameter gamma is, gammaavg=", gammaavg /. par]

Const = 4*R_rms/(Ntube*Abs[a1D]); Print["The const is, const=", Const /. par]

gammatube = (2*Const - 1 + Sqrt[(1 - 2*Const)^2 + 4*Const*Sqrt[5]])/2; Print["The peak gamma tube avg is, gammatube=", gammatube /. par]

(*gammatube is the gamma averaged over the density dist. for a single tube*)

gammatubeavg = NIntegrate[((2/(Pi xcr^2))(1 - r^2/xcr^2)) 2 Pi r gammatube /. {N -> N[1 - r^2/xcr^2], R_rms -> R_rms[(1 - r^2/xcr^2)]^((1/3)*(eta/(eta+2)) + (1/2)*(2/(eta+2))), Pyag -> Pyag*Exp[-2 r^2/woyag^2]} /. par,
  {r, 0, xcr /. par}]; Print["The average gas parameter gammatube is, gammatubeavg=", gammatubeavg /. par]

TvTF = 2 (1/(5 kb)) m RTF^2 wz^2; Print["The release temperature, mean field, = ", TvTF /. par]

TvTonks = 2 (1/(8 kb)) m RTonks^2 wz^2; Print["The release temperature, Tonks, = ", TvTonks /. par]

TvTFavg = Integrate[((2/(Pi xcr^2))(1 - r^2/xcr^2)) 2 Pi r TvTF /. {N -> N[1 - r^2/xcr^2]} /. par, {r, 0, xcr /. par}];

Print["The average release temperature,                    TvTFavg, = ", TvTFavg]

TvTonksavg = Integrate[((2/(Pi xcr^2))(1 - r^2/xcr^2)) 2 Pi r TvTonks /. {N -> N[1 - r^2/xcr^2]} /. par, {r, 0, xcr /. par}];
```

The above expressions are relevant to the 1D gas. w's stand for trapping frequencies, SE is spontaneous emission, R is the atoms cloud radius, and T is temperature.

References:

[1] M.H. Anderson, J.R. Ensher, M.R. Matthews, C.E. Wieman, E.A. Cornell. Observation of Bose-Einstein Condensation in a Dilute Atomic Vapor. *Science* **269**, 198-201 (1995).

[2] C.C. Bradley, C.A. Sackett, J.J. Tollett, and R.G. Hulet. Evidence of Bose-Einstein Condensation in an Atomic Gas with Attractive Interactions. *Phys. Rev. Lett* **75**, 1687-1690 (1995).

[3] K. Davis, M-O. Mewes, M. Andrews, M. van Druten, D. Durfee, D. Kurn, and W. Ketterle. Bose-Einstein Condensation in a Gas of Sodium Atoms. *Phys. Rev. Lett.* **75**, 3969 (1995).

[4] L. Tonks, *Phys Rev.* **50**, 955 (1936).

[5] M. Girardeau, *J. Math. Phys.* **1**, 516 (1960).

[6] E.H. Lieb and W. Liniger, *Phys Rev.* **130**, 1605 (1963).

[7] H.J. Metcalf, P. Van der Straten. Laser Cooling and Trapping. Springer. New York, 1999.

[8] M. Barrett, J. Sauer, and M.S. Chapman, *Phys Rev. Lett.* **87**, 010404 (2001).

[9] T. Weber, J. Herbig, M. Mark, H.-C. Nagerl, and R. Grimm, *Science* **299**, 232 (2003).

[10] Y. Takasu, K. Maki, K. Komori, T. Takano, K. Honda, M. Kumakura, T. Yabuzaki, and Y. Takahashi, *Phys Rev Lett.* **91**, 040404 (2003).

[11] G. Cennini, G. Ritt, C. Geckeler, and M. Weitz, *Appl. Phys.B: Lasers Opt.* **77**, 773 (2003).

[12] D. Rychtarik, B. Engeser, H.-C. Nagerl, and R. Grimm, *Phys. Rev. Lett.* **92**, 173003 (2004).

[13] D. A. Steck. Rubidium 87 D Line Data. Los Alamos, 2003.

[14] J.L. Hall, L. Hollberg, T. Baer, and H.G. Robinson, *Appl. Phys. Lett.* **39**(9), (1981).

[15] S.L. Winoto, M.T. Depue, N.E. Bramall, and D.S. Weiss, *Phys Rev. A* **59**, R19 (1999).

[16] J. Dalibard and C. Cohen-Tannoudji. Laser Cooling Below the Doppler Limit by Polarization Gradients – Simple Theoretical Models. *J. Opt. Soc. Am. B* **6**, 2023-2045 (1989).

[17] Y. Takasu, K. Honda, K. Komori, T. Kuwamoto, M. Kumakura, Y. Takahashi, and T. Yabuzaki, *Phys. Rev. Lett.* **90**, 023003 (2003).

[18] M. DePue, PhD. Thesis, U.C. Berkeley (1999).

[19] D.J. Han unpublished calculation, U.C. Berkeley (2000).

[20] C. N. Yang, Y. P. Yang, *J. Math. Phys.* **10**, 1115 (1969).

[21] M. Greiner, O. Mandel, T. Esslinger, T. W. Hansch, I. Bloch, *Nature* **415**, 39 (2002).

[22] B. L. Tolra *et al*., *Phys. Rev. Lett.* **92**, 190401 (2004).

[23] M. Olshanii, *Phys. Rev. Lett.* **81**, 938 (1998).

[24] V. Dunjko, V. Lorent, M. Olshanii, *Phys. Rev. Lett.* **86**, 5413 (2001).

[25] W. Ketterle, D. S. Durfee, and D. M. Stamper-Kurn: *Making, probing and understanding Bose-Einstein condensates*. In *Bose-Einstein condensation in atomic gases*, Proceedings of the International School of Physics "Enrico Fermi", Course CXL, edited by M. Inguscio, S. Stringari and C. E. Wieman (IOS Press, Amsterdam, 1999) pp. 67-176; e-print cond-mat/9904034.

[26] A. F. Ho, M. A. Cazalilla, T. Giamarchi, *Phys. Rev. Lett.* **92**, 130405 (2004).

[27] M. Olshanii, V. Dunjko, *Phys. Rev. Lett.* **91**, 090401 (2003).

[27] M. Yasuda and F. Shimizu, *Phys. Rev. Lett.* **77**, 3090 (1996).

[28] W. Ketterle and H.-J. Miesner, *Phys Rev. A* **56**, 3291 (1997).

[29] C. McKenzie *et al.*, *Phys. Rev. Lett.* **88**, 120403 (2002).

[30] G. B. Partridge *et al.*, *cond-matI/*0505353.

[31] M. Greiner *et al.*, *Phys. Rev. Lett.* **94**, 110401 (2005).

[32] S. Folling *et al.*, *Nature* (London) **434** 481 (2005).

[33] D. Gangardt and G. Shlyapnikov, *Phys. Rev. Lett.* **90**, 010401 (2003).

[34] M. Theis *et al.*, *Phys. Rev. Lett.* **93**, 123001 (2004).

[35] J. L. Bohn and P. S. Julienne, *Phys. Rev. A* **56**, 1486 (1997).

[36] A. Fioretti *et al., Eur. Phys. J. D* **15**, 189 (2001).

[37] M. T. DePue *et al., Opt. Commun.* **180**, 73 (2000).

[38] M. D. Girardeau and E. M. Wright, *Phys. Rev. Lett.* **87**, 050403 (2001).

[39] B. Paredes *et al., Nature* **429**, 277-281 (2004).

[40] T. Kinoshita, T. Wenger, and D. S. Weiss, *Science* **305**, 1125-1128 (2004).

[41] M. Rigol and A. Muramatsu, *Phys. Rev. Lett.* **94**, 240403 (2005).

[42] P. Pedri, L. Santos, P. Ohberg, and S. Stringari, *Phys. Rev. A* **68**, 043601 (2003).

[43] S. Coleman, *Phys. Rev. D* **11**, 2088-2097 (1975).

[44] M. Tabor, *Chaos and Integrability in Nonlinear Dynamics* (Wiley, New York, 1989).

[45] F. Herrmann and P. Schmalzle, *Am. J. Phys.* **49**, 761-764 (1981).

[46] T. Kinoshita, T. Wenger, D. S. Weiss, *Phys. Rev. Lett.* **95**, 190406 (2005).

[47] S. Wu, Y. J. Wang, Q. Diot, and M. Prentiss, *Phys. Rev. A* **71**, 043602 (2005).

[48] Y. J. Wang *et al. Phys. Rev. Lett.* **94**, 090405 (2005).

[49] M. G. Moore, T. Bergeman, and M. Olshanii, *J. Phys. IV* **116**, 69-86 (2004).

[50] H. Wu and C. J. Foot, *J. Phys. B* **29**, L321-L328 (1996).

[51] C. Raman *et al.*, *Phys. Rev. Lett.* **83**, 2502-2505 (1999).

[52] Th. Anker *et al.*, *Phys. Rev. Lett.* **94,** 020403 (2005).

[53] G. Kalosakas *et al., Phys. Rev. Lett.* **89** 030402 (2002).

[54] A.F. Ho, M.A. Cazalilla, and T. Giamarchi, *Phys. Rev. Lett.* **92** 130405 (2004).

Vita Trevor Wenger

Undergraduate School: Millersville University B.S. Physics Sept. 1994 – Dec. 1999

Graduate School: Penn State University Ph.D. Physics Sept. 2000 – May 2007

Publications:

T. Kinoshita, T. Wenger, and D. S. Weiss, *Phys Rev. A* **71**, 011602 (2005).

T. Kinoshita, T. Wenger, and D. S. Weiss, *Science* **305**, 1125-1128 (2004).

T. Kinoshita, T. Wenger, and D. S. Weiss, *Phys. Rev. Lett.* **95**, 190406 (2005).

T. Kinoshita, T. Wenger, and D. S. Weiss, *Nature* **440**, 900-903 (2006).